UNIVERSITY OF THE WITWATERSRAND, JOHANNESBURG

Synthesis and characterization of lead-free cesium halide perovskite nanocrystals and their application in Schottky diodes

A dissertation submitted to the Faculty of Science, University of the Witwatersrand, in partial fulfillment for the degree of Master of Science in Chemistry

By

Olusola Moses Akinbami

1866971

Supervisors:

Dr. P.K. Mubiayi

Prof. N. Moloto

2021

Declaration

I declare that the work reported in this dissertation is my own independent work, submitted at the School of Chemistry, University of the Witwatersrand, Johannesburg. This work has not been submitted for any degree or examination in any other institution of higher learning.

15/06/2021

Candidate | Date

15/06/2021

Supervisor | Date

15/06/2021

Co-Supervisor | Date

Abstract

The need for renewable energy sources cannot be overemphasized. Global warming, climate change, environmental pollution and fluctuations in crude oil prices are some of the disadvantages of utilizing non-renewable energy sources. Hence, in recent times, research has been geared towards transitioning from non-renewable energy sources to renewable energy sources. Solar energy due to its abundance, reliability and environmental friendliness is one of the renewable energy sources being explored globally. Photovoltaic cells are among the most promising technologies for clean energy production. Among the different solar cell technologies, the perovskite solar cells (PSCs) have the greatest potential due to their outstanding power conversion efficiency and their ease of fabrication. However, incorporation of lead (Pb) in the perovskite's crystal structure has led to some disadvantages such as toxicity and stability issues in perovskites. As a result, research is ongoing on various ways of overcoming perovskite's toxicity while improving their stability in ambient conditions. In this study, to eliminate Pb toxicity, tin (Sn), bismuth (Bi) and zinc (Zn) were used as Pb replacements in a perovskite semiconductor material with an attempt to lower toxicity and improve stability. The Pb-based perovskites are the most efficient perovskites however, Pb is toxic to humans and Pb-based perovskites are unstable, hence alternative perovskites possessing high stability and low toxicity are required for the commercialization of perovskite solar cells. Sn and Pb belong to the same group in the periodic table while also having similar ionic radii. Bi shares the same period with Pb while Zn is non-toxic and an essential mineral element. Therefore, the three cations are investigated as promising perovskite candidates.

The colloidal method of synthesis was employed because of its flexibility and allowance of reaction parameter variation. Therefore, the reaction temperature and time were varied to investigate the optimum conditions for the synthesis of $CsSnBr_3$, $Cs_3Bi_2Br_9$ and Cs_2ZnBr_4 perovskite nanocrystals (NCs). Both temperature and time had an effect on the resultant particles. Cubic $CsSnBr_3$ nanocrystals were successfully synthesized at the optimum conditions of 230 °C for 1 min in oleylamine (OLA) and oleic acid (OA) using $SnBr_2$ and Cs_2CO_3 precursors. The $CsSnBr_3$ NCs produced quantum dots morphology. Hexagonal $Cs_3Bi_2Br_9$ NCs were synthesized at optimum conditions of 210 °C while orthorhombic Cs_2ZnBr_4 hybrid perovskite was formed at 160 °C, both using 1 min synthetic time. Pseudo spherical and nanorod morphologies were obtained for the $Cs_3Bi_2Br_9$ and Cs_2ZnBr_4 NCs, respectively. The bandgaps were found to be 1.72 eV, 2.82 eV and 3.18 eV for $CsSnBr_3$, $Cs_3Bi_2Br_9$ and Cs_2ZnBr_4,

respectively. The XRD and XPS showed the composition of the individual perovskite while NMR and FTIR conclusively showed that OLA successfully capped the NCs surface. The $CsSnBr_3$ NCs were stable for three days while the Cs_2ZnBr_4 and $Cs_3Bi_2Br_9$ were stable for over 21 days.

The electrical properties of the Sn, Bi and Zn based perovskites were investigated by fabricating Schottky diodes. The thin-films were fabricated *via* spin-coating method and the gold (Au) contacts were thermally deposited on the thin-films. The three perovskite materials showed rectifying properties while the parameters of the diode were acquired using three different methods namely: Classical thermionic model, Cheung's, and the Norde's method. The Cs_2ZnBr_4 material showed the best electrical properties due to its lowest series resistance and impressive barrier height while both the $CsSnBr_3$ and $Cs_3Bi_2Br_9$ perovskite NCs had electrical parameters that are comparable to the ones reported in the literature. As such, $CsSnBr_3$, $Cs_3Bi_2Br_9$ and Cs_2ZnBr_4 are potential perovskites for solar cell applications and can be used as hole-transporting layer (wide bandgap $Cs_3Bi_2Br_9$ and Cs_2ZnBr_4) or the active layer ($CsSnBr_3$).

Acknowledgements

I ascribe all glory to God almighty that saw me through this program. I sincerely appreciate my supervisors Professor N. Moloto and Dr. P. K. Mubiayi for their mentorship during this program. My special appreciation also goes to Dr. M. Bodunrin, Dr. A. Ipadeola, Dr. F. Otieno, Dr. M. Airo, Dr. R. Erasmus, Dr. S. Gqoba, all my colleagues in Lab 330B and CATMAT group. To my friends Thelma Majola, Yongezile Mhlana, Refilwe Moepya, Zakhele Ndala, Grace Ngubeni and Ndivhuwo Shumbula, I say thank you for the emotional support. My unfeigned love and appreciation go to everyone at WITS MMU for providing microscopic and structural instrumentation and their expertise. My gratitude goes to the School of Chemistry at Wits University and the National Research Foundation (RSA) for funding.

I sincerely appreciate my parents Dr. and Mrs. Akinbami, my siblings Damilola and Adeola Akinbami for financial, emotional and spiritual support.

Dedication

This dissertation is dedicated to my parents and to the giants whose shoulders I sat on.

List of presentations

- Oral presentation at Catalysis and Materials' (CATMAT) seminar held at the School of Chemistry, University of the Witwatersrand on the 21/05/2019.
- Oral presentation held on the 9th Annual Gauteng Nanoscience's Young Researchers' Symposium (2019 SANi-NYRS) held at the University of Pretoria on 12/11/2019. (2nd prize MSc category)
- Grad-flash presentation at the 10th annual University of the Witwatersrand's annual cross-faculty postgraduate symposium held at Wits University on 13/10/2020. (Runner-up winner)
- Oral presentation at the South African Chemical Institute Young Chemists' Symposium. Royal Society of Chemistry local section. Organized by University of Johannesburg on 18/11/2020. (2nd Prize MSc category).

List of publications

- O. Akinbami, G. N. Ngubeni, F. Otieno, R. Kadzutu-Sithole, E. C. Linganiso, Z. N. Tetana, S. S. Gqoba, K. P. Mubiayi and N. Moloto. "The effect of temperature and time on the properties of 2D Cs_2ZnBr_4 perovskite nanocrystals and its application in a Schottky barrier device." Journal of Materials Chemistry C. 2021.
- Olusola M. Akinbami, Samuel R. Oke, Michael O. Bodunrin. "The state of Renewable Energy Development in South Africa: An Overview." Alexandria Engineering Journal. 2021.
- Lead-free Ruddorfite-type $Cs_3Bi_2Br_9$ nanoparticles for photocatalytic degradation of rhodamine B and methylene blue. Under review at Journal of Photochemistry and Photobiology A: Chemistry (JPHOTOCHEM-D-21-00168).
- The synthesis and characterization of $CsSnBr_3$ and $Cs_3Bi_2Br_9$ perovskite nanocrystals and their application in a Schottky diode. To be submitted.

Table of Contents

List of figures

List of tables

List of abbreviations

BG: Band gap

Bi: Bismuth

Br: Bromine

Cs: Cesium

CB: Conduction band

FTIR: Fourier Transform Infrared

IEA: International Energy Agency

MA: Methylammonium

NCs: Nanocrystals

Nm: Nanometers

NMR: Nuclear Magnetic Resonance

OA: Oleic Acid

OLA: Oleylamine

Pb: Lead

PCE: Power conversion efficiency

Pm: Picometers

PL: Photoluminescence

PSCs: Perovskite solar cells

PXRD: Powder X-ray diffraction

Sn: Tin

TEM: Transmission Electron Microscope

VB: Valence band

Zn: Zinc

Synopsis

The aim of the study was to synthesize and study the effect of different lead-free perovskite nanocrystals using the colloidal method while evaluating their electrical properties and potential application for solar cell applications by fabricating Schottky diodes. The layout of the dissertation is therefore shown below.

Chapter 1: Is comprised of the general background, problem statement, motivation for the study as well as the aims and objectives.

Chapter 2: Is the literature review of perovskites, their properties as well as the synthetic routes. Also, a review on metal-semiconductor contacts was discussed.

Chapter 3: Reports on the effect of temperature and time variation on the synthesis of $CsSnBr_3$ nanocrystals.

Chapter 4: Reports on the effect of temperature and time variation on the synthesis of $Cs_3Bi_2Br_9$ nanocrystals.

Chapter 5: Reports on the effect of temperature and time variation on the synthesis of Cs_2ZnBr_4 nanocrystals.

Chapter 6: Reports on the investigation of the electrical properties of $CsSnBr_3$, $Cs_3Bi_2Br_9$ and Cs_2ZnBr_4 nanocrystals.

Chapter 7: Meticulously discuss the conclusions and suggests possible future studies.

CHAPTER 1
General background

1.1 Introduction

The role of energy in human development cannot be overemphasized. Since the discovery and subsequent use of electricity, humans have benefitted greatly from the productivity, ease of life and economic growth it affords [1, 2]. The ever increasing demand for electricity is largely satisfied by non-renewable energy sources such as natural gas and coal. However, their unreliability and associated deleterious environmental effects on the planet are sadly, a cause for concern [3–5]. South Africa is the world's 7th largest producer of coal according to the latest publication by the International Energy Agency (IEA) Energy Atlas [6, 7]. Coal is the largest energy fuel source in South Africa [8] accounting for over 85% of all generated electricity in the country as shown in Fig. 1.1. Unfortunately, such overreliance on coal has positioned South Africa among the top ten greenhouse gas emitters in the world [9–11], while being the largest carbon dioxide (CO_2) emitter in Africa. Due to global warming and climate change, nonrenewable energy sources are gradually being replaced with clean and readily available energy sources produced by nature termed renewable energy [12, 13]. The rise in CO_2 emission coupled with the incessant load shedding by South Africa's electricity provider has made the need for an alternative source of electricity generation a major necessity. The drive towards renewable energy has been further articulated by the Sustainable Development Goals (SDGs). The SDGs are an assemblage of 17 global goals ratified by the United Nations (UN) to serve as a blueprint towards ensuring sustainability for the future of mankind. The 7th goal in the UN SDGs iterates the need for clean energy. There are various sources of RE which include solar, wind, geothermal and biomass.

Solar energy is an enormous renewable energy source capable of serving as an alternative to fossil fuels. This form of energy is unique because most other RE sources depends directly or indirectly on it. For instance, biomass energy derived from organic matter depends directly on solar energy because plants' growth is dependent on photosynthesis [14, 15]. Wind energy depends indirectly on solar energy since wind is partially caused by the differential heating on the earth's surface due to solar radiation [16].

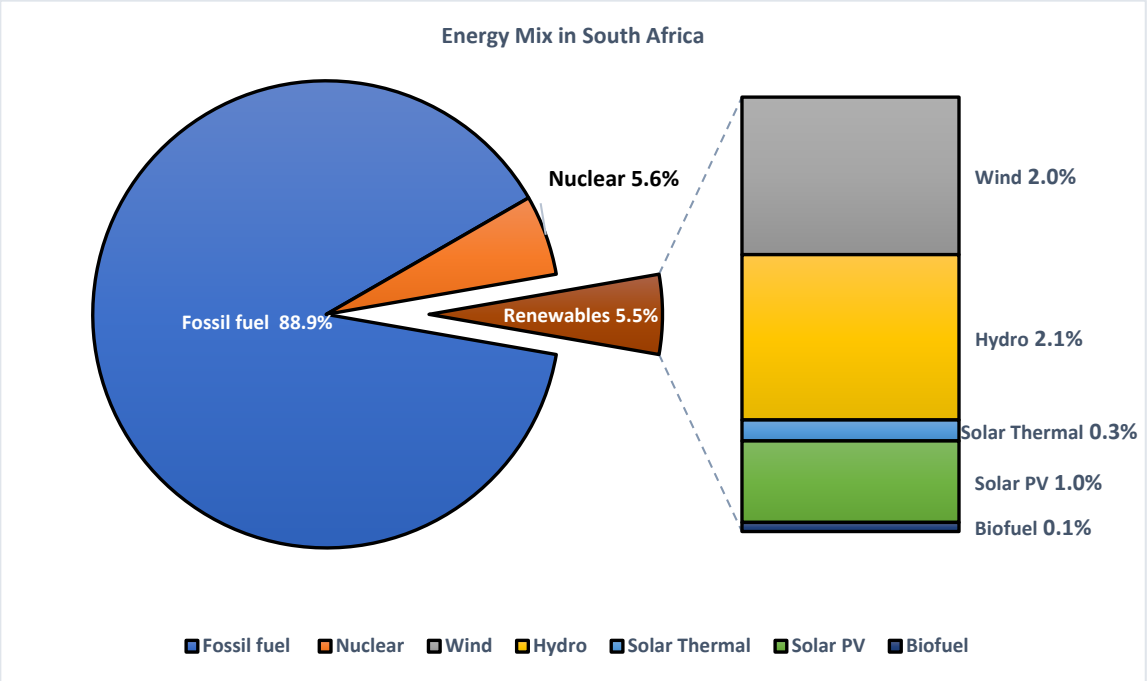

Fig. 1.1: International Energy Agency (IEA) graph showing the source of electricity generation in South Africa [17].

Theoretically, solar energy can satisfy the global energy needs provided it can be efficiently harnessed since about 4 million exajoules of energy get radiated on earth annually [18]. Solar cells are devices used to directly harness solar energy into electricity and it works through the principle of photoelectric effect [19]. There are three generations of solar cells starting with the crystalline silicon as the 1st generation solar cell, followed by the thin-film solar cells as the 2nd generation and lastly, the perovskite semiconductors as the 3rd generation solar cells. The perovskite solar cell (PSC) is a particularly disruptive solar cell because of its attained efficiency over a short period. Interestingly, the PSCs are less than a decade from their inception but have outperformed most other types of solar cells in terms of efficiency and have comparable performance with silicon solar cells as shown in Fig. 1.2 [20].

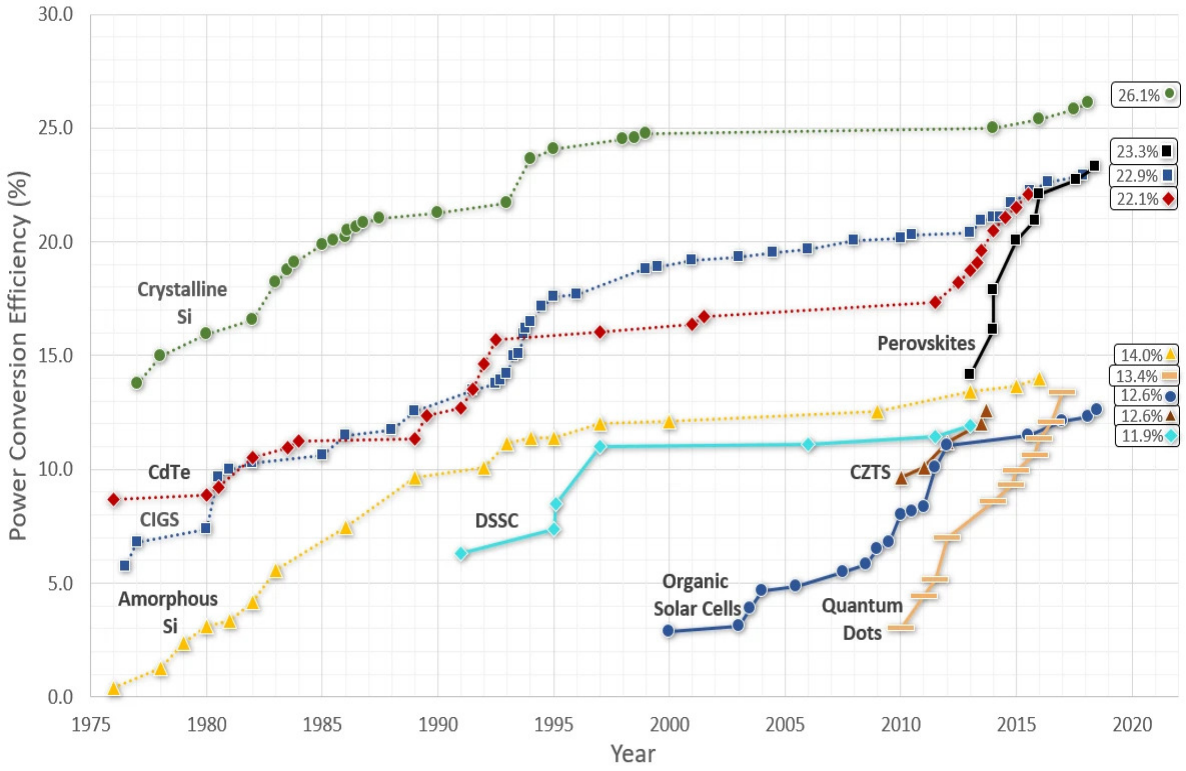

Fig. 1.2: The chart of solar cell efficiencies [20].

Although impressive performances have been recorded for perovskites in solar cell application, the most effective perovskites however are lead (Pb) based perovskite and they are unstable. Hence, new materials are being explored as a substitute to Pb for solar cell application.

1.2 Problem Statement

Electricity demand is constantly rising and the conventional means of electricity generation cannot sufficiently cater to the world's energy demands largely because of the dwindling coal and fossil fuel reserves. Emissions of CO_2 is another drawback of the utilization of non-renewable energy sources therefore, renewable energy (solar energy) is the most feasible alternative to produce clean and sustainable energy for mankind. Perovskite materials have shown to be efficient light absorbers however; toxicity and stability are the main issues inhibiting the commercialization of these materials. The Pb based perovskites have been extensively studied, contrarily, research into Pb-free perovskites is still in its infancy. Hence, it is a necessity to explore lead-free perovskite materials for solar cell applications and other electronic and optoelectronic devices.

1.3 Motivation

Perovskite materials possess outstanding optoelectronic properties, high electron and hole mobility, direct bandgap and a simple method of fabrication. Their bandgap can be tuned through the manipulation of their shape and size or by doping. Also, these materials are defect tolerant and they possess low non-radiative carrier recombination rates therefore, they are ideal materials for optoelectronic and electronic applications.

1.4 Aim and Objectives

The aim of this project was to study the effect of divalent and trivalent cations on the properties of cesium based all-inorganic perovskites. Their electrical properties at the metal-semiconductor interface were investigated by fabricating a Schottky diode. To fulfill the aforementioned aim, the following objectives were identified:

- Colloidal synthesis of $CsSnBr_3$, $Cs_3Bi_2Br_9$ and Cs_2ZnBr_4 nanocrystals.
- Determination of the optimum reaction conditions for the synthesis of $CsSnBr_3$, $Cs_3Bi_2Br_9$ and Cs_2ZnBr_4 by varying reaction parameters such as temperature and time.
- Characterization of the synthesized materials *via* several techniques such as XRD, TEM, UV-vis absorption, photoluminescence, Raman, FTIR and XPS spectroscopies, CV and TGA among others.
- Investigation of the electrical properties of the nanocrystals and their performance as a Schottky diode.

1.5 References

[1] S. Pachauri, A. Brew-Hammond, D. Barnes, D. Bouille, S. Gitonga, V. Modi, G. Prasad, A. Rath, H. Zerrifi, *Energy Access for Development* (2012) 1401-1458.

[2] A. Jain, T. Shahidi, *Economics of Energy & Environmental Policy 8* (2019).

[3] M. Hasanuzzaman, U.S. Zubir, N.I. Ilham, H. Seng Che, *Wiley Interdisciplinary Reviews: Energy and Environment 6* (2017) e222.

[4] N. Kannan, D. Vakeesan, *Renewable and Sustainable Energy Reviews 62* (2016) 1092–1105.

[5] J. Schwartz, A. Vodonos, E. Marais, M. Sulprizio, L. Mickley, *Environmental Epidemiology 3* (2019) 356.

[6] International Energy Agency 2020, https://www.iea.org/ accessed February 17, 2021.

[7] S. Jain, P. Jain, *Energy Procedia* 143 (2017) 721–726.

[8] International Energy Agency database 2019 https://www.iea.org/ accessed February 17, 2021.

[9] F.V. Bekun, F. Emir, S.A. Sarkodie, *Science of The Total Environment* 655 (2019) 759–765.

[10] J.G. Olivier, K. Schure, J. Peters, *PBL Netherlands Environmental Assessment Agency* 5 (2017).

[11] G. Cohen, J.T. Jalles, P. Loungani, R. Marto, *Energy Policy* 118 (2018) 58–68.

[12] J.A. Turner, *Science* 285 (1999) 687–689.

[13] N. Panwar, S. Kaushik, S. Kothari, *Renewable and Sustainable Energy Reviews* 15 (2011) 1513–1524.

[14] C.J. Weinberg, R.H. Williams, *Scientific American 263* (1990) 146–155.

[15] B.A. Stout, F. and A.O. of the U. Nations, Biomass Energy Profiles, *Food & Agriculture Org.*, 1983.

[16] G.M. Joselin Herbert, S. Iniyan, E. Sreevalsan, S. Rajapandian, *Renewable and Sustainable Energy Reviews* 11 (2007) 1117–1145.

[17] International Energy Agency 2021 https://www.iea.org/ accessed February 17, 2021.

[18] E. Kabir, P. Kumar, S. Kumar, A.A. Adelodun, K.-H. Kim, *Renewable and Sustainable Energy Reviews* 82 (2018) 894–900.

[19] L. Hernández-Callejo, S. Gallardo-Saavedra, V. Alonso-Gómez, *Solar Energy* 188 (2019) 426–440.

[20] National Renewable Energy Laboratory Solar Cell Efficiency Table 2020 https://www.nrel.gov/pv/cell-efficiency.html accessed January 17, 2021.

CHAPTER 2

LITERATURE REVIEW

2.1 Perovskite overview

Perovskite referred to a mineral composed of calcium titanate ($CaTiO_3$) which was first discovered in Russia in 1839 by a German mineralogist named Gustav Rose, the discovered mineral was however named after a Russian mineralogist called Count Lev Perovski hence the term perovskite [1–3]. Perovskites are characterized as the class of materials with stoichiometry similar to $CaTiO_3$ with general formula ABO_3 where A is usually a large cation, B is a smaller cation and O is an oxide. The examples of such perovskites are $BaTiO_3$ and $CaTiO_3$ compounds. The formula was later generalized to ABX_3 in order to include other materials such as halide perovskites ($CsPbBr_3$) [4–6]. The crystallographic arrangement of perovskites shows that the A cation is coordinated to 12 anions to form the cuboctahedra structure while the B cation is coordinated to 6 oxygen/halogen atoms to form the octahedral structure as shown in Fig. 2.1 [7, 8]. An ideal perovskite is cubic in nature, however, due to variations in the ionic radii of constituent elements in the perovskite, deviation from the ideal cubic structure might occur [9–11]. The versatility in the application of perovskites is largely due to the BX_6 octahedral, although the A cation also influences the structure-property relationship of perovskites [12, 13]. There are three major distortions that influence the structure and property of any given perovskite [14]. They are cation displacement, octahedral distortion and octahedral tilting. The magnetic, electric and dielectric properties of perovskites largely depend on these distortions.

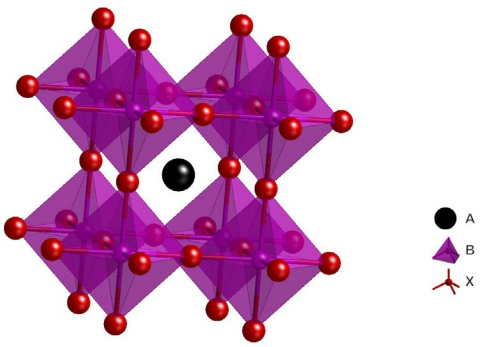

Fig. 2.1: Crystal structure of ABX_3 perovskite.

2.1.1 Perovskite distortions

2.1.1.1 Cation Displacement

Perovskites can undergo distortions that play critical role on their properties. Cation displacement is one of the distortions that occur in a perovskite. A cation situated in an anion enclosure will be energetically stable due to the individual contributions from the cations and surrounding anions therefore, the structural stability of the perovskite largely depends on the individual ionic radius of the elements present in the crystal structure [15]. In a situation whereby the cation has a small ionic radius compared to the available anion cage, the system tries to achieve stabilization by displacing the cation out of the center of the cage as shown in the cation displacement of $BaTiO_3$ in Fig. 2.2 [16,17]. The movement of the cation from the center of the octahedral results in the placement of the positive charges from the cations in a certain direction in the crystal thus leading to electrical polarization of the crystal [18]. The displacement between the positive and negative ions in the crystal structure results in an electric dipole moment making the perovskite suitable for ferroelectric applications such as sensors [19, 20]. Helen Magaw in 1945 was among the pioneer crystallographers to study perovskites ($BaTiO_3$) [21, 22], upon solving the crystal structure of $BaTiO_3$ coupled with the discovery of ferroelectric properties of some perovskite oxides, research into perovskites rose leading to the interesting discovery of materials for various industrial applications. The effect of cation displacement is not only limited to charge polarization but also cause phase transition experienced in some perovskites. The phase transition in $BaTiO_3$ from orthorhombic to a tetragonal structure at about -11 °C and from tetragonal to cubic structure at 120 °C is also due to cation displacement [23].

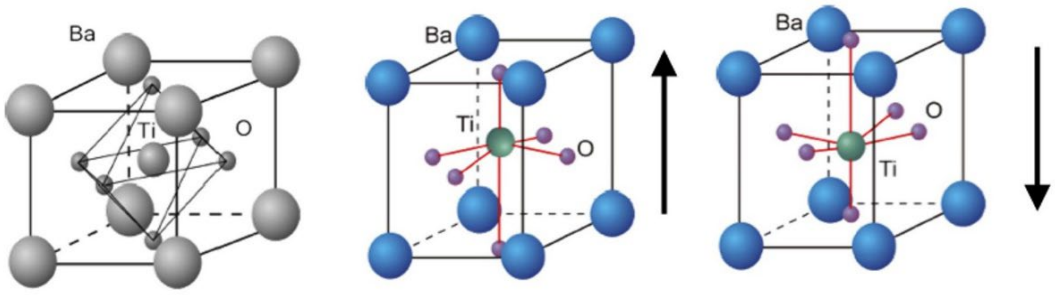

Fig. 2.2: Cation displacement in $BaTiO_3$ perovskites [24].

2.1.1.2 Octahedral distortion

Octahedral distortion in the form of Jahn-Teller (JT) distortion is another type of distortion acting on perovskites. The Jahn-Teller theorem states that "any non-linear molecule possessing a degenerate electronic ground state undergoes a geometrical distortion to eliminate such a degeneracy, to lower the overall energy of the molecule" [25]. Hence, JT distortions deal with the geometrical distortion occurring in a molecule or ions [26, 27]. For instance, the octahedral coordination of perovskite's B cations with the neighboring anions in the BX_6 octahedral usually cause JT distortions when the B cation is a transition metal [28]. The distortion is more pronounced in metal complexes having odd number of electrons occupying the e_g orbitals and examples of such include; high spin d^4, low spin d^7 and d^9 elements [29]. Therefore, for the molecule to become more stable, there is a split in the doubly degenerate energy level further splitting the e_g levels thus lowering the overall energy of the system and consequently lowering the symmetry of the system [15, 30–31]. These distortions can be in the form of elongation and compression of the axial B-X bonds and equatorial B-X bonds respectively or *vice versa*. The lowering of the symmetry caused by distortion may result in the deviation of the perovskite from an ideal cubic structure to lower symmetry such as tetragonal and orthorhombic phase, and such distortion could also be driven by conditions such as temperature and pressure [32–34].

An example of the octahedral distortion can be seen in the $KCuF_3$ perovskite. Cu^{2+} being a transition metal ion in the d^9 group has an electronic configuration with odd numbers of electrons in its e_g level therefore it is expected to undergo a pronounced JT distortion. The distortion in $KCuF_3$ shows that the Cu^{2+} octahedron is distorted to a tetragonal symmetry. Although the direction of the distortion is not always predictable but the elongation and shortening of the bonds are always obvious [35, 36].

2.1.1.3 Octahedral tilting

Ideally, the corner linked BX_6 octahedron is a network of partially flexible joints that allows some rotations or tilting, as a result, when the A cation is too small to fit perfectly in the cuboctahedra site, a slight tilting of the octahedron occur as a mechanism to help attain stability [16]. In other words, octahedral tilting in perovskites is facilitated as a means to achieve stability. The tilts can occur along any of the rotational axes of symmetry. Mike Glazer extensively studied perovskite tilting and discovered the twenty-three possible octahedral tilts

that can occur in a perovskite, where such octahedral tilts majorly influence the lattice parameters of perovskites which in turn determines the overall perovskite symmetry [37].

To predict whether a perovskite will deviate from the ideal cubic structure and distort to other symmetries, Moritz Goldschmidt developed the Goldschmidt tolerance factor as a theoretical calculation for determining the perovskite structure that will be preferentially formed [38, 39]. The Goldschmidt tolerance factor "t" relationship is given in equation 2.1:

$$t = \frac{r_a + r_x}{\sqrt{2}(r_b + r_x)} \tag{2.1}$$

Where r_a, r_b and r_x represent the ionic radii of cations A, B and anion X respectively. Generally, perovskite materials with a tolerance factor within the range of 0.9 – 1.0 adopt the cubic structure, while those in the range of 0.7 – 0.89 adopt distorted perovskite structures [40]. The examples of different perovskites, their t and predicted structures are summarized in Table 2.1. Although the Goldschmidt tolerance factor was designed for oxide perovskites, the trend is still mostly valid for halide perovskites [40].

Table 2.1: Tolerance factor and predicted structure of some perovskite materials

Tolerance factor (t)	Examples	Predicted structure	References
>1	$BaNiO_3$	Hexagonal	[41]
0.95 – 1	$SrTiO_3$, $CaGeO_3$	Cubic	[42]
0.75 - 0.94	$MgTiO_3$ $CsPbBr_3$	Orthorhombic/Rhombohedral	[42, 43]
< 0.75	$LiNbO_3$, $LiTaO_3$	Other structures	[42]

The halide perovskites are similar to the oxide perovskites with the only distinction being the substitution of oxygen with halogens thereby making halide perovskites have the general formula ABX_3. In order to allow the prediction of stability and tendency of forming a cubic structure, a theoretical equation called the octahedral factor "μ" was derived for the halide perovskites. The octahedral factor predicts stability by determining whether the cation B is of the right size to perfectly fit into the B site octahedral to coordinate with the 6 surrounding anions, hence $0.44 < \mu < 0.90$ for a perovskite to adopt the ideal cubic structure [44–46].
The octahedral factor "μ" relationship is given in equation 2.2:

$$\mu = \frac{r_B}{r_x} \tag{2.2}$$

Where r_B and r_x represent the ionic radii of cation B and anion x respectively. Asides from the general ABX_3 perovskites, other perovskite-related structures have been discovered which are discussed in subsequent sections.

2.2 Perovskite related structures

2.2.1 Double perovskite

As the name suggests, double perovskites are a class of perovskites whose unit cell is twice that of an ordinary perovskite with a general formula $A_2B_2X_6$. This formula can be further divided into 2 which are: $A^IA^{II}B_2X_6$ and $A_2B^IB^{II}X_6$ where either the A and B sites are occupied by 2 distinct cations respectively [47, 48]. Since the physical properties of perovskites are majorly influenced by the B cations, the $A_2B^IB^{II}X_6$ type double perovskite is the most common. Double perovskites are particularly interesting to researchers because of the vast combination of elements it affords, resulting in a diversity of applications. Such applications are shown by some examples in Table 2.2. The double perovskites, especially the all-inorganic double perovskites reportedly show higher thermal stability compared to the generic ABX_3 perovskites and this is attributed to the stronger bonding characteristics and the absence of organic moiety in their structure [49]. Despite their impressive thermal stability, the formation of high-quality double perovskite thin films is still a challenge [49].

Table 2.2: Double perovskite materials and their applications

Double Perovskite	Applications	References
Ba_2BiNbO_6, Bi_2FeCrO_6	Hydrogen evolution reactions	[50, 51]
$Cs_2NaTbCl_6$, $Cs_2NaEuCl_6$	X-ray detectors	[52]
$Cs_2AgBiBr_6$, La_2NiMnO_6	Photovoltaics	[53, 54]
$Cs_2AgBiBr_6$, $Cs_2AgInCl_6$	Photodetectors	[55, 56]

2.2.2 Layered Perovskite

Asides from the double perovskite, a class of layered perovskites also exists, such layered perovskites include: (i) the Ruddelsden-popper phase (ii) Aurivillius phase and the (iii) Dion Jacobson perovskites [57–59]. The Ruddelsden-popper phase has the formula $(A_2)A^I_{(n-1)}B_nX_{(3n+1)}$ where n represents the size of the 2D slabs [60]. This layered perovskite has regular slabs of ABX_3 perovskite but is separated by a particular group or motif. An example of the

Ruddesden-popper phase perovskite is $(BA)_2(MA)_2Pb_3I_{10}$ where the BA act as the separating motif and this perovskite has been useful for photovoltaic applications [61, 62]. The Aurivillius phase is similar to that of the RP phase but the separating motif is a rock-salt like Bi_2O_2 layer [63]. Aurivillius phase is categorized with the formula $(A^I_2X_2)(A_{n-1}B_nX_{3n+1})$ where the $A^I_2X_2$ rock salt configuration is the separating motif [64, 65]. An example of the Aurivillius perovskite is Bi_3TiNbO_9 which is used in piezoelectric application [66, 67]. Lastly, the Dion-Jacobson perovskite phase with a formula $A^I(A_{n-1}B_nX_{3n+1})$ is also a layered perovskite for numerous applications, it however differs from the other layered perovskite by having an alkali metal as its separating motif. Although the different forms of perovskites have been discussed, it is equally necessary to discuss the properties of these materials that make them ideal semiconductors for a plethora of applications.

2.3 Properties of perovskite

2.3.1 Bandgap

Bandgap energy is one of the most important parameters to consider when selecting a material for optoelectronic applications. Solid materials, based on their energy transport properties can be categorized as (i) conductors, (ii) semiconductors and (iii) insulators. Conductor materials have an overlap of their valence and conduction bands hence electrons can move freely across the material, while insulators have such a high energy gap between the valence and conduction bands that electrons cannot be injected into the conduction band [68, 69]. However, semiconductors possess electrical conductivity between that of an insulator and a conductor. The optimum bandgap energy of perovskite is an interesting feature that makes halide perovskites excel as an absorber layer. Halide perovskites generally have a direct bandgap which is tunable between 1.1 - 1.9 eV making them favorable for solar applications [70–72]. However, higher bandgaps exceeding 1.9 eV have been recorded in other perovskite related structures which consequently increases the versatility of perovskites. The ease of doping of perovskites also further makes bandgap tuneability seamless.

2.3.2 Diffusion length

Diffusion length is the average distance charge carriers can cover before they recombine. The diffusion lengths which can be determined by photoluminescence quenching measurements strongly depend on the lifetime and mobility of the carriers. Perovskites generally possess a high diffusion length which sometimes exceeds 1 μm [73]. This high intrinsic diffusion length

helps prevents fast recombination of holes and electrons which consequently leads to an efficient solar cell [73, 74].

2.3.3 Absorption coefficient

High absorption coefficient is also another interesting feature of perovskites, as it determines how deep light of a specific wavelength can penetrate a material before its absorption. The higher the absorption coefficient, the thinner the absorber layer can be fabricated to absorb solar radiation effectively. The perovskite absorber layer has been reported to have an absorption coefficient that is remarkably higher than that of crystalline silicon material hence thinner perovskite film is sufficient to efficiently absorb the solar radiation [75].

2.4 The transition from organic-inorganic perovskite to all-inorganic perovskite

The photovoltaic (PV) application is perhaps the most ubiquitous application of halide perovskites. This particular application of perovskites started in the early 2000s when Miyasaka and coworkers in 2006 used halide perovskite as a component of a dye-sensitized solar cell [76, 77]. After the initial work of Miyasaka *et al*., [76] an improved efficiency was recorded in 2009 by the same group and in 2011, perovskite's power conversion efficiency (PCE) was over 6.5 % [78, 79]. Originally, the PV application of perovskites started with the organic-inorganic halide perovskites (OIHPs) such as the methylammonium lead iodide ($CH_3NH_3PbI_3$) where the organic component (CH_3NH_3) is the cation A [80]. These halide perovskites readily dissolve in the liquid electrolyte used, thereby inhibiting their stability and PCE [81]. The introduction of a solid-state hole transport layer 2,2',7,7'- tetrakis (N,N-di-p-methoxyphenylamine)-9,9'-spirobifluorene (spiro-OMeTAD) as a replacement for the previously used liquid electrolyte led perovskite solar cell to attain an impressive record efficiency of 10.9 % [82, 83]. Despite their impressive performance, perovskites are notoriously unstable because they degrade under oxygen and moisture thus inhibiting their outdoor application [84–86]. The OIHPs are particularly sensitive to water as they easily hydrolyze in a moisture-rich environment. For instance, $CH_3NH_3PbI_3$ rapidly decomposes to CH_3NH_3I and PbI_2 in the presence of moisture. Such degradation occurs as expressed in equations 2.3 and 2.4 [87]:

$$CH_3NH_3PbI_{3(s)} \leftrightarrow PbI_{2(s)} + CH_3NH_3I_{(aq)} \quad (2.3)$$

$$CH_3NH_3I_{(aq)} \leftrightarrow CH_3NH_{2(aq)} + HI_{(aq)} \quad (2.4)$$

The HI formed is degraded either in the presence of oxygen or through photochemical reduction as shown in equations 2.5 and 2.6.

$$4HI_{(aq)} + O_{2(g)} \leftrightarrow 2I_{2(s)} + 2H_2O_{(l)} \quad (2.5)$$

$$2HI_{aq} \leftrightarrow H_{2(g)} + I_{2(s)} \quad (2.6)$$

Such degradation is not unique to iodides but also affects the chloride and bromide perovskites albeit to a lesser extent.

Another route of perovskite decomposition was proposed by Kelly *et al.,* [88] who studied the mechanistic degradation of OIHP through in-situ techniques. The study showed that an intermediate phase identified as a monohydrate phase is first formed during the decomposition process [88, 89] whereby hydrogen bonds exist between the A cation (methylammonium) and H_2O molecules. Such interaction effectively transforms the perovskite into 2-dimensional sheets segregated by the H_2O molecules, this step is then proceeded by the isolation of the PbI_6^{4-} octahedra consequently leading to the formation of Pb byproducts such as PbO and $Pb(OH)_2$ [90, 91].

It was later observed that the use of mixed halide $CH_3NH_3PbI_{3-x}Cl_x$ not only enhanced the charge carrier properties of the perovskites but also improved the stability of the mixed halide perovskite over its pure iodide counterpart [73, 83]. Further research into the composition engineering of perovskites revealed that the use of bromine (Br) in perovskites greatly improved stability and efficiency [92, 93]. Kang *et al.* [94], observed that upon the addition of bromine into an iodide perovskite, the crystallinity quality of the perovskite was enhanced while suppressing the trap-mediated recombination process. Asides from stability, toxicity is another challenge of perovskites. Most studied and highly efficient perovskites are Pb-based, but the toxicity of Pb is a major concern for the large-scale application and deployment of perovskites. Pb toxicity even at minute levels has been known to cause renal failure in humans since Pb is majorly removed from the body through the kidney hence, nephrotoxicity occurs from lead ingestion [95,96]. Furthermore, early life exposure to Pb has been reported to contribute to over 500,000 cases of impaired brain development [96,97]. The Pb noxiousness emerges from its ability to hinder antioxidant enzymes such as glutathione reductase where it forms covalent linkages with the functional sulf-hydryl groups of such enzymes consequently making them non-functional [98]. Also, the Pb ability to mimic Ca allows it to cross the blood-

brain barrier and concentrate in the brain where it interferes with glutamate which is a neurotransmitter essential for brain development [99].

The ease of degradation of OIHP primarily due to the weakly bonded organic constituents led to the substitution of the organic components (cation A) of the perovskite with inorganic cations with similarly large ionic radius (cesium and rubidium) thus forming an all-inorganic halide perovskite. The substitution of the A organic cation with inorganic cesium (Cs) results in tunable formation energy of the perovskite resulting in a more stable perovskite [100–102]. This stability was further proven theoretically by Zhang *et al.,* [100,101] who determined the thermodynamic stability of the inorganic perovskites through Gibbs free energy calculations. The study revealed that the different possible orientations of methylammonium (MA) in the halide perovskites lead to higher configurational entropy which affects the overall stability of the OIHPs. However, the substitution of MA with a symmetric cation (Cs) without variable configurations eliminates the influence of configurational entropy in the all-inorganic halide perovskite translating to improved stability. Another factor responsible for the enhanced stability of Cs-based perovskites is the absence of free acid protons in the system thus making the inorganic perovskites more tolerant to superoxides (O_2^-) which have been reported to initiate the degradation reactions of OIHPs [86, 100, 103].

Due to the aforementioned toxicity and stability issues of perovskites, Pb-free perovskites are gaining attention. Despite several elements being proposed as Pb substitute, tin (Sn) is one of the most promising of these elements since Sn satisfies the ionic size, coordination and charge balance prerequisites [104]. Tin is an ideal substitute for Pb not only because they are in the same group of the periodic table but because they also have a relatively similar ionic radius (r_{ion}) with Sn^{2+} (r_{ion} 115 pm) and Pb^{2+} (r_{ion} of 119 pm) [105, 106]. In the Sn-based halide perovskite ($CsSnBr_3$), the unstable MA and highly toxic Pb are replaced with Cs and tin (Sn) respectively. $CsSnBr_3$ is a direct bandgap semiconductor with a bandgap energy of about 1.85 eV [107]. This perovskite like most other perovskites undergoes phase transitions due to the condensation of the rotational modes of $SnBr_6$ octahedra leading to a closer packing hereby slightly distorting from the ideal cubic structure [108]. The $CsSnBr_3$ is cubic with space group *Pm3m* at 25 °C, but transition to tetragonal *P4/mbm* just below 19 °C [108]. Subsequently, it was discovered that further transitions occur at lower temperatures. Mori *et al.,* [109] found out that after the initial transition at 19 °C, the tetragonal *P4/mbm* transition to tetragonal $P42_12$ at 1 °C and then to the monoclinic phase at -26 °C. The electronic property of $CsSnBr_3$ is shown

in Fig. 2.3 where the valence band maximum and the conduction band minimum are both situated at the R symmetry point confirming that the material has a direct bandgap [110]. The $CsSnBr_3$ material has been reported to have improved thermal stability over its organic counterparts as it only starts to thermally degrade at about 430 °C [111].

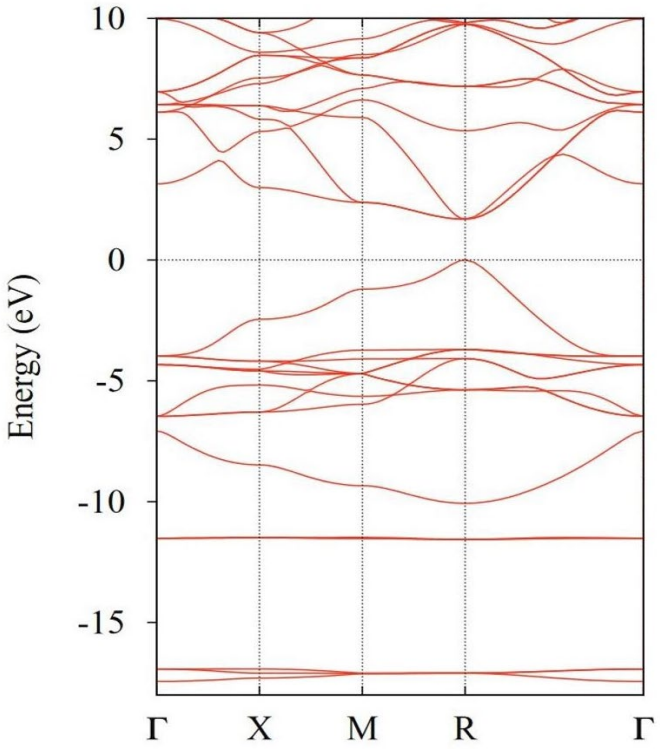

Fig. 2.3: The electronic band diagram of $CsSnBr_3$ [110].

Asides from Sn, bismuth (Bi) is another potential substitute for lead because Bi^{3+} is isoelectronic to Pb^{2+} and it has a lower toxicity than Pb [112, 113]. Due to the dominant +3 oxidation state of Bi [114], the Bi-based perovskites are structured as $A_3Bi_2Br_9$ where there is a replacement of three Pb^{2+} cations with two Bi^{3+} cations [115]. The Bi-based perovskite crystallizes into the P3m1 space group and adopts the layered, vacancy ordered $A_3Bi_2X_9$ configuration with one-third of the octahedral B^{3+} sites unoccupied to preserve charge neutrality [116]. The electronic band diagram of $Cs_3Bi_2Br_9$ is shown in Fig 2.4. The band diagram shows a low-lying 2.52 eV indirect transition originating from the Γ point to A. This is accompanied by a moderately larger direct gap of 2.64 eV [117].

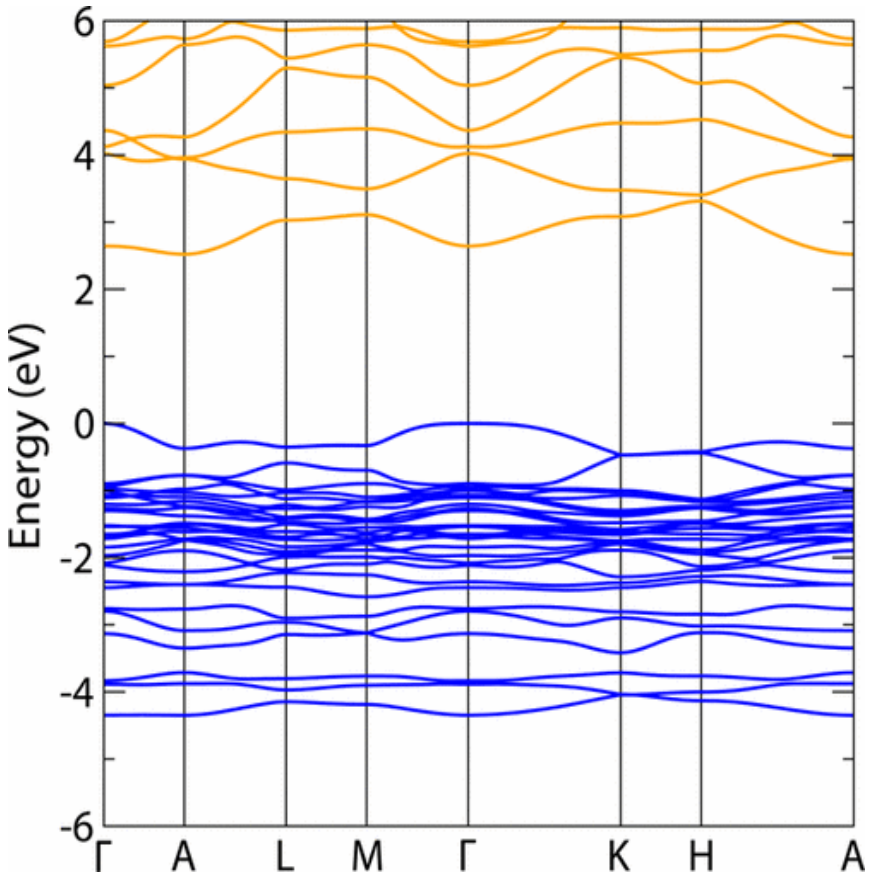

Fig. 2.4: The electronic band diagram of $Cs_3Bi_2Br_9$ [117].

Finally, zinc (Zn) is another cation that is gaining recognition as a substitute for lead in perovskites. Zn is a transition element with a normal oxidation state of +2. Although Zn has a smaller ionic radius compared to Pb, it is however a stronger Lewis acid than Pb and is amphoteric in nature [118]. Recently, Zn^{2+} was introduced into an organic perovskite, the study revealed that upon addition of Zn^{2+}, a better film quality with fewer trap state density was observed which consequently improved the efficiency of the device from 12.1% to 16.3% [118]. To efficiently utilize the interesting properties of perovskites in different electronic and optoelectronic devices, it is important to investigate their behavior when in contact with metals since most applications of perovskites will involve the fabrication of the perovskite layer on a metal or conducting substrate. Section 2.5 discusses the different types of contacts between a semiconductor and a metal, this section also elucidates how the interface between these dissimilar materials can be used to probe the electrical properties of the perovskite semiconductor.

2.5 Insights into the metal/semiconductor interface

Asides from the optical properties and other interesting properties of perovskites previously discussed, harnessing these semiconductors for solar cell devices or other electronic and optoelectronic applications will require the understanding of contact formed between the metal and the perovskite. Generally, such metal–semiconductor contact is of two forms namely (i) the ohmic contact and (ii) the Schottky contact [119].

2.5.1 Ohmic contact

The ohmic contact is a non-rectifying contact that has current–voltage (*I-V*) characteristics that follow Ohm's law (*V=IR*) [120]. The ohmic contact possesses low resistance with its I-V characteristics showing linearity regardless of the applied voltage signal [120]. Fig. 2.5 shows the contact between a metal and a semiconductor. In this system, the Fermi level of the metal (Ef_M) is higher than that of the semiconductor (E_F) where the energy band of the n-type semiconductor bends downwards towards the contact. Since the magnitude of the band bending is negligible, there is practically no potential barrier between the metal and the semiconductor therefore, electrons move unhindered through the contact [121].

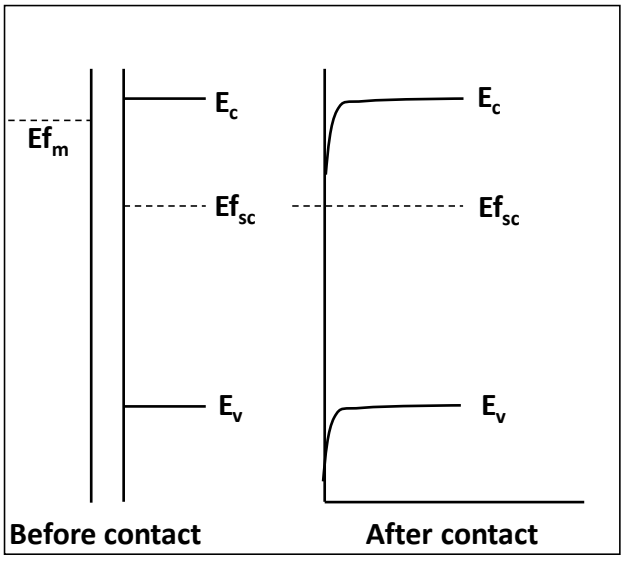

Fig. 2.5: Energy bands of an ohmic contact.

2.5.2 Schottky contact

The electrical characteristics derived from the metal-semiconductor (M-S) contact are important characterization largely studied for their physical properties and technological

applications in electronic, optoelectronic and electrochemical devices. These M-S contact can either be a rectifying contact or non-rectifying. The rectifying contact also called the Schottky contact or Schottky diode shows a non-linear current-voltage characteristic when changing the polarity of the applied voltage [122]. This rectifying effect in the M-S contact was discovered by a German electrical engineer named F. Braun in 1874 [123]. However, this effect was only properly explained in 1938 by Schottky and Mott [121]. The Schottky contact allows the flow of current in one bias direction (forward bias) while blocking current in the opposite bias direction (reverse bias) [121]. This behavior indicates a high current resistance in the reverse-bias. One of the most important attributes of the Schottky contact is the barrier height since the barrier height is responsible for the characterization of the electronic properties of the M-S contact.

2.5.2.1 Schottky barrier formation

The deposition of a metal onto the surface of a semiconductor leads to the formation of a potential barrier at the M-S surface [121]. From the energy band diagram of a metal and a semiconductor in Fig. 2.6, the conduction band of the semiconductor is higher than the Fermi level of the metal. Considering an n-type semiconductor and a metal. Upon contact of the metal and the semiconductor, the Fermi levels of both the metal (Ef_M) and the semiconductor (Ef_{SC}) align to reach a thermodynamic equilibrium which is formed through the electron transfer from the conduction band of the semiconductor (E_C) into the metal due to the $E_C > Ef_M$ [121].

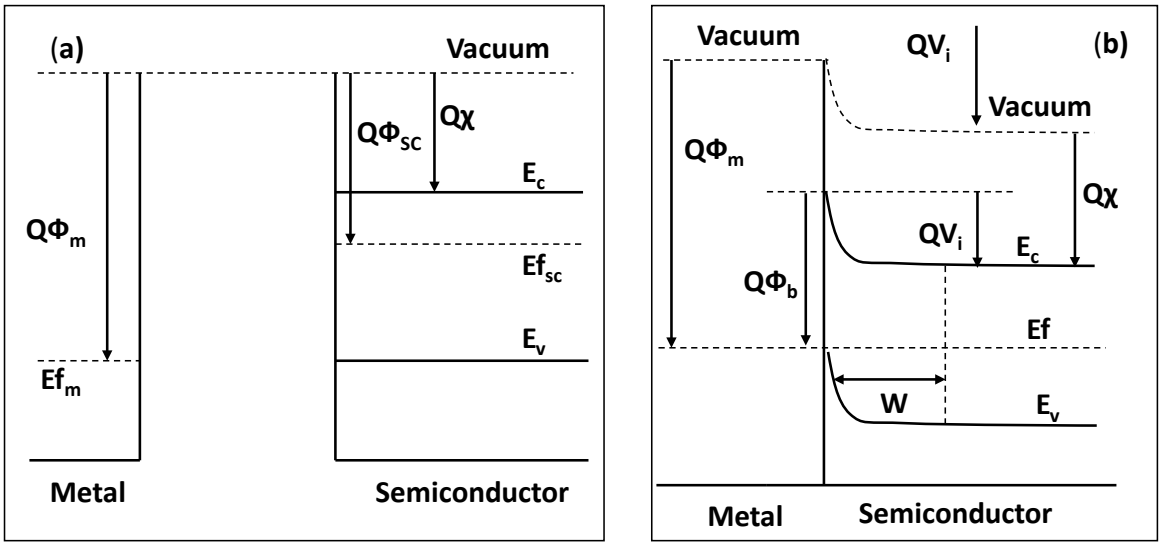

Fig. 2.6: (a) Energy bands in a metal and a semiconductor (b) Energy band diagram of the Schottky contact.

Due to the electron flow, there exists a negative charge buildup on the metal surface accompanied by a concomitant positive charge buildup on the semiconductor consequently causing an electric field in the gap between the metal and the semiconductor [121]. A space-charge region characterized by electron depletion is formed in the semiconductor close to the metal interface. The width of this region is denoted as W_0. Due to the metal and semiconductor Fermi levels alignment and the presence of the depletion region, semiconductor band curvature (QV_i) equals:

$$QV_i = Q(\emptyset_m - \emptyset_{SC}) \tag{2.7}$$

Where $Q\emptyset_m$ and $Q\emptyset_{SC}$ represents the metal and the semiconductor's work function respectively. This curvature represented by V_i corresponds to the potential barrier inhibiting the electron migration into the metal. In contrast, electrons in the metal see a potential barrier ($\emptyset_b$) which equals:

$$Q\emptyset_b = Q(\emptyset_m - \chi) = QV_i + (E_c - E_f) \tag{2.8}$$

Where χ represents the electron affinity and E_f is the aligned Fermi level.

At room temperature, these potential barriers are remarkably larger than the thermal voltage and only little electrons have enough energy to overcome them. The current derived due to the migration of electrons from the semiconductor into the metal upon overcoming the barrier is notated as $I_{M \rightarrow S}$. This notation signifies the negative charge (electrons) migration from the semiconductor into the metal and this process corresponds to a positive flow of current from the metal into the semiconductor. At thermal equilibrium and without external bias, the current $I_{M \rightarrow S}$ is completely balanced by a current of electrons flowing into the semiconductor from the metal $I_{S \rightarrow M}$. Therefore, under equilibrium conditions, $I_{S \rightarrow M} = - I_{M \rightarrow S}$. If a forward bias ($Va > 0$) is introduced into the system, the potential barrier at the semiconductor side decreases from V_i to $V_i - V_a$ allowing numerous electrons to flow into the metal from the semiconductor. However, $I_{S \rightarrow M}$ remains constant since the potential barrier from the metal side $\emptyset_b$ is the same. Contrastingly, if a reverse bias $V_a < 0$ is introduced the potential barrier in the semiconductor increases from V_i to $V_i - V_a$ therefore $I_{M \rightarrow S}$ is reduced while $I_{S \rightarrow M}$ remains constant. This

asymmetry between the forward and reverse current flow produces the non-linear current-voltage characteristics.

2.5.2.2 Measurement of the barrier height

Due to its simplicity, the current-voltage measurement is among the most common way to determine the Schottky barrier. Due to thermionic emission, the electrons overcome the barrier between the metal and the semiconductor, this process is prompted by the electrons' thermal energy. Despite the thermal energy been smaller than the potential barrier at room temperature, there is still a probability that a very small amount of electrons will accumulate sufficient energy to overcome the barrier. If a forward bias V_a is applied to the device, the potential barrier that must be surmounted by the electrons to move to the metal from the semiconductor is given as $\emptyset_b^i - V_a$. Therefore, the resulting thermionic emission current is expressed as:

$$\mathrm{I}_{\mathrm{M}\rightarrow\mathrm{S}} = AR^*T^2 \exp\left[-\frac{q(\Phi_b^i - \mathrm{V_a})}{kT}\right] \tag{2.9}$$

Where R^* is the Richardson constant and A is the diode area.

Since $\mathrm{I}_{\mathrm{S}\rightarrow\mathrm{M}} = -\mathrm{I}_{\mathrm{M}\rightarrow\mathrm{S}}$ when $V_a = 0$ and also, since $\mathrm{I}_{\mathrm{S}\rightarrow\mathrm{M}}$ is constant and independent of the applied voltage. Therefore:

$$\mathrm{I}_{\mathrm{S}\rightarrow\mathrm{M}} = -AR^*T^2 \exp\left[-\frac{q(\Phi_b^i - \mathrm{V_a})}{kT}\right] \tag{2.10}$$

Since the overall current in the diode is $\mathrm{I}_{\mathrm{S}\rightarrow\mathrm{M}} + \mathrm{I}_{\mathrm{M}\rightarrow\mathrm{S}}$

$$I = AR^*T^2 \exp\left[-\frac{q(\Phi_b^i - \mathrm{V_a})}{kT}\right]\left[\exp\left(\frac{qV_a}{kT}\right) - 1\right] \tag{2.11}$$

$$I_0 = AR^*T^2 \exp\left[-\frac{q(\Phi_b^i - \mathrm{V_a})}{kT}\right]\left[\exp\left(\frac{qV_a}{kT}\right) - 1\right] \tag{2.12}$$

Therefore,

$$\mathrm{I} = \mathrm{I_0}\left[\exp\left(\frac{qV}{nkT}\right) - 1\right] \tag{2.13}$$

Where n is the diode ideality factor, q is the electronic charge, k is Boltzmann constant, T is the ambient temperature. The plot of InI against V gives a straight line and the value of $\mathrm{I_0}$ can be extrapolated from the straight line to $V = 0$.

2.5.3 Transport mechanism in a Schottky diode

The flow of current in a Schottky diode is due to the charge transport from the semiconductor to the metal or *vice-versa*. As a result, the carrier transport in the Schottky diode can transpire *via* four different mechanisms**.** These mechanisms are discussed in the subsequent sections.

2.5.3.1 Thermionic emission over the barrier

The original theory about the conduction process in a Schottky diode was the diffusion theory postulated by Wagner, Schottky and Spenke [124]. Summarily, this theory postulated that electrons emission into the metal is influenced by the density of states available in the metal where such electron migration to the metal must be transported through the depletion region. While migrating through this region, the motion of the electron is determined by the drift and diffusion process. Subsequently, Bethe [125] proposed that the electron's Fermi levels are constantly horizontal across the depletion zone. As a result, the thermionic emission theory was conceptualized and it postulated that " only charge carriers with energies greater than the potential barrier can overcome the barrier to generate the diode current" [126]. The ideal *I-V* characteristics of a Schottky diode is given as:

$$I = I_0 \left[\exp\left(\frac{qV}{kT}\right) - 1\right] \tag{2.14}$$

Where I_0 is the saturation current

$$I_0 = AA^{**}T^2 \exp\left[-\frac{\Phi_B}{kT}\right] \tag{2.15}$$

Where A^{**} is the effective Richardson constant for thermal emission.

2.5.3.2 Tunneling through the barrier

This is another mechanism in which current flows in a Schottky diode. Due to certain circumstances (doping and low temperature), electrons with energies lower than the barrier height may pass through the barrier by quantum-mechanical tunneling. This quantum-mechanical tunneling happens in severely doped semiconductors such that the Fermi level is positioned above the bottom of the conduction band hereby causing a very thin potential barrier. Because of the combined effect of the thin potential barrier and low temperature, electrons whose energies are near the Fermi levels can tunnel to the metal from the semiconductor. This form of tunneling is termed field emission. If the temperature is slightly

increased, there is electron excitation to higher energy which results in higher tunneling probability since the electrons experience a thinner and lower barrier. However, if the temperature is further increased, ultimately, all the electrons will possess enough energies to overcome the barrier hence the tunneling effect is insignificant and the process becomes pure thermionic emission.

2.5.3.3 Generation and recombination mechanisms

The generation and recombination of electron pairs in the depletion zone can also be responsible for the current component in a Schottky device. The rate of electron-hole pair generation equals the rate of recombination in the depletion region of the Schottky barrier at thermal equilibrium under zero bias. Therefore, the electron-hole product equals n_i^2. However, when an applied voltage is present, the electron-hole product deviates from n_i^2 causing a net generation or net recombination of current depending on the applied bias polarity. Assuming it is an n-type semiconductor and a reverse bias is applied, the electron-hole pairs generation will increase in the depletion region. These pairs will be ejected from the depletion region by the barrier's electric field consequently producing the reverse saturation current. Contrarily, if the diode is forward biased, electrons injection from the neutral bulk of the semiconductor into the depletion region will occur, causing ejection of holes from the metal. The electrons will recombine with the holes due to their buildup in the depletion region to produce a forward recombination current. These recombination centers in semiconductors are most effective when its energy levels are close to the center of the bandgap. The generation recombination current (I_{rg}) in the depletion region is given by:

$$I_{rg} = I_{ro}\left[\exp\left(\frac{qV}{2kT}\right) - 1\right] \tag{2.16}$$

with

$$I_{ro} = \frac{qn_iW}{2\tau_0} \tag{2.17}$$

Where τ_0 is the carrier lifetime in the depletion region while is W the thickness of the depletion region. This current is added to the thermionic emission current and may sometimes be responsible for ideality factor greater than 1.

2.5.3.4 Minority carrier injection

The Schottky barrier is a majority carrier device. However, usually, the barrier height of an n-type semiconductor is significantly higher than half the bandgap of the semiconductor. When this happens, the semiconductor region that is adjacent to the metal will possess high concentration of holes thus becoming p-type. Under the influence of a forward bias, the electrons flow into the metal from the semiconductor and some of the holes diffuse into the neutral zone of the semiconductor. This causes the injection of holes from the metal to the semiconductor. These injected holes gradually disappear by recombining with electrons. If the concentration of holes is higher that of the electrons, then the surface becomes inverted and forms a p-n junction with the bulk. Upon a comprehensive theoretical understanding of perovskites and their behavior with a metal contact, it is important to discuss the techniques of synthesizing these versatile materials. Section 2.6 explains different routes of semiconductor synthesis.

2.6 Synthesis of perovskites

The rising interest in the study of perovskites has led researchers to explore numerous synthetic routes to produce these nanoparticles (NPs), some of such routes are discussed in this section. Generally, NPs synthesis is broadly grouped into two approaches, which are; the top-down and bottom-up approaches [127–129]. The bottom-up approach deals with the addition of building blocks where the NPs are built up atom by atom or as constituent molecules [130]. Contrarily, the top-down approach involves the removal or breakdown of the bulk material to the required NPs [130] as illustrated in Fig. 2.7.

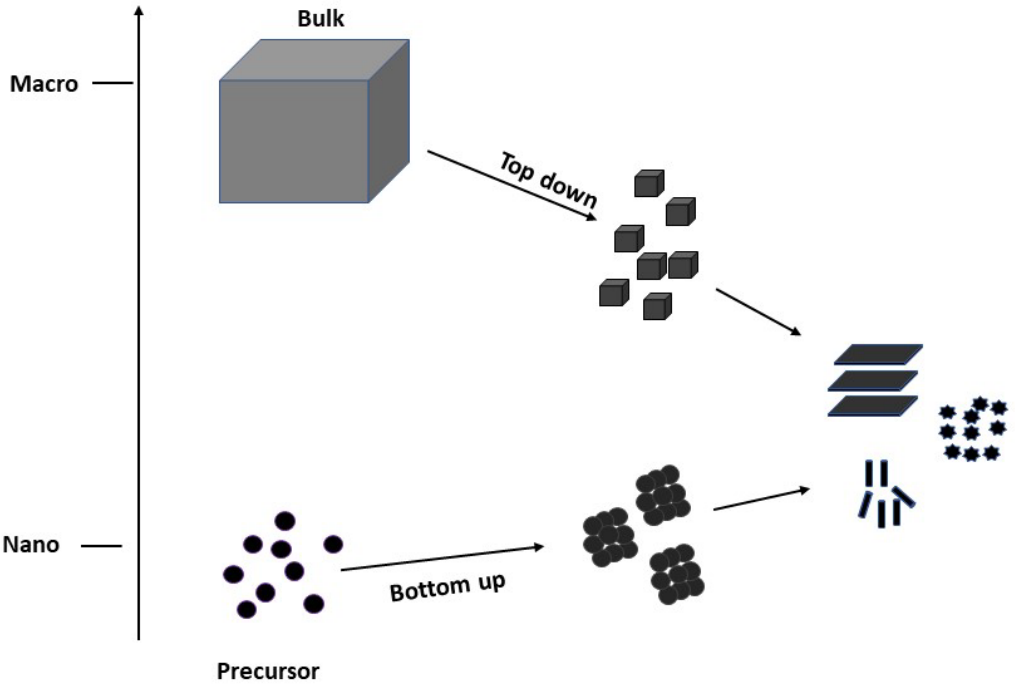

Fig. 2.7: Schematic illustration of the bottom-up and top-down approaches of NPs syntheses.

2.6.1 Top-down synthetic route

2.6.1.1 Ultrasonic exfoliation technique

This form of top-down synthesis requires the aid of soundwaves in the exfoliation of the bulk material [131]. In this process, the generated soundwaves are propagated through a liquid medium to produce microbubbles which are energised till they implode by a process called cavitation [132]. The cavitation occurs beside the bulk material causing the formation of fast-paced liquid jets which cuts into the bulk material while also weakening the intermolecular forces of the material due to the damaging effects of the shockwaves generated [132, 133]. This bond weakening eventually increases the interlayer spacing of the material so the stacked sheets can be exfoliated. This particular technique has been very useful for the synthesis of graphene sheets [134, 135]. Recently, layered perovskites have also been synthesized with this technique [136, 137].

2.6.1.2 Lithographic technique

This is another example of a top-down synthetic approach which involves the use of substrates or plates for printing. Lithography means *lithos* (stone) and *gráphien* (to write), hence the process deals with the transfer of ordered shapes onto the surface of a material [138]. The lithographic techniques use UV light, electrons and x-rays to imprint an image containing the desired pattern onto a surface [139]. Depending on the type of radiation used, a series of lithographic techniques exist which include photolithography, ion-beam lithography and x-ray lithography [140, 141]. Photolithography is perhaps the most common form of all lithographic techniques and it has been very useful in the electronics industry where computer-designed shapes are transferred onto a substrate such as silicon and glass [142]. In the photolithographic process, chemical cleansing of the substrates is done to remove impurities, followed by the deposition of a barrier layer (silicondioxide) on the cleaned substrate's surface. After successfully depositing the barrier layer, a photoresist layer possessing high sensitivity to UV light is then deposited on the substrate's surface [143]. Following photoresist deposition, the wafer is soft-baked at a moderately high temperature to remove residual solvent which would have otherwise affected the substrate-resist layer adhesion. After the soft baking process, the coated wafers are moved to an illumination system where the alignment of masks with the substrate's surface is done. In the illumination system, light of specific wavelengths and spectral properties are used to perfectly transfer the mask image onto the resist in the form of a latent image [144]. While lithographic techniques have been used for years in the electronics industry where the precision of internal circuit is a necessity, perovskites are also gradually getting fabricated with this technique [145, 146].

2.6.2 Bottom-up synthetic approach

2.6.2.1 Sol-gel method

The sol-gel method of NP synthesis is a technique used to produce solid materials from small molecules. In this synthetic approach, the solution slowly transforms into a gel-like substance where the starting solution in such synthesis is usually a metal alkoxide or an organometallic compound [147]. A sol is a steady dispersion of colloids in a particular solvent while the gel is a semi-solid substance containing a three-dimensional framework enclosing a liquid phase [148, 149]. The sol-gel method generally involves three steps which are; hydrolysis, condensation and gelation.

2.6.2.1.1 Hydrolysis

The hydrolysis step allows the attachment of hydroxy (OH^-) ions to the metal atoms present in the precursor material, often using a controlled temperature and in the presence of a catalyst. For an alkoxide based precursor, the hydrolysis reaction is expressed in equation 2.18 [150].

$$M(OR)_4 + nH_2O \rightarrow M(OR)_{(4-n)}(OH)_n + nHOR \quad (2.18)$$

2.6.2.1.2 Condensation

The condensation process allows for the liberation of water molecules as a step towards the formation of larger molecules. The condensation reaction is given as equation 2.19 [150]:

$$2M(OR)_{(4-n)}(OH)_n \rightarrow \left(M(OR)_{(4-n)}(OH)_{(n-1)}\right)_2 O + H_2O \quad (2.19)$$

The larger molecules are formed through the polymerization process whereby there is a condensation of neighbouring molecules followed by the elimination of water.

2.6.2.1.3 Gelation

This is the last step in the sol-gel process. Through a polycondensation step, a structure of high cross-linking termed gel is formed [151]. Increasing the pH of the sol precursors will aid in the formation of a gel where the gel formation can be due to *Van der Waals* forces or covalent bonds. Aging of the gel can also be done as an advanced step to help reinforce the gel [148].

2.6.2.2 Colloidal synthesis

In colloidal method of synthesis, organometallic precursors or inorganic salts are dissolved or decomposed in solution to produce NPs of interest. Such transformation of precursor materials to NPs occurs in the liquid phase through precipitation reaction which allows for the controlled growth process to help yield high-quality NPs [152, 153]. The thermal dissolution or decomposition of the starting materials raises the concentration of the inherent elements in a short period, causing a short nucleation event and then proceeds by a slower growth regime. Oftentimes, the precursors are separately injected into the reaction vessel to allow the nucleation process occur at an even narrower time frame. Perovskite materials like most other semiconductor nanomaterials have their optoelectronic properties largely dependent on their sizes and morphology [154–156]. Therefore, to further understand these fascinating materials and efficiently utilize their intrinsic properties, a synthetic approach that allows for the

manipulation of NP surface chemistry coupled with a seamless size and shape optimization is of utmost importance to the halide perovskite field. Colloidal synthesis is one of such synthetic methods. To fully comprehend the colloidal synthesis route, it is important to discuss the steps (nucleation and growth process) involved in NP synthesis.

2.6.2.2.1 Nucleation

The nucleation process which can either be homogenous or heterogenous is the first step towards the production of nanoparticles. Most theoretical work on nucleation using equilibrium thermodynamics are established on the classical nucleation theory which was first developed by Becker and Döring [157]. The concept of the theory is summarized that, a thermodynamic system will be inclined to minimize its Gibbs free energy [157]. Nucleation is the process whereby molecules, atoms or ions aggregate from a liquid or gas phase to form a nucleus, which is the site where other particles can agglomerate to form crystals [158, 159]. The homogenous nucleation process involves the spontaneous and randomized formation of a nucleus from a supersaturated solution without the need for a nucleation site, contrarily, heterogenous nucleation requires a nucleation site [160]. In the homogenous nucleation, the Gibbs free energy of the nucleus is denoted as the sum of two terms which are the positive and negative terms, where the negative term expresses the decrease in Gibbs free energy due to the favorable bonding between a monomer and a cluster or between two monomers [161–163]. On the other hand, the positive term represents an increase in the Gibbs free energy due to the unfavorable bonding of a monomer [164]. The Gibbs free energy of a spherical cluster is given as;

$$\Delta G = -\frac{4}{3}\pi r^3 |\Delta G_v| + 4\pi^2\gamma \qquad (2.20)$$

Where r is the radius, $|\Delta G_v|$ represents the difference in Gibbs free energy per unit volume and γ is the surface energy per unit area.

Since the change in the Gibbs free energy is due to bond formations, there is a competition between the negative (favorable formation of bond) and the positive (surface energy) terms. Beneath a critical size that has a corresponding critical radius (r_c) and activation energy (ΔG_c), growth is unfavorable and the system is propelled towards dissolution. However, when the cluster has a radius greater than r_c, growth is favored because the negative volume energy decrease is higher. A plot showing the relationship between the Gibbs free energy and the

critical radius is shown in Fig. 2.8 where the effect of surface energy and bulk Gibbs free energy on the positive and negative term respectively is also presented.

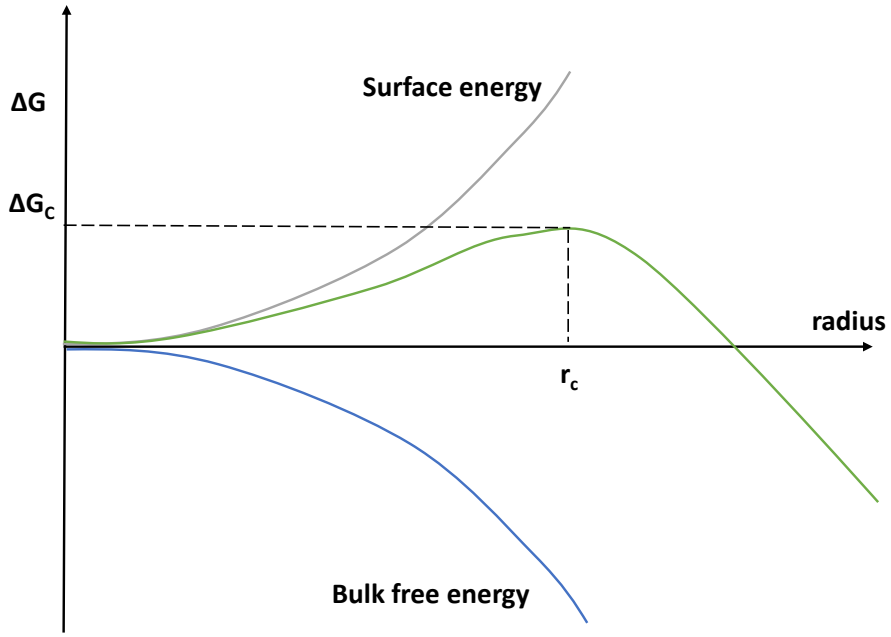

Fig. 2.8: A plot of the Gibbs free energy against the radius of the clusters.

The critical radius is given as

$$r_c = \frac{2\gamma}{|\Delta G_v|} \tag{2.21}$$

While the activation energy is given as

$$\Delta G_c = -\frac{16\,\pi\gamma^3}{|\Delta G_v|^2} \tag{2.22}$$

The rate of nucleation $J(T, \Delta G_c)$ is determined using the Arrhenius equation because the energy barrier relates to the activation energy.

$$J(T, \Delta G_c) = A\ exp\left(\frac{-\Delta G_c}{K_B T}\right) \tag{2.23}$$

LaMer, working on the theory of Becker and Doring in the 1950s applied the idea of classical nucleation theory to NP synthesis and formulated the theory of burst nucleation [165, 166]. In the LaMer's theory (Fig. 2.9), the nucleation process follows the homogenous method whereas the growth process is believed to be a heterogeneous process [167]. In the burst nucleation process, the production of nuclei occurs simultaneously as a result of homogenous nucleation

whereby succeeding growth process can occur without further nucleation. The LaMer's theory can be explained with three mechanisms [168].

1. Upon attainment of a critical temperature or due to instantaneous injection of precursors, the precursors will transform into monomers where the monomer concentration increases until the critical supersaturation of monomer concentration (C_s) is attained in the solution.
2. The saturation continually increases and attains a concentration level (C_{min}) where the energy barrier for nucleation can be overcome, resulting in a brisk self-nucleation process termed "burst nucleation". Consequently, the monomer concentration drops, lowering the saturation and eventually ending the nucleation regime.
3. Due to the nucleation cessation, the remaining monomers in solution diffuse and affix to the existing nuclei for growth hence this stage can be perceived as a heterogeneous growth process.

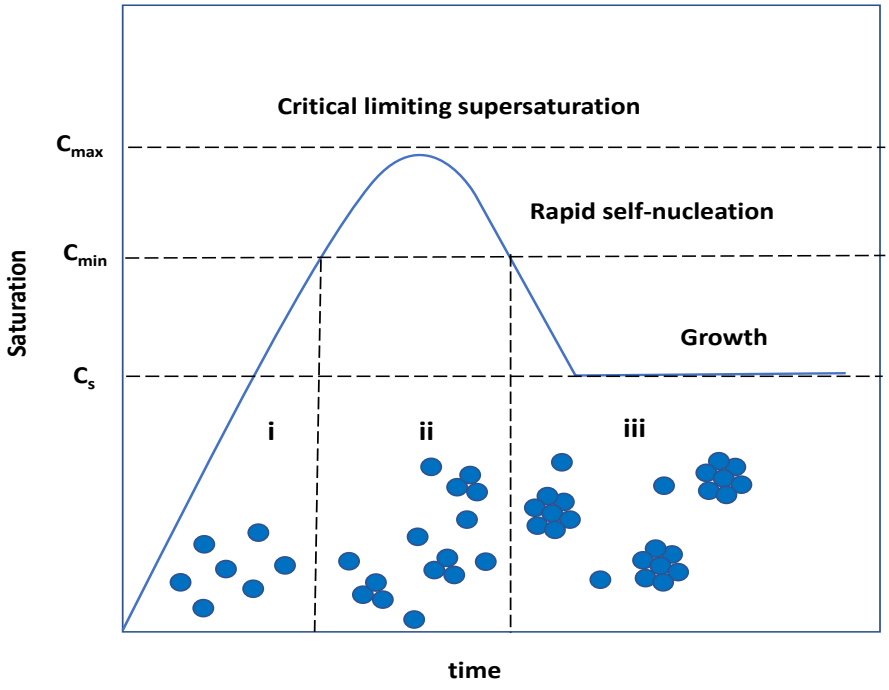

Fig. 2.9: A graphical illustration of LaMer and Dinegar nucleation.

Although the LaMer's model has successfully described the general mechanism for NPs formation, it is still unable to predict the formation of monodispersed NPs. Since during the LaMer's nucleation-growth process, the nucleation is often accompanied by the growth process, whereby stable nuclei continuously grow bigger eventually causing a broad size

distribution. Such nanoparticle growth in colloidal synthesis resulting in broad size distribution can be further explained using the Ostwald's ripening process.

2.6.2.2.2 The Ostwald ripening process

The Ostwald ripening is a growth process whereby smaller crystals in solution redissolve and deposit on the surface of larger particles to favor the growth of such large particles [169]. This process was discovered by Wilhelm Ostwald in the early 1900s and the process has since been named after him [169–171]. The driving force for this process is the solubility difference between the larger and smaller particles where the smaller particles possess higher solubility and interfacial energy, as a result, their Gibbs total energy is greater than that of the larger particles [170]. The continued growth of larger nanoparticles at the expense of small ones leads to a system with a broad range of size distribution as such, ostwald ripening is an undesired process when uniform size distribution of nanoparticles is required. To achieve control of the sizes of nanoparticles and obtain a uniform size distribution, different approaches have been suggested. Such approach includes the digestive ripening process.

2.6.2.2.3 Digestive ripening process

The digestive ripening process involves the growth of small particles at the expense of the larger ones resulting in the narrowing of particle size distribution [172, 173]. This process is a size modification process where highly monodispersed NPs are formed without any size separation step. This method is believed to be pioneered by Klabonde for gold NPs synthesis [172], it has however been adopted for other NP syntheses. Generally, the digestive ripening process involves three major steps. Firstly, the NPs are synthesized using a generic method of chemical synthesis, then, these NPs are capped with the digestive ripening agents. These agents are surface-active ligands such as carboxylic acids and thiols [174]. After the successful capping of the NPs, the capped NPs are recovered by precipitation. Lastly, the recovered capped NPs are refluxed in non-polar organic solvents and then re-dispersed in another portion of the digestive ripening agent. The result of these steps is the formation of extremely monodispersed materials [175].

Inorganic NPs synthesized *via* colloidal route are particularly interesting because such NPs often consist of two layers (the inorganic core coated with an organic layer), the synergistic interaction between the two layers leads to the prospect of property tailoring to fit specific application [176]. Occasionally, the inorganic core determines the magnetic and optoelectronic

properties whereas the organic outer layer influences the physio-chemical properties of the material [176]. The flexibility in property-tailoring coupled with the ease of fabrication has made colloidally synthesized nanoparticles an important group of materials for diverse applications.

2.6.2.3 Factors influencing morphology and size in colloidal synthesis

Various components and processes occurring during the synthesis are responsible for the size and shape tunability offered by colloidal synthesis. Such factors that influence the morphology and size of the NPs are discussed below.

2.6.2.3.1 The role of capping agents or coordinating ligands

Colloidal synthesis is usually performed in organic solvents that coat the colloidal NPs surface hereby forming the capping layer. These ligand molecules vehemently control the nucleation and growth processes of the NP synthesis and to a large extent influence their shapes and sizes [177]. Amphipathic molecules are the optimal capping agents where the polar head is responsible for the metal or NP's surface interaction while the apolar tail impacts the reactivity of the surfactant with the surrounding media [178]. The tendency of the head to coordinate with the NP or metal atom (M) stems from the existence of lone pairs present in the donor atoms (sulphur, phosporus, etc), where these unshared electron pairs successfully coordinate with the M or NP surface [178, 179]. Examples of such coordinating solvents include oleic acid, oleylamine and trioctylphosphine. Different forces such as electrostatic interactions, chemisorption and Lewis - acid-base interactions are responsible for the NP/M – capping agent bonding. The strength of the bond formed between the coordinating ligands and the M also influences the properties of the synthesized material where a strong bond might help improve stability whereas a weaker interaction might lead to an unwanted growth regime in the NPs. Rahimnejad *et al.,* [180] investigated the influence of solvent coordination on the quality of $MAPbI_3$ perovskite. The study showed that when different solvents with varying coordinating abilities are used, some plumbate ion species are formed alongside the intended $MAPbI_3$. The stronger coordinating solvents compete with the iodine atoms to occupy the octahedral sphere of the Pb. This results in the formation of undesired Pb-solvent bonds, which are secondary compounds that affects the overall quality of the perovskite. Similarly, Arian *et al.,* [181] studied the dynamics of solvent engineering for perovskite solar cells. Their study revealed that stronger solvents can dissolve precursor properly leading to lesser trap sites therefore

improving the perovskite's performance. Such strong solvents also form stable adducts with the precursor thus controlling nucleation rate and eventually narrowing the particle size distribution.

2.6.2.3.2 Role of precursor reactivity

Asides from using the right coordinating solvents, choosing the right precursor is also an important parameter to consider when synthesizing NPs. The rate at which the monomers are formed and how the NPs growth progresses is reliant on the type of starting materials. The monomer's reactivity depends on how strongly the surrounding ligands bind to it. The process of monomer formation due to precursor decomposition is given as:

$$P \overset{K_f}{\rightarrow} M \tag{2.24}$$

Where P, K_f and M represent the precursor, formation rate and monomer respectively. Assuming that the monomer formation is a 1st order reaction, the reaction constant will depend on the activation energy and temperature. This can be shown as:

$$\frac{d[M]}{dt} = -\frac{d[P]}{dt} = Aexp\{\frac{-E_A}{RT_V}\}[P] \tag{2.25}$$

Where A represents the prefactor, T_V is the temperature of the reacting solution while E_A represents the activation energy. As a result, monomer formation depends on both the operating temperature and the activation energy. A highly reactive precursor with low activation energy will allow fast monomer formation at low temperature resulting in quick attainment of supersaturation, as a result, nucleation is instantaneously triggered [182]. As a consequence of the fast nucleation and growth regime, more nuclei grow and continuously coalesce with the free monomers thereby quenching further nucleation. This eventually leads to low NP yield with a broad particle size distribution. A moderately reactive precursor however allows for the gradual nucleation process followed by a steady growth regime as a result, the obtained NPs will have a narrower size distribution. Lastly, when a low reacting precursor is used, the formation of monomers is delayed until higher temperature is attained. Therefore, monomer formation progresses very slowly causing delayed formation of nuclei as a result, nuclei of varying sizes are produced. Consequently, the growth regime progresses *via* the Ostwald ripening process resulting in the production of large NPs [182, 183].

2.7 Film deposition

The successful synthesis of the different perovskite solar cell layers is often followed by the deposition of such layers in the device assembly. The film deposition stage is a very crucial step in the PSC fabrication since factors such as film thickness; purity and crystallinity seriously determine the device performance. Some techniques have been developed to deposit different layers of a PSC; such techniques can be broadly grouped into two categories: the vacuum and non-vacuum based deposition techniques. The vacuum-based technique is a very effective way of depositing films and it relies on the material reaching the substrate with minimal or no external interference. The vacuum environment is designed to minimize ambient interferences and impurities to a reasonable minimum. Examples of vacuum-based techniques include evaporation, sputtering and laser deposition techniques. While the vacuum-based methods have been successfully used in PSC fabrication to obtain impressive efficiencies [184–187], this method however requires complex instrument to help control the vacuum environment [188]. The non-vacuum deposition techniques use less energy and inexpensive equipment. Examples of this technique include spray pyrolysis, drop-casting, and spin coating. Although these techniques are not as expensive as the vacuum-based deposition, they are plagued with difficulties during optimization.

2.8 References

[1] C.-H. Chiang, Z.-L. Tseng, C.-G. Wu, *Journal of Materials Chemistry A* 2 (2014) 15897–15903.

[2] N.Y. Yan, W. Yin, *Physics Today* 67 (2014) 13.

[3] H. Tanaka, M. Misono, *Current Opinion in Solid State and Materials Science* 5 (2001) 381–387.

[4] G.A. Samara, Journal of Physics: *Condensed Matter* 15 (2003) R367.

[5] C. Li, K.C.K. Soh, P. Wu, *Journal of Alloys and Compounds* 372 (2004) 40–48.

[6] P. Pizani, E. Leite, F. Pontes, E. Paris, J. Rangel, E. Lee, E. Longo, P. Delega, J.A. Varela, *Applied Physics Letters* 77 (2000) 824–826.

[7] N.-G. Park, *Materials Today* 18 (2015) 65–72.

[8] C. Quarti, E. Mosconi, F. De Angelis, *Physical Chemistry Chemical Physics* 17 (2015) 9394–9409.

[9] C.C. Stoumpos, L. Mao, C.D. Malliakas, M.G. Kanatzidis, *Inorganic Chemistry* 56 (2017) 56–73.

[10] D. Li, G. Wang, H.-C. Cheng, C.-Y. Chen, H. Wu, Y. Liu, Y. Huang, X. Duan, *Nature Communications* 7 (2016) 1–8.

[11] X.-G. Zhao, G.M. Dalpian, Z. Wang, A. Zunger, *Physical Review B* 101 (2020) 155137.

[12] J. Young, J.M. Rondinelli, *The Journal of Physical Chemistry Letters* 7 (2016) 918–922.

[13] C.D. Martin, S. Chaudhuri, C.P. Grey, J.B. Parise, *American Mineralogist* 90 (2005) 1522–1533.

[14] M.W. Lufaso, P.M. Woodward, *Acta Crystallographica Section B: Structural Science* 60 (2004) 10–20.

[15] M. Whangbo, E.E. Gordon, J.L. Bettis Jr, A. Bussmann-Holder, J. Köhler, Zeitschrift *Für Anorganische Und Allgemeine Chemie* 641 (2015) 1043–1052.

[16] G.O. Jones, P.A. Thomas, *Acta Crystallographica B* 58 (2002) 168–178.

[17] N. Setter, L.E. Cross, *Journal of Materials Science* 15 (1980) 2478–2482.

[18] G. Gou, J. Young, X. Liu, J.M. Rondinelli, *Inorganic Chemistry* 56 (2017) 26–32.

[19] T. Qi, I. Grinberg, A.M. Rappe, *Physical Review B* 82 (2010) 134113.

[20] M. Dolgos, U. Adem, X. Wan, Z. Xu, A. J. Bell, T. P. Comyn, T. Stevenson, J. Bennett, J. B. Claridge, M. J. Rosseinsky, *Chemical Science* 3 (2012) 1426–1435.

[21] H.D. Megaw, *Nature* 155 (1945) 484–485.

[22] B. Wul, *Nature* 157 (1946) 808–808.

[23] H.D. Megaw, *Proceedings of the Royal Society of London. Series A. Mathematical and Physical Sciences* 189 (1947) 261–283.

[24] C.H. Ahn, K.M. Rabe, J.-M. Triscone, *Science* 303 (2004) 488–491.

[25] H.A. Jahn, E. Teller, *Proceedings of the Royal Society of London. Series A-Mathematical and Physical Sciences* 161 (1937) 220–235.

[26] U. Öpik, M.H.L. Pryce, *Proceedings of the Royal Society of London. Series A. Mathematical and Physical Sciences 238* (1957) 425–447.

[27] M.C. O'Brien, C. Chancey, *American Journal of Physics* 61 (1993) 688–697.

[28] J.K. Burdett, *Inorganic Chemistry* 20 (1981) 1959–1962.

[29] *Chemistry LibreTexts* https://chem.libretexts.org/ accessed January 16, 2021.

[30] P. Garcia-Fernandez, M. Moreno, J.A. Aramburu, *The Journal of Physical Chemistry C* 118 (2014) 7554–7561.

[31] S. Deng, A. Simon, J. Köhler, *Angewandte Chemie International Edition* 47 (2008) 6703–6706.

[32] S.A. Redfern, *Journal of Physics: Condensed Matter 8* (1996) 8267.

[33] G. Samara, *Ferroelectrics* 2 (1971) 277–289.

[34] B.J. Kennedy, C.J. Howard, B.C. Chakoumakos, *Journal of Physics: Condensed Matter* 11 (1999) 1479–1488.

[35] J.-S. Zhou, J. Alonso, J. Han, M. Fernández-Díaz, J.-G. Cheng, J.B. Goodenough, *Journal of Fluorine Chemistry* 132 (2011) 1117–1121.

[36] M. Towler, R. Dovesi, V.R. Saunders, *Physical Review B* 52 (1995) 10150.

[37] A. Glazer, Acta Crystallographica Section B: *Structural Crystallography and Crystal Chemistry* 28 (1972) 3384–3392.

[38] V.M. Goldschmidt, *Naturwissenschaften* 14 (1926) 477–485.

[39] X. Liu, R. Hong, C. Tian, *Journal of Materials Science: Materials in Electronics* 20 (2009) 323.

[40] Z. Li, M. Yang, J.-S. Park, S.-H. Wei, J.J. Berry, K. Zhu, *Chemistry of Materials* 28 (2016) 284–292.

[41] F. Dong, D. Chen, Y. Chen, Q. Zhao, Z. Shao, *Journal of Materials Chemistry* 22 (2012) 15071–15079.

[42] K. Leinenweber, W. Utsumi, Y. Tsuchida, T. Yagi, K. Kurita, *Physics and Chemistry of Minerals* 18 (1991) 244–250.

[43] X. Zhang, X. Bai, H. Wu, X. Zhang, C. Sun, Y. Zhang, W. Zhang, W. Zheng, W.W. Yu, A.L. Rogach, *Angewandte Chemie International Edition* 57 (2018) 3337–3342.

[44] M. Becker, T. Klüner, M. Wark, *Dalton Transactions* 46 (2017) 3500–3509.

[45] C. Li, X. Lu, W. Ding, L. Feng, Y. Gao, Z. Guo, *Acta Crystallographica Section B* 64 (2008) 702–707.

[46] D. Ji, S. Feng, L. Wang, S. Wang, M. Na, H. Zhang, C. Zhang, X. Li, *Vacuum* 164 (2019) 186–193.

[47] D. Serrate, J. De Teresa, M. Ibarra, *Journal of Physics: Condensed Matter 19* (2006) 023201.

[48] F. Igbari, Z. Wang, L. Liao, *Advanced Energy Materials* 9 (2019) 1803150.

[49] E. Meyer, D. Mutukwa, N. Zingwe, R. Taziwa, *Metals* 8 (2018) 667.

[50] S. Li, B. AlOtaibi, W. Huang, Z. Mi, N. Serpone, R. Nechache, F. Rosei, *Small* 11 (2015) 4018–4026.

[51] G. Volonakis, A.A. Haghighirad, R.L. Milot, W.H. Sio, M.R. Filip, B. Wenger, M.B. Johnston, L.M. Herz, H.J. Snaith, F. Giustino, *The Journal of Physical Chemistry Letters* 8 (2017) 772–778.

[52] Q. Hu, Z. Deng, M. Hu, A. Zhao, Y. Zhang, Z. Tan, G. Niu, H. Wu, J. Tang, *Science China Chemistry* 61 (2018) 1581–1586.

[53] W. Gao, C. Ran, J. Xi, B. Jiao, W. Zhang, M. Wu, X. Hou, Z. Wu, *ChemPhysChem* 19 (2018) 1696–1700.

[54] F. Wei, Z. Deng, S. Sun, F. Zhang, D.M. Evans, G. Kieslich, S. Tominaka, M.A. Carpenter, J. Zhang, P.D. Bristowe, *Chemistry of Materials* 29 (2017) 1089–1094.

[55] J. Luo, S. Li, H. Wu, Y. Zhou, Y. Li, J. Liu, J. Li, K. Li, F. Yi, G. Niu, *ACS Photonics* 5 (2018) 398–405.

[56] W. Meng, X. Wang, Z. Xiao, J. Wang, D.B. Mitzi, Y. Yan, *The Journal of Physical Chemistry Letters* 8 (2017) 2999–3007.

[57] S. Uma, A.R. Raju, J. Gopalakrishnan, *Journal of Materials Chemistry* 3 (1993) 709–713.

[58] S. Ahmad, P. Fu, S. Yu, Q. Yang, X. Liu, X. Wang, X. Wang, X. Guo, C. Li, *Joule* 3 (2019) 794–806.

[59] S. Zhao, C. Lan, H. Li, C. Zhang, T. Ma, *The Journal of Physical Chemistry C* 124 (2019) 1788–1793.

[60] B. Beznosikov, K. Aleksandrov, *Crystallography Reports* 45 (2000) 792–798.

[61] H. Tsai, W. Nie, J.-C. Blancon, C.C. Stoumpos, R. Asadpour, B. Harutyunyan, A.J. Neukirch, R. Verduzco, J.J. Crochet, S. Tretiak, *Nature* 536 (2016) 312–316.

[62] D.H. Cao, C.C. Stoumpos, O.K. Farha, J.T. Hupp, M.G. Kanatzidis, *Journal of the American Chemical Society* 137 (2015) 7843–7850.

[63] B. Frit, J. Mercurio, *Journal of Alloys and Compounds* 188 (1992) 27–35.

[64] T. Rentschler, M. Karus, A. Wellm, A. Reller, *Solid State Ionics* 90 (1996) 49–55.

[65] G. Nalini, G. Subbanna, T.G. Row, *Materials Chemistry and Physics* 82 (2003) 663–671.

[66] M. Nanao, M. Hirose, T. Tsukada, *Japanese Journal of Applied Physics* 40 (2001) 5727.

[67] Z. Zhou, X. Dong, H. Chen, H. Yan, *Journal of the American Ceramic Society* 89 (2006) 1756–1760.

[68] L. Spadaro, F. Arena, A. Palella, in: *Methanol, Elsevier*, (2018), 429–472.

[69] C.M. Maxfield, in: C.M. Maxfield (Ed.), *Bebop to the Boolean Boogie (Third Edition), Newnes, Boston*, (2009), 17–31.

[70] F. Hao, C.C. Stoumpos, R.P. Chang, M.G. Kanatzidis, *Journal of the American Chemical Society* 136 (2014) 8094–8099.

[71] N.K. Noel, S.D. Stranks, A. Abate, C. Wehrenfennig, S. Guarnera, A.-A. Haghighirad, A. Sadhanala, G.E. Eperon, S.K. Pathak, M.B. Johnston, *Energy & Environmental Science* 7 (2014) 3061–3068.

[72] Z. Yang, A. Rajagopal, C. Chueh, S.B. Jo, B. Liu, T. Zhao, A.K. Jen, *Advanced Materials* 28 (2016) 8990–8997.

[73] S.D. Stranks, G.E. Eperon, G. Grancini, C. Menelaou, M.J. Alcocer, T. Leijtens, L.M. Herz, A. Petrozza, H.J. Snaith, *Science* 342 (2013) 341–344.

[74] Y. Zhao, A.M. Nardes, K. Zhu, *The Journal of Physical Chemistry Letters* 5 (2014) 490–494.

[75] X. Ziang, L. Shifeng, Q. Laixiang, P. Shuping, W. Wei, Y. Yu, Y. Li, C. Zhijian, W. Shufeng, D. Honglin, Y. Minghui, G.G. Qin, *Optical Materials Express* 5 (2015) 29–43.

[76] A. Kojima, K. Teshima, T. Miyasaka, Y. Shirai, *The Electrochemical Society*, 2006, 397–397.

[77] N. Ashurov, B.L. Oksengendler, S. Maksimov, S. Rashiodva, A.R. Ishteev, D.S. Saranin, I.N. Burmistrov, D.V. Kuznetsov, A.A. Zakhisov, *Modern Electronic Materials* 3 (2017) 1–25.

[78] M.A. Green, A. Ho-Baillie, H.J. Snaith, *Nature Photonics* 8 (2014) 506.

[79] J.-H. Im, C.-R. Lee, J.-W. Lee, S.-W. Park, N.-G. Park, *Nanoscale* 3 (2011) 4088–4093.

[80] J. Qian, B. Xu, W. Tian, *Organic Electronics* 37 (2016) 61–73.

[81] L. Ji, H.-Y. Hsu, A.J. Bard, T.Y. Edward, *IEEE Conference on Photovoltaics Specialists*, (2016), 0781–0784.

[82] H.-S. Kim, C.-R. Lee, J.-H. Im, K.-B. Lee, T. Moehl, A. Marchioro, S.-J. Moon, R. Humphry-Baker, J.-H. Yum, J.E. Moser, *Scientific Reports* 2 (2012) 591.

[83] M.M. Lee, J. Teuscher, T. Miyasaka, T.N. Murakami, H.J. Snaith, *Science* 338 (2012) 643–647.

[84] D. Bryant, N. Aristidou, S. Pont, I. Sanchez-Molina, T. Chotchunangatchaval, S. Wheeler, J.R. Durrant, S.A. Haque, *Energy and Environmental Science* 9 (2016) 1655–1660.

[85] Y. Han, S. Meyer, Y. Dkhissi, K. Weber, J.M. Pringle, U. Bach, L. Spiccia, Y.-B. Cheng, *Journal of Materials Chemistry A* 3 (2015) 8139–8147.

[86] N. Aristidou, C. Eames, I. Sanchez-Molina, X. Bu, J. Kosco, M.S. Islam, S.A. Haque, *Nature Communications* 8 (2017) 1–10.

[87] G. Abdelmageed, L. Jewell, K. Hellier, L. Seymour, B. Luo, F. Bridges, J.Z. Zhang, S. Carter, *Applied Physics Letters*. 109 (2016) 233905.

[88] J. Yang, T.L. Kelly, *Inorganic Chemistry* 56 (2017) 92–101.

[89] J.A. Christians, P.A. Miranda Herrera, P.V. Kamat, *Journal of the American Chemical Society* 137 (2015) 1530–1538.

[90] F. Hao, C.C. Stoumpos, Z. Liu, R.P. Chang, M.G. Kanatzidis, *Journal of the American Chemical Society* 136 (2014) 16411–16419.

[91] A.M. Leguy, Y. Hu, M. Campoy-Quiles, M.I. Alonso, O.J. Weber, P. Azarhoosh, M. Van Schilfgaarde, M.T. Weller, T. Bein, J. Nelson, *Chemistry of Materials* 27 (2015) 3397–3407.

[92] A. Suzuki, H. Okada, T. Oku, *AIP Publishing LLC*, (2016), 2002-2009.

[93] F. Ansari, M. Salavati-Niasari, P. Nazari, N. Mir, V. Ahmadi, B. Abdollahi Nejand, *ACS Applied Energy Materials*. 1 (2018) 6018–6026.

[94] S. Lee, D.-W. Kang, *ACS Applied Materials Interfaces* 9 (2017) 22432–22439.

[95] M. Loghman-Adham, *Environmental Health Perspectives* 105 (1997) 928–939.

[96] P. Mitra, S. Sharma, P. Purohit, P. Sharma, *Critical Reviews in Clinical Laboratory Sciences* 54 (2017) 506–528.

[97] H. Needleman, *Annual Review of Medicine* 55 (2004) 209–222.

[98] A.H. Slavney, R.W. Smaha, I.C. Smith, A. Jaffe, D. Umeyama, H.I. Karunadasa, *Inorganic Chemistry* 56 (2017) 46–55.

[99] J. Markovac, G.W. Goldstein, *Nature* 334 (1988) 71–73.

[100] Y. Zhou, Y. Zhao, *Energy & Environmental Science* 12 (2019) 1495–1511.

[101] S.C. Yue-Yu Zhang, S.C. Yue-Yu Zhang, *Chinese Physics Letters* 35 (2018) 36104–036104.

[102] M. Saliba, T. Matsui, J.-Y. Seo, K. Domanski, J.-P. Correa-Baena, M.K. Nazeeruddin, S.M. Zakeeruddin, W. Tress, A. Abate, A. Hagfeldt, M. Grätzel, *Energy and Environmental Science* 9 (2016) 1989–1997.

[103] N. Aristidou, I. Sanchez-Molina, T. Chotchuangchutchaval, M. Brown, L. Martinez, T. Rath, S.A. Haque, *Angewandte Chemie* 127 (2015) 8326–8330.

[104] W. Ke, C.C. Stoumpos, M.G. Kanatzidis, *Advanced Materials* 31 (2019) 1803230.

[105] S.F. Hoefler, G. Trimmel, T. Rath, *Monatshefte Chemie-Chemical* 148 (2017) 795–826.

[106] G.P. Nagabhushana, R. Shivaramaiah, A. Navrotsky, *Proceedings of the National Academy of Sciences* 113 (2016) 7717–7721.

[107] A. Wang, Y. Guo, F. Muhammad, Z. Deng, *Chemistry of Materials* 29 (2017) 6493–6501.

[108] D.E. Scaife, P.F. Weller, W.G. Fisher, *Journal of Solid State Chemistry* 9 (1974) 308–314.

[109] M. Mori, H. Saito, *Journal of Physics C: Solid State Physics* 19 (1986) 2391.

[110] L. Huang, W.R. Lambrecht, *Physical Review B* 88 (2013) 165203.

[111] B. Li, R. Long, Y. Xia, Q. Mi, *Angewandte Chemie International Edition 57* (2018) 13154–13158.

[112] M. Leng, Z. Chen, Y. Yang, Z. Li, K. Zeng, K. Li, G. Niu, Y. He, Q. Zhou, J. Tang, *Angewandte Chemie International Edition* 55 (2016) 15012–15016.

[113] Q. Zhang, H. Ting, S. Wei, D. Huang, C. Wu, W. Sun, B. Qu, S. Wang, Z. Chen, L. Xiao, *Materials Today Energy* 8 (2018) 157–165.

[114] K.H. Whitmire, *Encyclopedia of Inorganic and Bioinorganic Chemistry* (2011) 1–32.

[115] K. Dave, M.H. Fang, Z. Bao, H.T. Fu, R.S. Liu, Chemistry – *An Asian Journal* 15 (2020) 242–252.

[116] Q. Zhang, F. Hao, J. Li, Y. Zhou, Y. Wei, H. Lin, *Science and Technology of Advanced Materials* 19 (2018) 425–442.

[117] K.K. Bass, L. Estergreen, C.N. Savory, J. Buckeridge, D.O. Scanlon, P.I. Djurovich, S.E. Bradforth, M.E. Thompson, B.C. Melot, *Inorganic Chemistry* 56 (2017) 42–45.

[118] R. Chen, D. Hou, C. Lu, J. Zhang, P. Liu, H. Tian, Z. Zeng, Q. Xiong, Z. Hu, Y. Zhu, L. Han, *Sustainable Energy & Fuels* 2 (2018) 1093–1100.

[119] M.S. Gorji, K.Y. Cheong, *Critical Reviews in Solid State and Materials Sciences* 40 (2015) 197–222.

[120] F. Kröger, G. Diemer, H. Klasens, *Physical Review* 103 (1956) 279.

[121] B. Sharma, Metal-Semiconductor Schottky Barrier Junctions and Their Applications, *Springer Science & Business Media*, 2013.

[122] L.M. Porter, R.F. Davis, *Materials Science and Engineering: B* 34 (1995) 83–105.

[123] M. Tyagi, in: Metal-Semiconductor Schottky Barrier Junctions and Their Applications, *Springer*, (1984), 1–60.

[124] P.L. Hanselaer, W.H. Laflère, R.L. Van Meirhaeghe, F. Cardon, *Journal of Applied Physics* 56 (1984) 2309–2314.

[125] M. Ožold, *Physica Status Solidi* (a) 132 (1992) 517–525.

[126] K. Potje-Kamloth, in: H.S. Nalwa (Ed.), *Handbook of Surfaces and Interfaces of Materials, Academic Press, Burlington*, (2001), 445–494.

[127] Y. Wang, Y. Xia, *Nano Letters* 4 (2004) 2047–2050.

[128] V. Pareek, A. Bhargava, R. Gupta, N. Jain, J. Panwar, *Advanced Science, Engineering and Medicine* 9 (2017) 527–544.

[129] A.M. Ealias, M. Saravanakumar, *Materials Science and Engineering* (2017).

[130] *Materials Today* 4 (2001) 24–29.

[131] D.J. Ashworth, A. Cooper, M. Trueman, R.W.M. Al-Saedi, L.D. Smith, A.J.H.M. Meijer, J.A. Foster, Chemistry – *A European Journal 24* (2018) 17986–17996.

[132] K. Muthoosamy, S. Manickam, *Ultrasonics Sonochemistry* 39 (2017) 478–493.

[133] K.S. Suslick, G.J. Price, *Annual Review of Materials Science* 29 (1999) 295–326.

[134] V. Štengl, J. Henych, M. Slušná, P. Ecorchard, *Nanoscale Research Letters* 9 (2014) 167.

[135] C. Cai, N. Sang, Z. Shen, X. Zhao, *Journal of Experimental Nanoscience* 12 (2017) 247–262.

[136] X.-D. Wang, N.-H. Miao, J.-F. Liao, W.-Q. Li, Y. Xie, J. Chen, Z.-M. Sun, H.-Y. Chen, D.-B. Kuang, *Nanoscale* 11 (2019) 5180–5187.

[137] Y. Hu, L. Guo, *ChemCatChem* 7 (2015) 584–587.

[138] G. Tallents, E. Wagenaars, G. Pert, *Nature Photonics* 4 (2010) 809.

[139] B.P. Wong, A. Mittal, G.W. Starr, F. Zach, V. Moroz, A. Kahng, Nano-CMOS Design for Manufacturability: Robust Circuit and Physical Design for Sub-65nm Technology Nodes, *John Wiley & Sons*, 2008.

[140] H.I. Smith, D. Spears, S. Bernacki, *Journal of Vacuum Science and Technology* 10 (1973) 913–917.

[141] F. Watt, A. Bettiol, J. Van Kan, E. Teo, M. Breese, *International Journal of Nanoscience* 4 (2005) 269–286.

[142] R.P. Seisyan, *Technical Physics*. 50 (2005) 535–545.

[143] C. Mack, Fundamental Principles of Optical Lithography: The Science of Microfabrication, *John Wiley & Sons*, 2008.

[144] M. Madou, C. Wang, in: B. Bhushan (Ed.), *Encyclopedia of Nanotechnology, Springer* Netherlands, Dordrecht, (2012), 2051–2060.

[145] J. Wu, J. Chen, Y. Zhang, Z. Xu, L. Zhao, T. Liu, D. Luo, W. Yang, K. Chen, Q. Hu, Nano Letters 17 (2017) 3563–3569.

[146] Z. Duan, Y. Wang, G. Li, S. Wang, N. Yi, S. Liu, S. Xiao, Q. Song, *Laser & Photonics Reviews* 12 (2018) 1700234.

[147] J.D. Mackenzie, E.P. Bescher, *Accounts of Chemical Research* 40 (2007) 810–818.

[148] G.V. Aguilar, Sol-Gel Method - Design and Synthesis of New Materials with Interesting Physical, Chemical and Biological Properties (2018).

[149] I. Lacatusu, N. Badea, R. Nita, A. Murariu, F. Miculescu, I. Iosub, A. Meghea, *Optical Materials* 32 (2010) 711–718.

[150] S. Bashir, J. Liu, Advanced Nanomaterials and Their Applications in Renewable Energy (2015) 51.

[151] S. Mann, S.L. Burkett, S.A. Davis, C.E. Fowler, N.H. Mendelson, S.D. Sims, D. Walsh, N.T. Whilton, *Chemistry of Materials* 9 (1997) 2300–2310.

[152] A.V. Rane, K. Kanny, V. Abitha, S. Thomas, in: Synthesis of Inorganic Nanomaterials, *Elsevier*, (2018), 121–139.

[153] P.V. Kamat, M. Flumiani, A. Dawson, *Colloids and Surfaces A*: Physicochemical and Engineering Aspects 202 (2002) 269–279.

[154] Y. Xia, Y. Xiong, B. Lim, S.E. Skrabalak, *Angewandte Chemie International Edition* 48 (2009) 60–103.

[155] M. Valden, X. Lai, D.W. Goodman, *Science* 281 (1998) 1647–1650.

[156] A. Zecchina, E. Groppo, S. Bordiga, *Chemistry–A European Journal* 13 (2007) 2440–2460.

[157] R. Becker, W. Döring, *Annalen Der Physik* 416 (1935) 719–752.

[158] D.T. Wu, in: H. Ehrenreich, F. Spaepen, *Solid State Physics*, Academic Press, (1996), 37–187.

[159] T.H. Zhang, X.Y. Liu, *Handbook of Crystal Growth, Elsevier*, (2015), 561–594.

[160] X.Y. Liu, J. *The Journal of Chemical Physics.* 112 (2000) 9949–9955.

[161] J.E. McDonald, *American Journal of Physics* 30 (1962) 870–877.

[162] A. Dillmann, G. Meier, *Chemical Physics Letters* 160 (1989) 71–74.

[163] P.R. ten Wolde, D. Frenkel, *Physical Chemistry Chemical Physics* 1 (1999) 2191–2196.

[164] W.D. Callister, D.G. Rethwisch, *Materials Science and Engineering, John wiley & sons NY*, 2011.

[165] V.K.L. Mer, *Industrial & Engineering Chemistry* 44 (1952) 1270–1277.

[166] V.K. LaMer, R.H. Dinegar, *Journal of the American Chemical Society* 72 (1950) 4847–4854.

[167] D.B.K. Chu, J.S. Owen, B. Peters, *The Journal of Physical Chemistry A* 121 (2017) 7511–7517.

[168] N.T.K. Thanh, N. Maclean, S. Mahiddine, *Chemical Reviews* 114 (2014) 7610–7630.

[169] D.D. Eberl, J. Srodon, *American Mineralogist* 73 (1988) 1335–1345.

[170] C.C. Yec, H.C. Zeng, *Journal of Materials Chemistry A* 2 (2014) 4843–4851.

[171] W. Ostwald, *Zeitschrift Für Physikalische Chemie* 34 (1900) 495–503.

[172] X. Lin, C. Sorensen, K. Klabunde, *Journal of Nanoparticle Research* 2 (2000) 157–164.

[173] X. Lin, H. Jaeger, C. Sorensen, K. Klabunde, *The Journal of Physical Chemistry B* 105 (2001) 3353–3357.

[174] B. Prasad, S.I. Stoeva, C.M. Sorensen, K.J. Klabunde, *Chemistry of Materials* 15 (2003) 935–942.

[175] J.R. Shimpi, D.S. Sidhaye, B.L. Prasad, *Langmuir* 33 (2017) 9491–9507.

[176] Y. Yin, A.P. Alivisatos, *Nature* 437 (2005) 664–670.

[177] J. Pérez-Juste, I. Pastoriza-Santos, L.M. Liz-Marzán, P. Mulvaney, *Coordination Chemistry Reviews* 249 (2005) 1870–1901.

[178] R.A. Sperling, W.J. Parak, Philosophical Transactions of the Royal Society *A: Mathematical, Physical and Engineering Sciences* 368 (2010) 1333–1383.

[179] C.M. Phan, H.M. Nguyen, *The Journal of Physical Chemistry A* 121 (2017) 3213–3219.

[180] S. Rahimnejad, A. Kovalenko, S.M. Forés, C. Aranda, A. Guerrero, *ChemPhysChem* 17 (2016) 2795–2798.

[181] Z. Arain, C. Liu, Y. Yang, M. Mateen, Y. Ren, Y. Ding, X. Liu, Z. Ali, M. Kumar, S. Dai, *Science China Materials* 62 (2019) 161–172.

[182] J. van Embden, A.S. Chesman, J.J. Jasieniak, *Chemistry of Materials* 27 (2015) 2246–2285.

[183] S.G. Kwon, T. Hyeon, *Small* 7 (2011) 2685–2702.

[184] D. Yang, Z. Yang, W. Qin, Y. Zhang, S. (Frank) Liu, C. Li, *Journal of Materials Chemistry A* 3 (2015) 9401–9405.

[185] C.-W. Chen, H.-W. Kang, S.-Y. Hsiao, P.-F. Yang, K.-M. Chiang, H.-W. Lin, *Advanced Materials* 26 (2014) 6647–6652.

[186] A. Babaei, W. Soltanpoor, M.A. Tesa-Serrate, S. Yerci, M. Sessolo, H.J. Bolink, *Energy Technology* 8 (2020) 1900784.

[187] C.-Y. Chen, W.-H. Lee, S.-Y. Hsiao, W.-L. Tsai, L. Yang, H.-L. Lin, H.-J. Chou, H.-W. Lin, *Journal of Materials Chemistry A* 7 (2019) 3612–3617.

[188] A. Boudrioua, M. Chakaroun, A. Fischer, in: A. Boudrioua, M. Chakaroun, A. Fischer, *An Introduction to Organic Lasers, Elsevier*, (2017), 49–93.

CHAPTER 3

The effect of temperature and time on the synthesis of $CsSnBr_3$ perovskite nanocrystals

3.1 Introduction

Perovskites are a class of semiconductor materials with the general formula ABX_3 as previously discussed in Chapter 2 section 2.1. Due to Pb toxicity, there is growing interest in the search for Pb substitutes in the perovskites. The formula of perovskites potentially allows the exploitation of numerous divalent cations in the periodic table, the most suitable substitute for Pb however is tin (Sn) [1]. Tin is a divalent element with an atomic number of 50 and it belongs to the same group as Pb therefore, similar chemical properties can be expected. Asides from the aforementioned similarity, Sn and Pb also have roughly the same ionic radii (Sn = 115 picometer (pm), Pb = 117 pm) [1]. As a result, Sn is perfectly sized to fit into the B octahedral site in the perovskite's crystal structure. Interestingly, Sn is generally considered less toxic as compared to Pb largely due to the poor absorption of Sn by organisms except for the organotin compounds which are very toxic [2]. The $CsSnBr_3$ is a direct bandgap material with the bandgap in the range of 1.75 to 1.9 eV [3, 4]. Due to their tunable bandgap, low recombination rates and high rate of carrier diffusion, this material is very useful for photovoltaic application [4]. The synthesis of $CsSnBr_3$ perovskite nanocrystals (NCs) can be done using colloidal route which is an efficient method of synthesizing monodispersed NCs. The hot-injection method is a form of colloidal synthesis employed for highly monodisperse NCs. This method was pioneered by Alivisatos and Bawendi to synthesize cadmium chalcogenides [5, 6]. This synthetic method entails the generation of homogenous nuclei through the expeditious injection of the precursor into solvents at high temperature [7]. Therefore, the burst nucleation achieved lead to the attainment of narrow size distribution of the NCs. In the reaction vessel, surfactant molecules and ligands are also present and their role is to prevent the agglomeration of the NCs by selectively binding/capping to the nanoparticles NPs surface [7]. Typical ligands used include alkylphosphines (trioctylphosphine), long-chain amines (oleylamnine) and long-chain carboxylic acids (oleic acid). Upon precursor injection, the reaction temperature is reduced to differentiate the nucleation and the nanocrystal growth stages. Since the size and shape control of the NCs are highly dependent on the kinetics of the nucleation and growth regime, it is therefore important to control the reaction parameters such as the reaction temperature and time among others. Herein, the hot-injection synthesis of

$CsSnBr_3$ NCs is discussed followed by studying the effect of reaction temperature and time while also comprehensively characterizing the synthesized perovskite.

3.2 Experimental procedures

3.2.1 Chemicals

Tin(II) bromide ($SnBr_2$ 99%), Cesium carbonate (Cs_2CO_3 99%), Oleylamine (OLA 70%), Oleic acid (OA, 90%), tetrabutylammoniumhexafluorophosphate ($TBAPF_6$, 99%), dichloromethane (DCM anhydrous > 90%), chloroform-d ($CdCl_3$ 99.8 atom% D) and toluene 95% were purchased from Sigma-Aldrich. All chemicals were used without any further purification.

3.2.2 Synthesis of $CsSnBr_3$ nanomaterials

Under nitrogen flow, 0.1 g cesium carbonate (Cs_2CO_3) was placed in 7 mL of oleic acid (OA) in a three-necked round bottom flask and heated to 140 °C for 1 hour under vigorous stirring for the Cs_2CO_3 to completely dissolve and form Cesium oleate (CsOA). In a separate 25 mL three-necked flask, 0.3 g $SnBr_2$ was placed in equal volume (7.5 ml) of OA and OLA and temperature was varied between 170 °C - 230 °C for 1 h for the $SnBr_2$ to completely dissolve. Thereafter, 1 mL of the CsOA was swiftly injected into the $SnBr_2$ three-necked flask with a syringe where after 1 min; the flask was cooled to room temperature with a cold-water bath. The resultant powders were washed subsequently in toluene. Using the same method, the temperature and time were varied.

3.2.3 Characterization techniques

Powder X-ray diffraction (PXRD) analysis was conducted using a Bruker D2 phaser (D2-205530) diffractometer using a Cu Kα radiation source (λ 1.541060 Å) at 30 kV and 10 mA. The measurements were taken over the range of 5 to 90° at room temperature. The sample morphologies were determined using FEI Technai T12 Transmission Electron Microscope (TEM), operated at 120 kV with a beam spot of 3 in the TEM mode. The nanocrystals (NCs) were dispersed in toluene and drop-casted onto a lacey-carbon copper grid and dried at room temperature before analysis. The absorption measurements were done by dispersing the NCs in toluene and then placed into a quartz cuvette (1 cm path length) thereafter the measurements were carried out on a Specord 210 plus AnalytikJena UV-vis spectrophotometer. The

photoluminescence (PL) measurements on powdered samples were done using HORIBA QM8000 spectrofluorometer equipped with a PPD-850 detector. X-ray photoelectron spectroscopy (XPS) analysis was conducted using a Physical Electronics PHI 5700 spectrometer using non-monochromatic Mg Kα x-rays (300 W, 15 kV, and 1253.6 eV) as the excitation source. The spectrometer energy scale was calibrated using Cu $2p_{3/2}$, Ag $3d_{5/2}$, and Au $4f_{7/2}$ photoelectron lines at 932.7, 368.3, and 84.0 eV, respectively. The samples for XPS analysis were loaded onto the sample holder and left overnight at a high vacuum in the preparation chamber prior to being transferred to the analysis chamber. The Fourier Transform Infrared (FTIR) spectra were measured on a Bruker Tensor 27 FTIR spectrophotometer while the nuclear magnetic resonance (NMR) data were obtained with a 500 MHz Bruker AVANCE III; the samples were characterized using $CdCl_3$ as a solvent at room temperature. Raman spectroscopy experiments were performed on a J-Y T64000 micro-Raman spectrometer (Horiba Jobin-Yvon, Ltd., Stanmore, UK) equipped with a liquid nitrogen-cooled charge-coupled device detector. All samples were measured after excitation with a laser wavelength of 514.5 nm. A Biologic SP-300 potentiostat with a 3-electrode cell was used for the CV measurement. Glassy carbon electrode, Ag wire and a platinum rod were used as the working, reference, and counter electrode respectively. A 100 mM $TBAPF_6$ solution prepared in DCM was used as the electrolyte solution; the reference electrode was polished severally with alumina paste and washed with deionized water. The thermal stability of the samples was monitored with a PerkinElmer 6000 thermogravimetric analyzer.

3.3 Results and discussions

3.3.1 Effect of temperature on $CsSnBr_3$ nanocrystals

The study was done using 170 °C, 200 °C and 230 °C as variables for temperature of synthesis. The crystal structure and phase of $CsSnBr_3$ was determined with XRD. The XRD patterns in Fig. 3.1 show the reference peaks and the XRD patterns obtained at different temperatures. At 170 °C reaction temperature, the material formed did not match the $CsSnBr_3$ perovskite and this could be due to presence of unreacted precursors or the formation of other materials. Hence, at low temperatures (≤ 170 °C), the complete formation of $CsSnBr_3$ is unfavored. However, at a higher temperature (200 °C), the cubic $CsSnBr_3$ perovskite with space group *Pm-3m* (221), card number PDF 01-070-1645 and lattice parameter a = 5.79500 Å was formed. At further elevated temperature (230 °C) the $CsSnBr_3$ perovskite was still formed with no deviations in the peak positions observed. Both the $CsSnBr_3$ perovskite synthesized at 200 °C

and 230 °C show high crystallinity as indicated from the narrow and sharp peaks in Fig. 3.1. Prior to this study, the colloidal synthesis of $CsSnBr_3$ has mostly relied on the use of the expensive trioctylphosphine (TOP) as the reducing and co-ordinating solvent while some literature employs additional precursors such as $MgBr_2$ which is reacted with stannous 2-ethylhexanoate to synthesize the $CsSnBr_3$ perovskite [8, 9]. The sole use of OLA and OA mixture has been reported to form CsBr precipitate instead of the desired $CsSnBr_3$ [8]. However, we found out that using the appropriate synthesis temperature coupled with the suitable OLA and OA volume ratio, the $CsSnBr_3$ perovskite can be synthesized without the need for TOP or any additional precursor, this translates to a cost-effective method of lead-free perovskite synthesis.

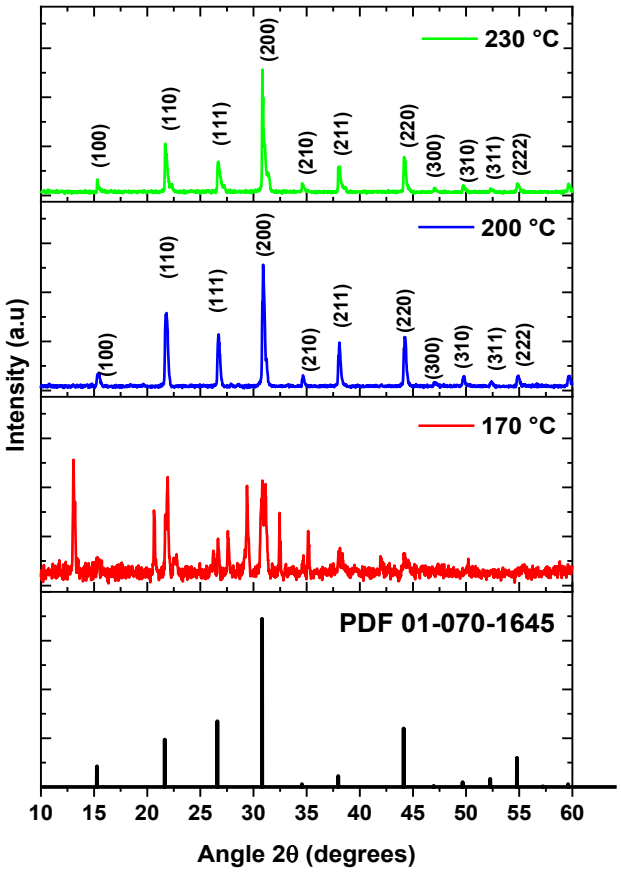

Fig. 3.1: XRD patterns of $CsSnBr_3$ nanocrystals synthesized at different temperatures.

The size and shape of the NCs synthesized at different temperatures were investigated *via* TEM. From the TEM image in Fig. 3.2, the NCs synthesized at 170 °C showed a hollow hexagonal morphology which is uniformly distributed and monodispersed, these NCs have an

average particle size distribution of 20 nm as indicated from their histogram. At 200 °C where the ideal $CsSnBr_3$ perovskite was formed, nanocrystals with an average particle size of 3 nm were formed while at 230 °C, similar nanocrystals with 3 nm particle size were obtained.

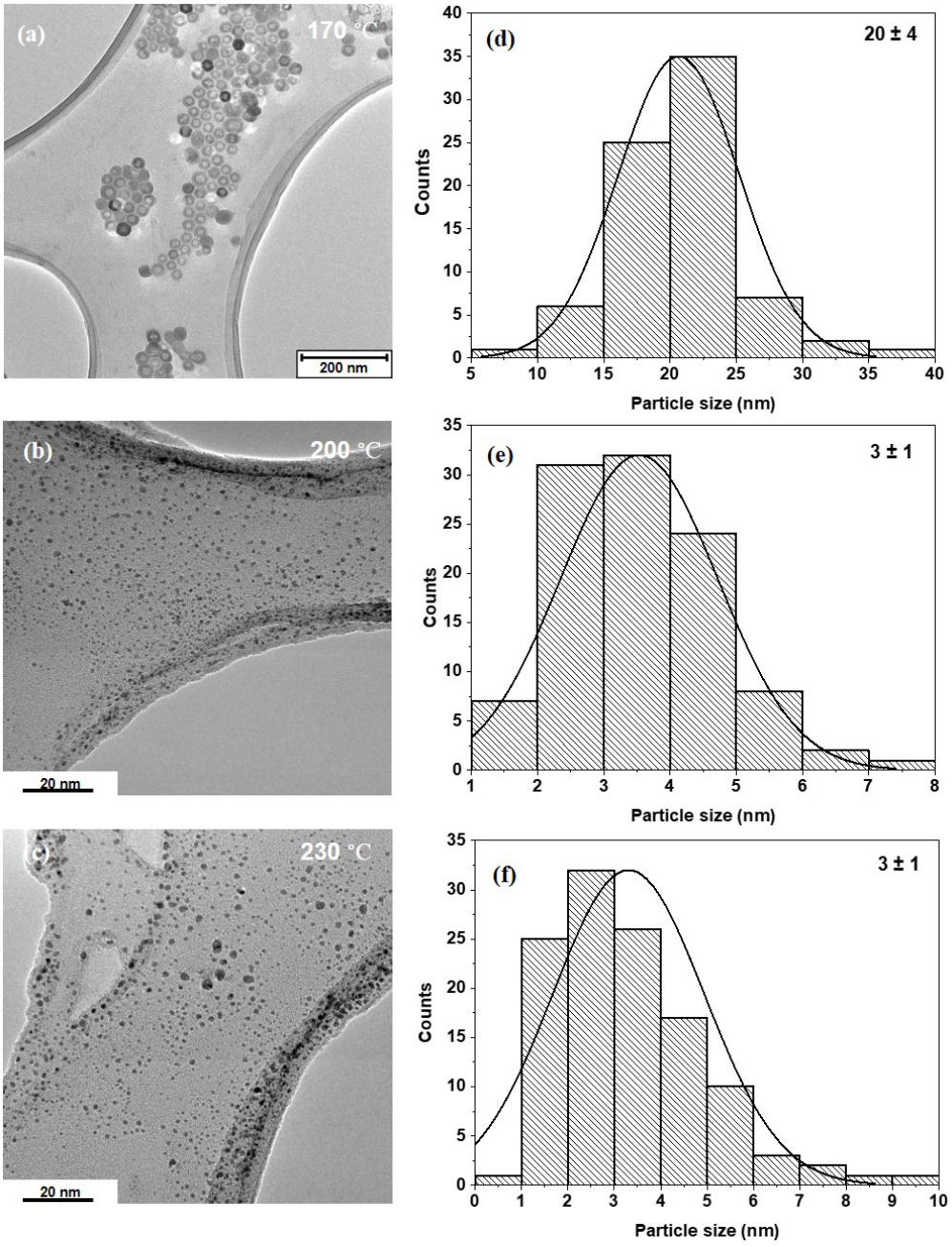

Fig. 3.2: (a-c) TEM images and (d-f) size distribution of $CsSnBr_3$ NCs synthesized at different temperatures.

Optical properties are important for optoelectronic applications of semiconductors and they are strongly dependent on size and morphology of NCs. The investigation of the optical properties of $CsSnBr_3$ nanocrystals were determined using UV-vis and PL spectroscopy and the results are shown in Fig. 3.3. From the Tauc plots, as the reaction temperature is increased from 170

°C to 200 °C, the absorption peaks became more defined with a corresponding red-shifting in the bandgap of the $CsSnBr_3$ NCs from 2.52 eV to 1.75 eV and finally, at 230 °C there is a further slight red-shift in the bandgap of the perovskite NCs to 1.72 eV. The steady decrease in the bandgap energy of the NCs with a corresponding decrease in NC size deviates from the ideal electronic confinement effect. However, this deviation is because entirely different materials are synthesized at 170 °C and 200 °C as seen from the XRD pattern in Fig. 3.1, hence a genuine trend cannot be established. Li *et al.,* [3] synthesized $CsSnBr_3$ with a furnace at 450 °C for 4 h and obtained a bandgap of 1.9 eV which is close to the 1.85 eV synthesized *via* colloidal synthesis reported here. Both the absorption and emission spectroscopy data can be used to determine the stokes shift of the nanocrystals where a small stokes shift is ideal in perovskites so as to prevent energy loss. The emission spectra of the NCs are shown in Fig. 3.3(b). Similar to the absorption spectra of $CsSnBr_3$ at varying temperatures, there was a steady bathochromic shift in the emission wavelength of $CsSnBr_3$ with an increase in temperature of the NCs. At 170 °C, the emission wavelength recorded was 550 nm (2.25 eV); however, the wavelength increased to 686 nm (1.81 eV) at 200 °C and finally redshifted to 693 nm (1.79 eV) at 230 °C.

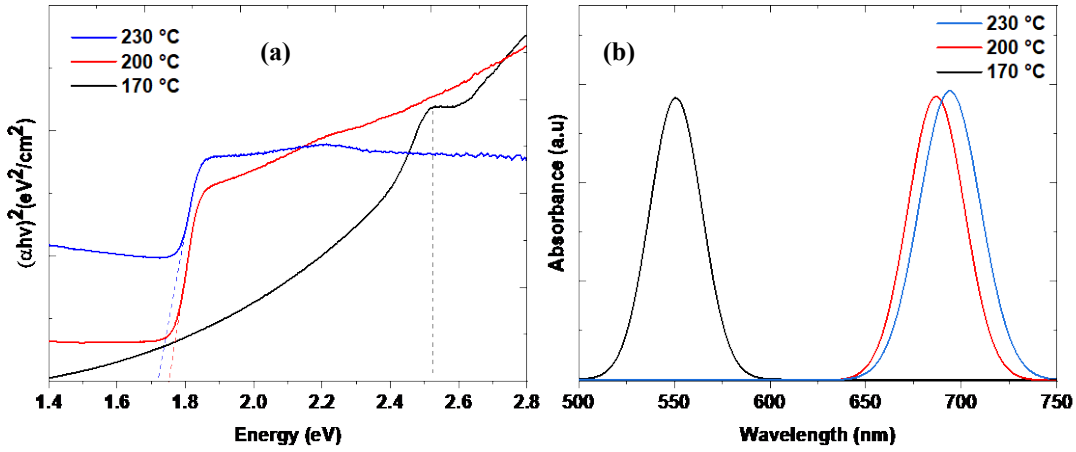

Fig. 3.3: (a) UV-vis absorption spectroscopy (b) PL emission spectroscopy of $CsSnBr_3$ at different temperature.

3.3.2 Effect of time on $CsSnBr_3$ nanocrystals

The effect of reaction time on the perovskite was investigated to garner further insight on the behavior of the perovskite at 1 min, 5 min and 10 min and to determine the most ideal condition for the synthesis of the Pb-free perovskite. Due to the quick reactivity of perovskites during the

hot-injection colloidal synthesis, the reaction time was varied from 1 min to 10 min. Since the $CsSnBr_3$ NCs synthesized at 230 °C has the lowest bandgap energy, it was used to investigate the effect of time. From the XRD pattern in Fig. 3.4, the ideal cubic perovskite was synthesized at 1 min and 5 min with pm-3m (221) space group and card number PDF 01-070-1645. However, at an extended period (10 min), secondary peaks began to emerge in the XRD pattern of the perovskite. The secondary peaks are marked with an asterisk in Fig. 3.4 and they are attributed to the possible transition of the cubic Pm-3m $CsSnBr_3$ to cubic Fm-3m Cs_2SnBr_6 nanocrystals. Such phase transitions at high temperatures have previously been reported in the literature about perovskites [10, 11].

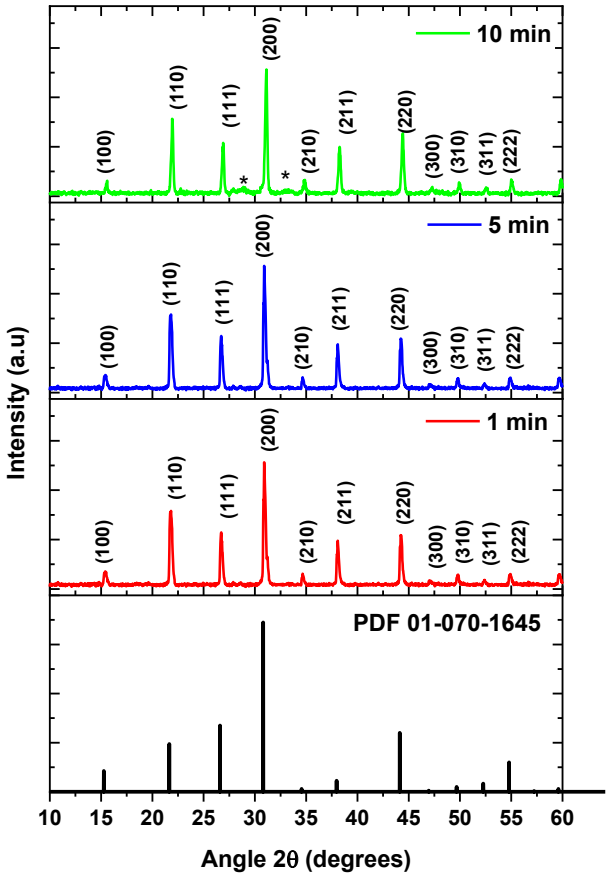

Fig. 3.4: XRD patterns of $CsSnBr_3$ nanocrystals synthesized at different reaction times.

The TEM images of the NCs synthesized at different reaction time is shown in Fig. 3.5. The NCs synthesized at 1 min and 5 min reaction time both have a particle size of 3 nm as shown from their respective histograms. However, at 10 min the particle size distribution could not be accurately determined due to severe agglomeration observed in the material. The

agglomeration observed at 10 min could be related to the phase transition of the perovskite material as initially suggested from the XRD pattern of 10 min.

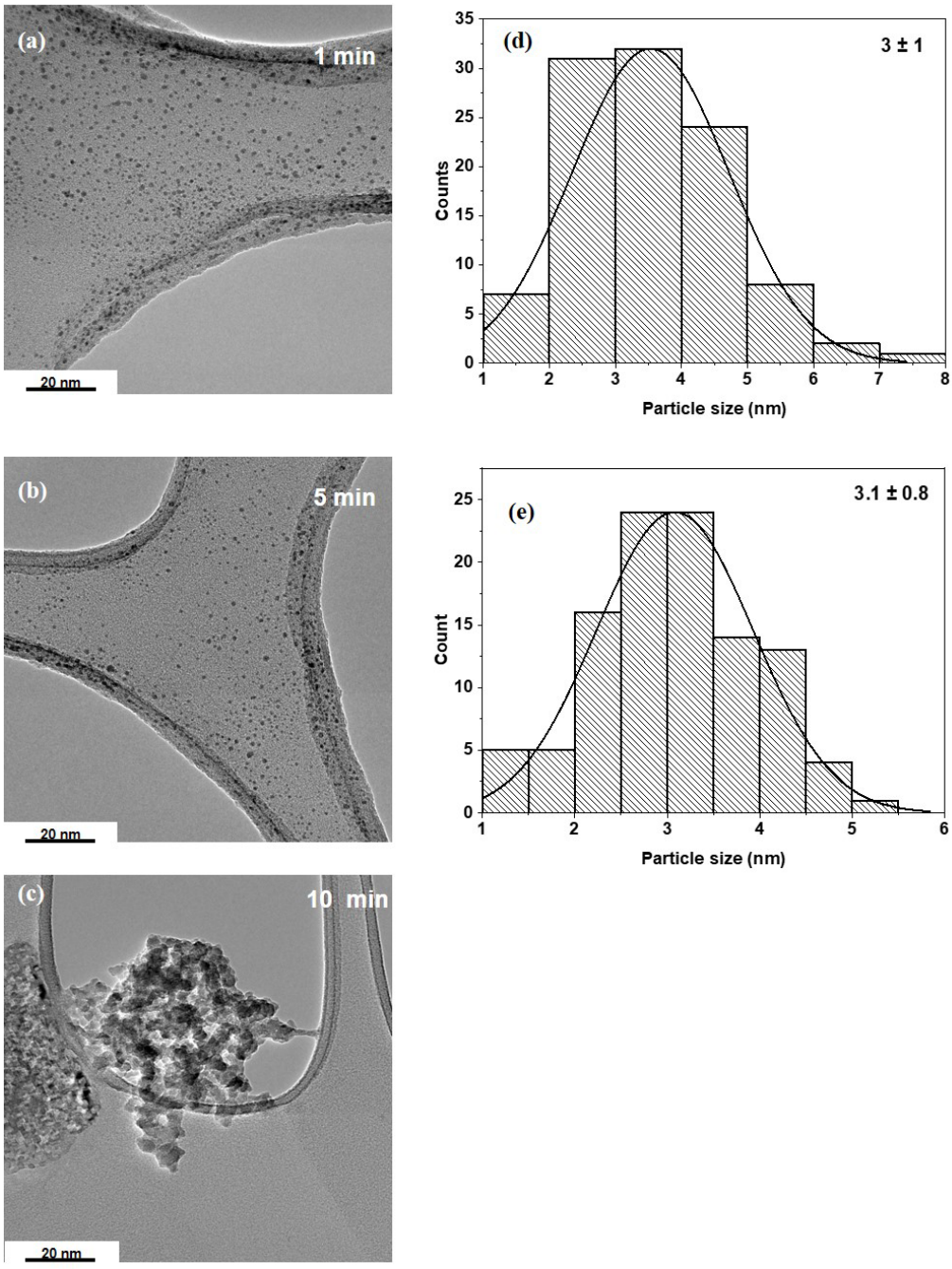

Fig. 3.5: (a-b) TEM images and (d-e) corresponding size distribution of $CsSnBr_3$ NCs synthesized at different times.

The absorption spectra of the NCs at different times are shown in Fig. 3.6. At 1 min and 5 min, the bandgap energy of the perovskite was 1.72 eV and 1.70 eV respectively. However, at 10 min, the bandgap energy red-shifted to 1.66 eV. The values of the bandgap energies suggest that the samples from 1 min and 5 min syntheses were made of well distributed smaller sized particles compared to the particles prepared at 10 min. The PL spectra show a red-shifting in

the emission peaks of the NCs from 687 nm (1.80 eV) at 1 min to 691 nm (1.79 eV) at 5 min. Finally, an emission peak at 704 nm (1.76 eV) was recorded for 10 min. The $CsSnBr_3$ synthesized at 230 °C for 1 min was investigated further with other techniques as detailed in the next sections.

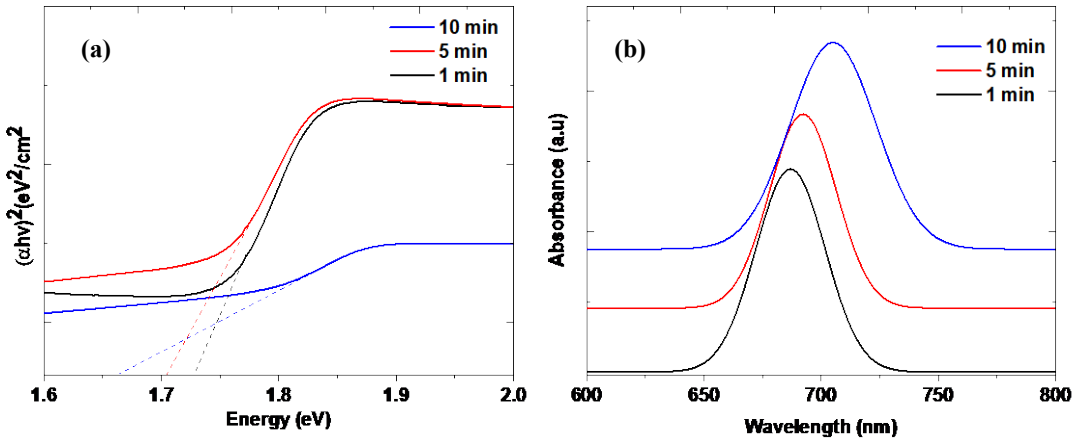

Fig. 3.6: (a) UV-vis spectra and (b) PL spectra of $CsSnBr_3$ nanocrystals synthesized at different times.

Cyclic voltammetry was used for the determination of the electrochemical bandgap (E_{bg}) and for the estimation of the conduction band minimum (CBM) and valence band maximum (VBM) of the $CsSnBr_3$ NCs where a ferrocene/ferrocenium redox couple was used as the internal standard. For the electrochemical investigation of the $CsSnBr_3$ synthesized at 230 °C for 1 min, the CV measurements were carried out at room temperature in an inert atmosphere with the conventional three-electrode system within a potential range of 1 V to -2.5 V as shown in Fig. 3.7.

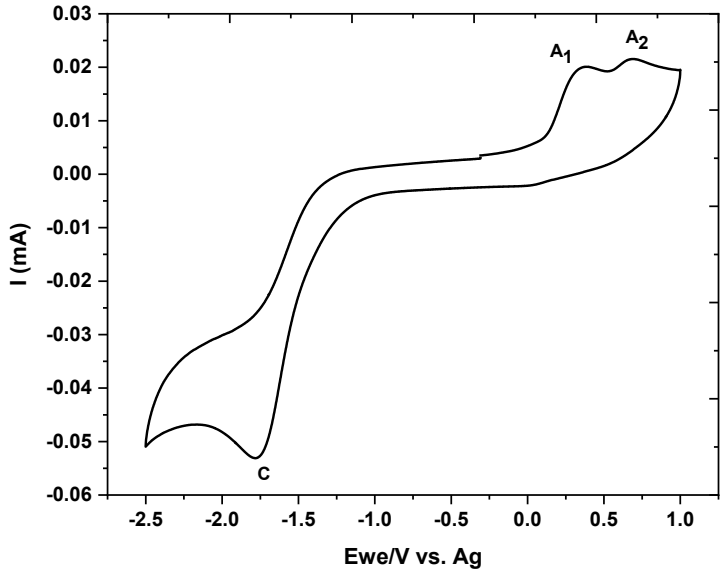

Fig. 3.7: Cyclic voltammogram of $CsSnBr_3$.

From the cyclic voltammogram of $CsSnBr_3$ shown in Fig. 3.7, the oxidation and reduction peaks of the perovskite were identified at 0.33 V and - 1.74 V respectively and are indicated as A_1 and C. The potential difference of these 2 peaks is called the electrochemical bandgap and is often close to the optical bandgap derived from absorption measurements [12]. The potential difference between A_1 and C (2.07 eV) differs slightly from the 1.85 eV optical bandgap obtained from the UV-vis measurement. The energy band levels of $CsSnBr_3$ NCs were estimated with the following equation.

$$E_{HOMO} = [-4.5 - E_{ox}]\ eV \quad (3.1)$$

$$E_{LUMO} = [-4.5 - E_{red}]\ eV \quad (3.2)$$

Where E_{HOMO} and E_{LUMO} represent the HOMO and LUMO energy levels respectively while E_{ox} and E_{red} are the oxidation and reduction peak potential of $CsSnBr_3$ NCs respectively. Using equations 3.1 and 3.2, the VBM and CBM of $CsSnBr_3$ NCs are -4.83 eV and -2.76 eV respectively. An additional peak indicated as A_2 at 0.7 V is observed in the cyclic voltammogram of $CsSnBr_3$ and this peak is ascribed to possible trap states in the perovskite [12]. The presence of multiple anodic and cathodic peaks in the cyclic voltammograms of perovskites is not uncommon as seen from literatures [12–14]. Also, interference from the reduced products of the perovskite has been suggested to be responsible for such additional

peaks since perovskites are very susceptible to dissolution in polar solvents used in the cyclic voltammetry measurements [15].

Raman spectroscopy was carried out to determine the vibrational modes of the $CsSnBr_3$ perovskite. The $CsSnBr_3$ NCs as reported from the XRD pattern belongs to the cubic phase with a space group of *Pm-3m* (221) indicating it belongs to the O_h point group where the Mulliken symbols A_{1g}, E_g and T_{2g} of the O_h groups show Raman activity by having the quadratic functions. However, due to the lack of literature on the Raman spectrum of $CsSnBr_3$, the analogous cubic $MAPbBr_3$ with a similar space group as $CsSnBr_3$ was employed to elucidate the Raman spectrum of $CsSnBr_3$. The Raman spectrum of $CsSnBr_3$ shows a broad peak at 328 cm^{-1} (Fig 3.8) as similarly observed in the spectrum of $MAPbBr_3$. This peak is attributed to the torsional vibration of MA with its motion coupled with the inorganic cage through the NH-Br hydrogen bonds [16]. Hence inference can be drawn that the peak is attributed to the Cs-Br torsional vibration.

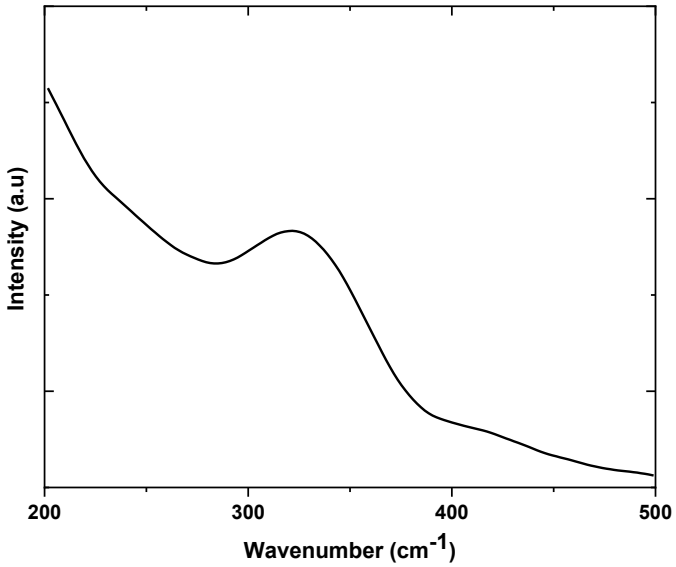

Fig. 3.8: Raman spectrum of $CsSnBr_3$.

X-ray photoelectron spectroscopy (XPS) was carried out on the perovskite. The survey spectrum and the high-resolution XPS spectra of the constituent elements in the capped $CsSnBr_3$ NCs are shown in Fig 3.9. Due to the spin-orbit coupling, the Cs 3d and Sn 3d give 2 peaks while the chemical environment of each constituent element was probed by deconvoluting their spectra. The high-resolution spectrum of Cs 3d showed 2 peaks at 724.5

eV and 738.4 eV attributed to $3d_{5/2}$ and $3d_{3/2}$ of Cs^+ [17]. Also, the doublet separation of these peaks is 13.8 eV which agrees with the standard peak separation of Cs 3d [18,19]. The Sn 3d spectrum showed two distinct peaks at 486.8 eV (3d $_{5/2}$) and 495.2 eV (3d $_{3/2}$) [20,21]. The doublet separation of the two Sn 3d peaks is 8.4 eV and this is in good agreement with the literature [22]. The Sn 3d peak at 486.8 is attributed to $SnBr_2$ bonding while the peak observed at 495.2 eV is assigned to SnO_2 which indicates the oxidation of Sn in the $CsSnBr_3$ NCs [20,21]. Gupta *et al*., [4] synthesized cubic $CsSnBr_3$ perovskite NCs and upon irradiation with the X-ray beam of the XPS, the material showed susceptibility to beam damage due to the generation of additional peaks at 493 eV and 484.5 eV. These peaks were attributed to the formation of Sn^0, therefore, to improve their perovskite's stability, SnF_2 was added. It is noteworthy that such beam damage was not observed during our characterization since aside from the expected double peaks of Sn 3d, no additional peaks were observed in our sample as confirmed in Fig. 3.9. The high-resolution Br 3d spectrum was deconvolved into two peaks at 68.2 eV ($3d_{5/2}$) and 69.3 eV ($3d_{3/2}$) where both peaks are attributed to the CsBr bonding in the sample [17]. The C 1s peaks were deconvolved to three distinct spectra at binding energies. The sharp peak at 284.4 eV is assigned to the C-C bonds originating from the alkyl chains of the capping agents. The C-O and O-C=O peaks located at 286.1 eV and 288.5 eV are from the oxidation of the capping agents.

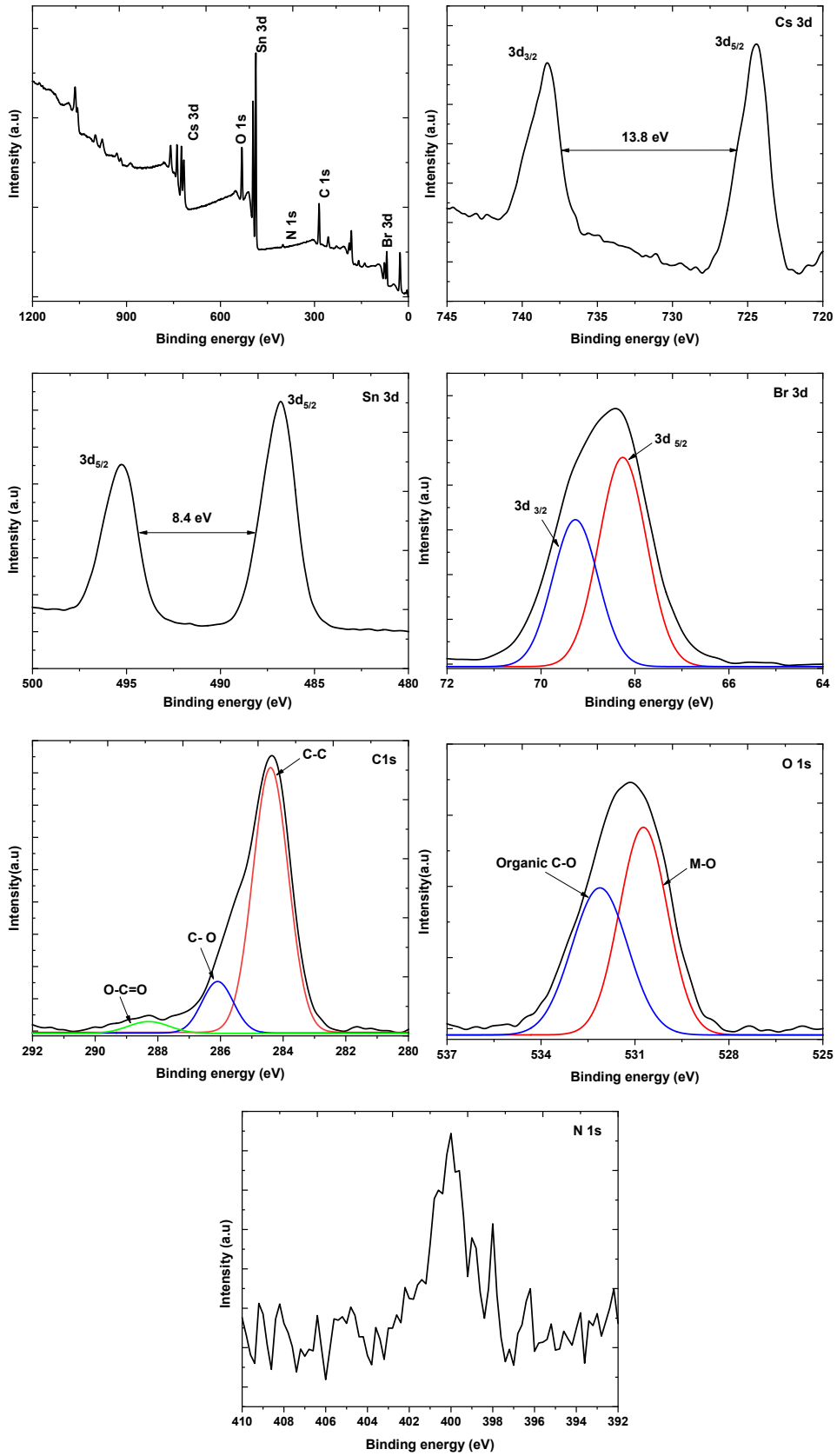

Fig. 3.9: XPS spectra of $CsSnBr_3$ nanocrystals.

The increase in BE from the C-C peak to the carbonyl peak is attributed to the bonding of C to a more electronegative element (O). Since oxygen is more electronegative, the electron density of the C is pulled away towards the more electronegative element, consequently increasing the binding (BE). The high-resolution O 1s spectrum peak was deconvoluted into two peaks, where the peak at 530.7 eV is attributed to the metal oxides while organic C-O was at 532.2 eV. The N 1s peak observed at 400 eV is assigned to organic N [23] which is from the OLA used in the $CsSnBr_3$ synthesis. This is an affirmation of the successful capping of oleylamine onto the perovskite's surface.

Table 3.1: Summary of the atomic composition and stoichiometric assignments obtained from the fitting of the XPS spectra of $CsSnBr_3$ nanocrystals

Element	Peak binding energy (eV)	Atomic %	Assignment	Assignment binding energy (eV)
Cs	724.8	2.3	Cs $3d_{5/2}$	724.5
			Cs $3d_{3/2}$	738.3
Sn	487.2	9.4	Sn $3d_{5/2}$	486.8
			Sn $3d_{3/2}$	495.2
Br	69.0	69.0	Br $3d_{5/2}$	68.2
			Br $3d_{3/2}$	69.3
C	285.1	51.1	C-C	284.4
			C-O	286.1
			O-C=O	288.5
N	400	9.2		
O	531.6	25.2	M-O	530.7
			C-O	532.2

FTIR analysis was performed to confirm the presence of the capping agents on the NC's surface. Pure samples of the capping agents (OLA and OA) were analyzed along with the $CsSnBr_3$ perovskite as shown in Fig. 3.10 and the results are summarized in Table 3.2. Both the OLA and OA show all the expected bands with their symmetric (ν_s) and asymmetric (ν_{as}) stretching vibrations at 2845 cm^{-1} and 2923 cm^{-1}. The sharp peak at 1709 cm^{-1} in the pure OA is the characteristic peak assigned to C=O stretching vibration while the characteristic N-H

band of OLA is located at 1586 cm^{-1}. As revealed from the FTIR spectra in Fig. 3.10, no C-O or C=O bands are present in the $CsSnBr_3$ spectrum and this indicates that the OA was not capped to the $CsSnBr_3$ NC surface. However, the N-H band of the OLA was notably present in the $CsSnBr_3$ spectrum indicating successful capping of OLA to the perovskite's surface. The preferential bonding of OLA on the NCs may be due to the higher nucleophilicity than the acid.

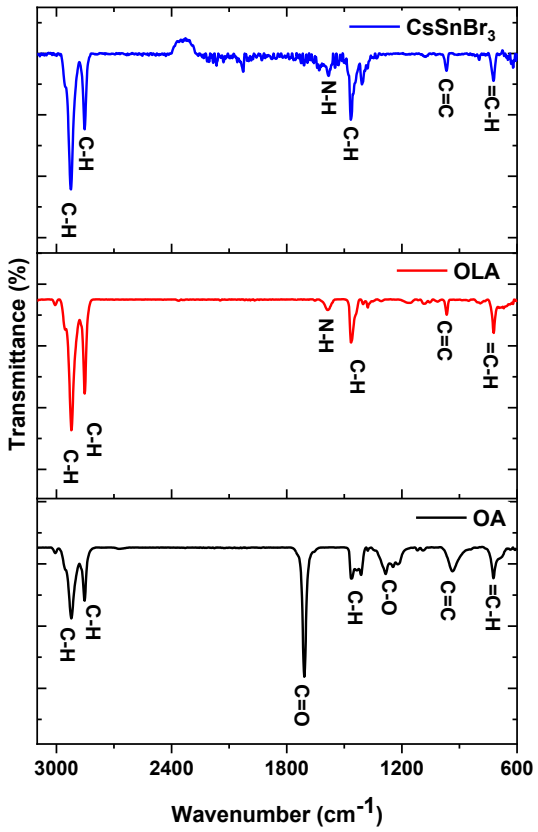

Fig. 3.10: FTIR spectra of OA, OLA and $CsSnBr_3$.

Table 3.2: FTIR assignments for oleic acid, oleylamine and $CsSnBr_3$ nanocrystals

Assignment	OA	OLA	$CsSnBr_3$
=C-H	715 cm^{-1}	715 cm^{-1}	715 cm^{-1}
C=C	926 cm^{-1}	967 cm^{-1}	967 cm^{-1}
C-H	1467 cm^{-1}, 2845 cm^{-1}, 2923 cm^{-1}	1467 cm^{-1}, 2845 cm^{-1}, 2923 cm^{-1}	1467 cm^{-1}, 2845 cm^{-1}, 2923 cm^{-1}
C-O	1265 cm^{-1}	-	-
C=O	1709 cm^{-1}		

N-H	-	1586 cm^{-1}	1579 cm^{-1}

While FTIR is a very informative technique, it is however not conclusive. Therefore, to further elucidate on the capping, NMR spectroscopy was done. The spectra are shown in Fig 3.11 and 3.12 and the results are summarized in Table 3.3. From the ^{1}H and ^{13}C NMR spectra of OLA and OA, all the protons and carbons were accounted for. The characteristic $CdCl_3$ peaks for the ^{1}H and ^{13}C NMR are located at 7.26 and 77 ppm respectively.

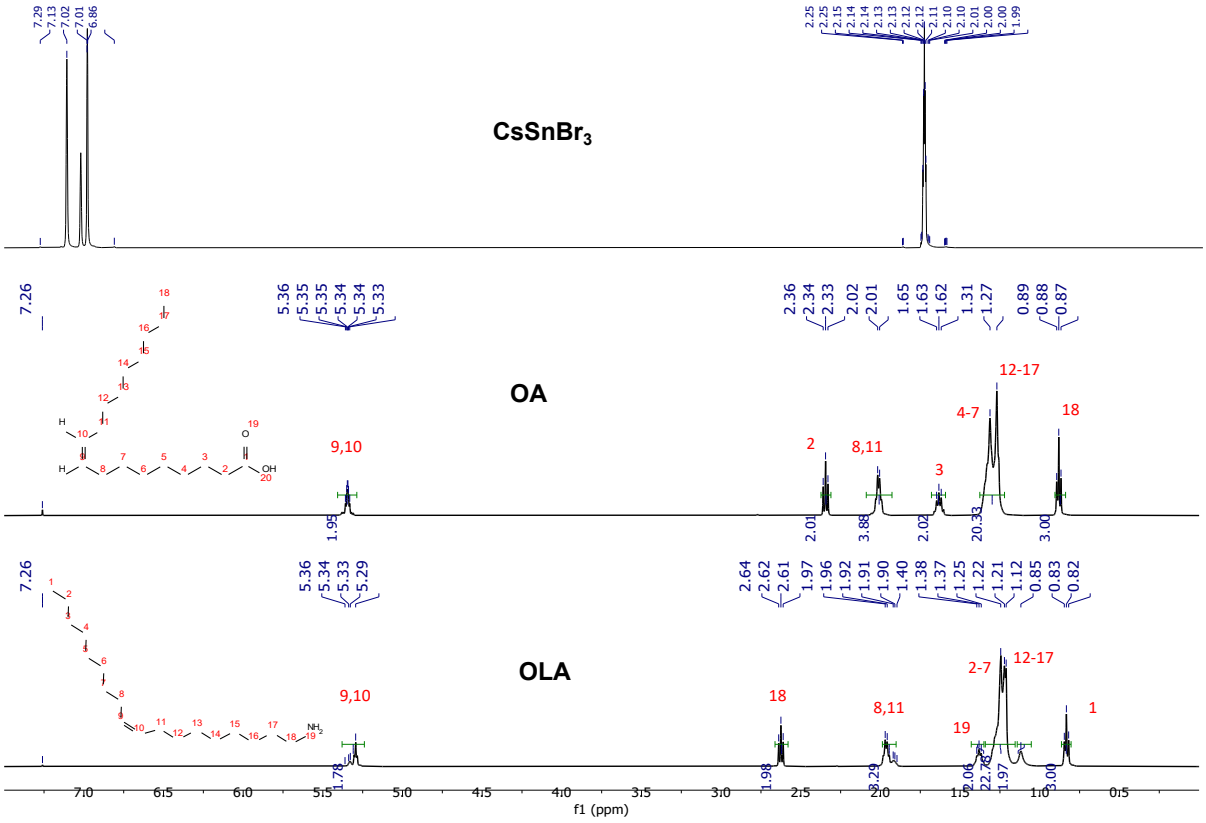

Fig. 3.11: ^{1}H NMR spectra of OLA, OA and $CsSnBr_3$ nanocrystals.

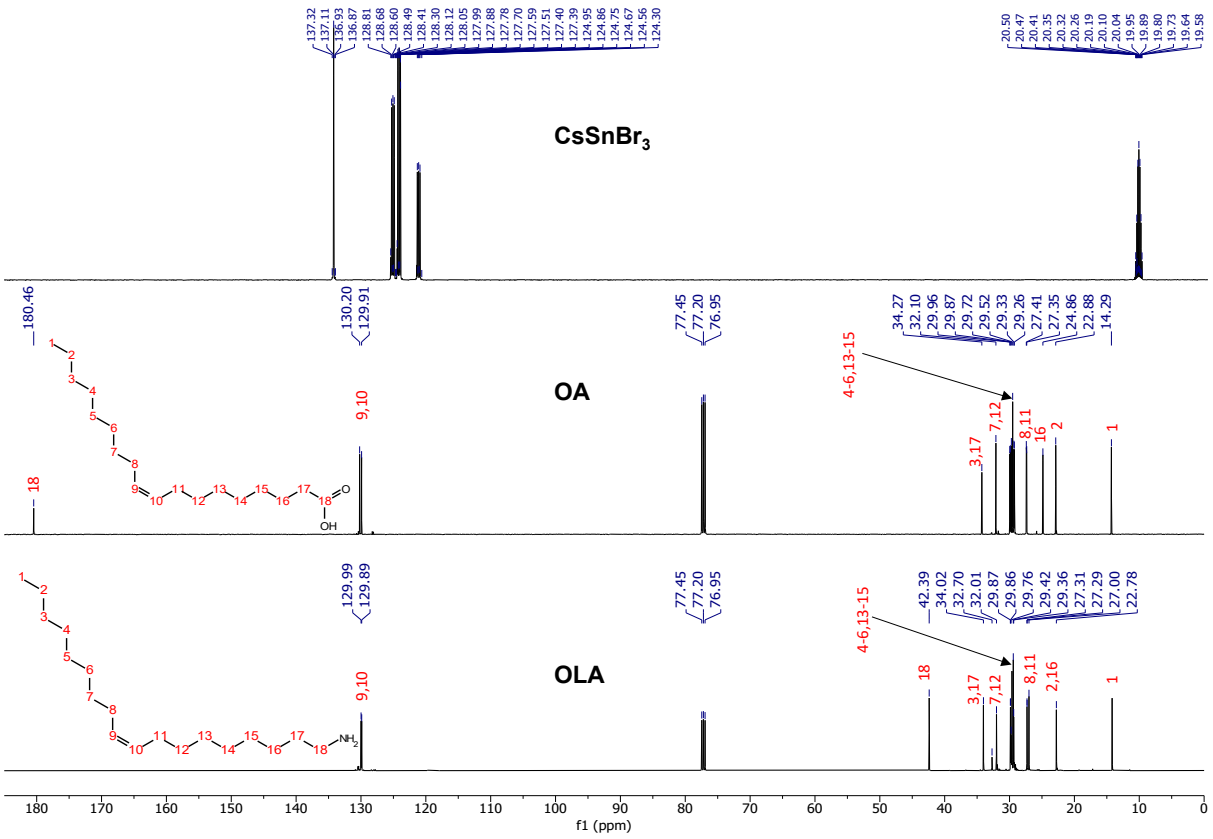

Fig. 3.12: ^{13}C NMR spectra of OLA, OA and $CsSnBr_3$ nanocrystals.

The characteristic peaks for OLA were the NH_2 (1.37-1.40 ppm) and the -CH_2-NH_2 (2.61-2.64) in the ^{1}H NMR spectrum and the -CH_2-NH_2 (42.39) in the ^{13}C NMR spectrum. While for the OA, the -CH_2-C=O (2.33 – 2.36 ppm) chemical shifts in the proton spectrum and C=O (180.46 ppm) chemical shift in the ^{13}C spectrum were the distinguishing bands. The ^{1}H NMR spectrum of the $CsSnBr_3$ NCs showed intense toluene peaks arising from the solvent used to wash and disperse the NCs. The perovskite's ^{1}H NMR spectrum also shows the -CH_2-NH_2 (2.12 – 2.25 ppm) peaks. These peaks suggest that only OLA is capped on the NCs surface. The absence of OA capping was further confirmed from the ^{13}C NMR spectrum of $CsSnBr_3$ NCs since no C=O peaks of the OA were observed. The NMR results are consistent with the FTIR results where only the N-H bands are observed in the $CsSnBr_3$ spectrum.

Table 3.3: NMR assignments for oleylamine, oleic acid and $CsSnBr_3$ nanocrystals

Compound	^{1}H NMR (δ ppm)	^{13}C NMR (δ ppm)
OLA	$-CH_3$ (0.82 – 0.85), $-CH_2-$ (1.12 – 1.25), $-CH_2-CH=CH-CH_2-$ (1.90 – 1.97), $-NH_2$ (1.37 – 1.40), $-CH_2-NH_2$ (2.61 – 2.64), CH=CH (5.29 – 5.36)	$-CH_3$ (22.78), $-CH_2-$ (27.00 – 34.02), $-CH_2-NH_2$ (42.39), CH=CH (129.91 – 130.20)
OA	$-CH_3$ (0.87 – 0.89), $-CH_2-$ (1.27 – 2.02), $-CH_2-C=O$ (2.33 – 2.36), CH=CH (5.33 – 5.36)	$-CH_3$ (14.29), $-CH_2-$ (22.88 – 34.27), CH=CH (129.91 – 130.20), C=O (180.46)
$CsSnBr_3$	$-CH_2$ (1.99), CH_3 toluene (2.10), $-CH_2-NH_2$ (2.12 – 2.25), CH toluene (6.86 – 7.13)	$-CH_3$ (19), CH toluene (122.5 & 125.5), CH=CH (127), C toluene (137)

Perovskites are characterized with instability due to factors such as air and moisture. The mechanism of this degradation has been exhaustively discussed in Chapter 2. To maximize the properties of the $CsSnBr_3$ NCs for different applications, stability studies were conducted. Prior to analysis, the NCs were kept in ambient conditions contrary to the controlled environment required for some perovskites. From the XRD pattern in Fig. 3.13, the crystal structure and phase of the perovskite remained unchanged for the first 3 days. However, by day 4, secondary peaks indicated with asterisks began to appear and finally after 21 days, these peaks are very pronounced.

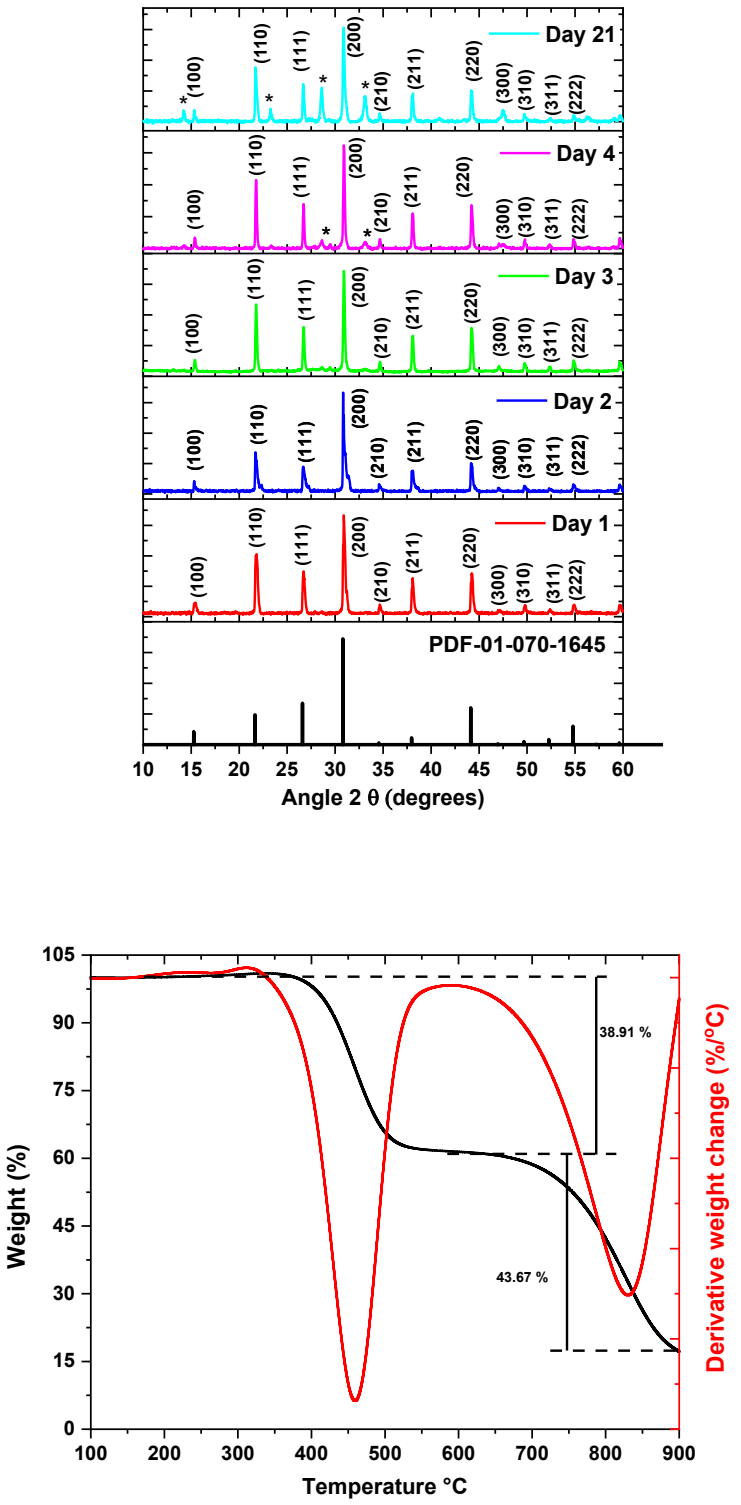

Fig. 3.13: Stability study of $CsSnBr_3$ nanocrystals synthesized at 230 °C for 1 min using XRD and TGA (* = peaks associated with $CsSnBr_3$ degradation).

The secondary peaks formed are attributed to the oxidation of Sn^{2+} to Sn^{4+} in the perovskite. Similar oxidation of Sn^{2+} to Sn^{4+} has been reported for the Sn-based perovskites [24]. However, it is significant to mention that the $CsSnBr_3$ NCs synthesized here showed improved stability in comparison to other reported $CsSnBr_3$ perovskites. For instance, Wang *et al*., [9] synthesized $CsSnBr_3$ NCs *via* colloidal synthesis but the perovskite started degrading after 3 h and then completely decomposed after 16 h. Similarly, Moghe *et al*., [25] prepared $CsSnBr_3$ films and upon exposure to ambient conditions, the perovskite was only stable for about 25 h. TGA was done to determine the thermal stability of the perovskite NCs. The freshly prepared day 1 $CsSnBr_3$ NCs were used for the TGA. Weight percent graph in the TGA provides information about the quantity of weight changes as the decomposition proceeds. The derivative weight change graph however gives information about the rate of each decomposition step and the maximum temperature at which a particular decomposition step occurs. From the TGA spectrum in Fig. 3.13, the derivative weight curve shows two distinct decomposition peaks of the $CsSnBr_3$ NCs where the maximum temperatures for the two decompositions are located at 461 °C and 832 °C. The weight percent curve shows that about 38.9% of the perovskite's weight was lost during the first decomposition step while 43.67% weight was lost during the second decomposition process. The first decomposition of the $CsSnBr_3$ perovskite NCs is probably due to the release of organic residues since TGA of both OLA and OA have been reported to decompose at temperature range of around 300 – 450 °C [26]. The second decomposition at higher temperature however could be attributed to the degradation of CsBr in the material. CsBr has a molar mass of 212.80 g/mol, using proportionality, the 43.67% weight loss observed in the second decomposition process accounts to 214.5 g/mol of the total 491.32 g/mol molar mass of the $CsSnBr_3$ NCs. Also, CsBr sublimes at 650 °C and this corresponds to the onset region of the second degradation process. To accurately determine the decomposition products and the equation of decomposition, hyphenated techniques such as TGA-MS or TGA-FTIR are often used. Nevertheless, the TGA spectrum shows that the perovskite is thermally stable up to 400 °C before any appreciable weight loss is observed. The $CsSnBr_3$ perovskite NCs thermal stability was comparable to that of $CsPbBr_3$ [26] which further suggests that $CsSnBr_3$ is a potential substitute for the Pb-based perovskite in various applications.

3.4 Conclusion

$CsSnBr_3$ nanocrystals were synthesized *via* a simple hot-injection method with OLA and OA. The sizes and morphology changed with varying reaction time and temperature. 1 min and 230 °C are the optimum reaction time and temperature for the synthesis of the $CsSnBr_3$ nanocrystals. The XPS analysis confirmed the composition of $CsSnBr_3$ and the capping agents of the nanocrystals. Further confirmation of the capping agent was done with NMR and FTIR where both spectra conclusively show that only oleylamine was capped to the nanocrystals' surface. From the XRD and TGA, the samples were found to be stable for 3 days before the oxidation of the Sn^{2+} while the appreciable decomposition temperature of $CsSnBr_3$ starts at 364 °C.

3.5 References

[1] F. Giustino, H.J. Snaith, *ACS Energy Letters* 1 (2016) 1233–1240.

[2] K.A. Winship, *Adverse Drug Reactions and Acute Poisoning Reviews* 7 (1988) 19–38.

[3] B. Li, R. Long, Y. Xia, Q. Mi, *Angewandte Chemie International Edition* 57 (2018) 13154–13158.

[4] S. Gupta, T. Bendikov, G. Hodes, D. Cahen, *ACS Energy Letters* 1 (2016) 1028–1033.

[5] Cb. Murray, D.J. Norris, M.G. Bawendi, *Journal of the American Chemical Society* 115 (1993) 8706–8715.

[6] X. Peng, J. Wickham, A. Alivisatos, *Journal of the American Chemical Society* 120 (1998) 5343–5344.

[7] Y. Pu, F. Cai, D. Wang, J.-X. Wang, J.-F. Chen, *Industrial and Engineering Chemistry Research* 57 (2018) 1790–1802.

[8] T.C. Jellicoe, J.M. Richter, H.F.J. Glass, M. Tabachnyk, R. Brady, S.E. Dutton, A. Rao, R.H. Friend, D. Credgington, N.C. Greenham, M.L. Böhm, *Journal of the American Chemical Society* 138 (2016) 2941–2944.

[9] A. Wang, Y. Guo, F. Muhammad, Z. Deng, *Chemistry of Materials* 29 (2017) 6493–6501.

[10] Y.J. Sohn, G. Mauer, G. Roth, O. Guillon, R. Vaßen, *Journal of the American Ceramic Society* 103 (2020) 1404–1413.

[11] D.G. Billing, A. Lemmerer, *Acta Crystallographica Section B: Structural Science* 63 (2007) 735–747.

[12] D. Cardenas-Morcoso, A.F. Gualdrón-Reyes, A.B. Ferreira Vitoreti, M. García-Tecedor, S.J. Yoon, M. Solis de la Fuente, I. Mora-Seró, S. Gimenez, *The Journal of Physical Chemistry Letters* 10 (2019) 630–636.

[13] Y.D. Gujarathi, S.K. Haram, *Materials Chemistry and Physics* 173 (2016) 491–497.

[14] H. R. Xia, W.-T. Sun, L.-M. Peng, *Chemical Communications* 51 (2015) 13787–13790.

[15] M. Hasan, S. Venkatesan, D. Lyashenko, J.D. Slinker, A. Zakhidov, *Analytical Chemistry* 89 (2017) 9649–9653.

[16] K. Nakada, Y. Matsumoto, Y. Shimoi, K. Yamada, Y. Furukawa, *Molecules* 24 (2019).

[17] W.E. Morgan, J.R. Van Wazer, W.J. Stec, *Journal of the American Chemical Society* 95 (1973) 751–755.

[18] M. Roy, S. Ghorui, Bhawna, J. Kangsabanik, R. Yadav, A. Alam, M. Aslam, *The Journal of Physical Chemistry C* 124 (2020) 19484–19491.

[19] M. Zhang, Z.-Q. Tian, D.-L. Zhu, H. He, S.-W. Guo, Z.-L. Chen, D.-W. Pang, *New Journal of Chemistry* 42 (2018) 9496–9500.

[20] W. Choi, H. Jung, S. Koh, *Journal of Vacuum Science & Technology* A 14 (1996) 359–366.

[21] P. Grutsch, M. Zeller, T. Fehlner, *Inorganic Chemistry* 12 (1973) 1431–1433.

[22] M. Di Giulio, G. Micocci, A. Serra, A. Tepore, R. Rella, P. Siciliano, *Sensors and Actuators B: Chemical* 25 (1995) 465–468.

[23] K.L. Tan, B.T.G. Tan, E.T. Kang, K.G. Neoh, *Physical Review B* 39 (1989) 8070–8073.

[24] T. Wang, F. Yan, Chemistry – *An Asian Journal* 15 (2020) 1524–1535.

[25] D. Moghe, L. Wang, C.J. Traverse, A. Redoute, M. Sponseller, P.R. Brown, V. Bulović, R.R. Lunt, *Nano Energy* 28 (2016) 469–474.

[26] J.B. Hoffman, G. Zaiats, I. Wappes, P.V. Kamat, *Chemistry of Materials* 29 (2017) 9767–9774.

CHAPTER 4

The effect of temperature and time on the synthesis of $Cs_3Bi_2Br_9$ perovskite nanocrystals

4.1 Introduction

Perovskite nanocrystals (NCs) are promising semiconductors for a plethora of applications. Due to their tunable bandgaps, impressive hole and electron mobility coupled with their high defect tolerance [1]**.** These materials have been used as sensors, photocatalysts and X-ray detectors. The instability of tin has been demonstrated in Chapter 3 and this is mostly related to the ease of oxidation of Sn^{2+} to Sn^{4+}. This instability presents a major challenge restricting the adoption of Sn as a Pb substitute in inorganic halide perovskites (IHPs). Therefore, other elements are being considered as Pb replacement. Bismuth (Bi) is one of the elements being considered as an alternative to Pb. Bi has an atomic number 83 and is in the same period as Pb where Bi^{3+} is isoelectronic to Pb^{2+} [2]. Despite the isoelectronic similarities between the 2 elements, Bi is considered less toxic than Pb hence Bi compounds such as bismuth vanadate have been used in cosmetics [3]. Furthermore, Bi-containing compounds have also been used in the pharmaceutical industry for decades in the treatment of syphilis and heartburn [3]. Due to this isoelectronic similarity and less toxicity of Bi compared to Pb, Bi-based perovskite derivatives have been gaining attention recently. The Bi^{3+} perovskite adopts the $A_3B_2X_9$ formula where trivalent cation such as Bi is substituted for Pb and Sn in the perovskite structure while A and X are cations and halides respectively. This $A_3B_2X_9$ based material is a polymorph of the vacancy-ordered triple perovskite and they are particularly useful due to their impressive stability and adoption of a less toxic element as a replacement for Pb. Herein, we investigate the synthesis of $Cs_3Bi_2Br_9$ perovskite using the colloidal synthesis. Also, the effect of changing reaction temperature and time on the properties of the $Cs_3Bi_2Br_9$ perovskite was investigated.

4.2 Experimental procedures

4.2.1 Chemicals

The same chemicals in Chapter 3 were used including bismuth bromide ($BiBr_3$, 98%) and hexane (95 %) that were all obtained from Sigma-Aldrich and used without further purification.

4.2.2 Synthesis of $Cs_3Bi_2Br_9$ nanocrystals

The same procedure as in Chapter 3 was followed, except that $BiBr_3$ was the metal precursor and the nanocrystals were washed with hexane.

4.2.3 Characterization techniques

The same characterization techniques were used as in Chapter 3.

4.3 Results and discussions

4.3.1 Effect of temperature on $Cs_3Bi_2Br_9$ nanocrystals

The study was done with 180 °C, 210 °C and 240 °C as variables for temperature of synthesis. Fig. 4.1 shows the reference pattern and the XRD patterns obtained at different temperatures. At 180 °C, some peaks were observed at 11°, 32° and 46° are indicated with an asterisk. These peaks were not matching the reference pattern and they are attributed to the likely presence of organic compounds from the capping agents as previously observed in other NCs [4]. However, at elevated temperatures (210 °C and 240 °C) all the peaks matched perfectly to the $Cs_3Bi_2Br_9$ and crystallized in the hexagonal phase with card number PDF 01-070-0493 and lattice parameters: a = 7.97200 Å, and c = 9.86700 Å. The $Cs_3Bi_2Br_9$ material belongs to the p-3m1 (164) space group with the sharp peaks indicative of crystallinity in the perovskite.

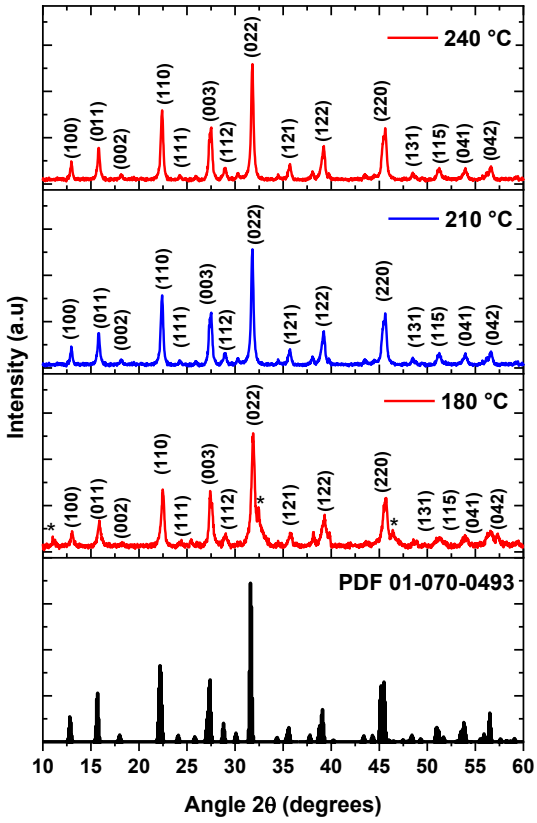

Fig. 4.1: XRD patterns of $Cs_3Bi_2Br_9$ nanocrystals synthesized at different temperatures.

The morphology of the NCs synthesized at different temperatures was determined with TEM. From the TEM images in Fig. 4.2, the $Cs_3Bi_2Br_9$ NCs synthesized at 180 °C showed nearly spherical particles with an average particle size of 27 ± 11 nm while the NCs synthesized at 210 °C showed improved uniform morphology with average NCs size of 17 ± 2 nm. The morphology seen at 180 ºC may be due to the presence of organics together with the pure $Cs_3Bi_2Br_9$ NCs. Finally, the NCs synthesized at 240 °C showed agglomeration coupled with polydispersity which is due to thermal agitation and isotropic growth of the NCs. $Cs_3Bi_2Br_9$ NCs were recently syntheszied using anti-solvent precipitation method [5]. The synthesized $Cs_3Bi_2Br_9$ NCs were used for ring-opening reactions of epoxides and similar agglomerated NCs were obtained.

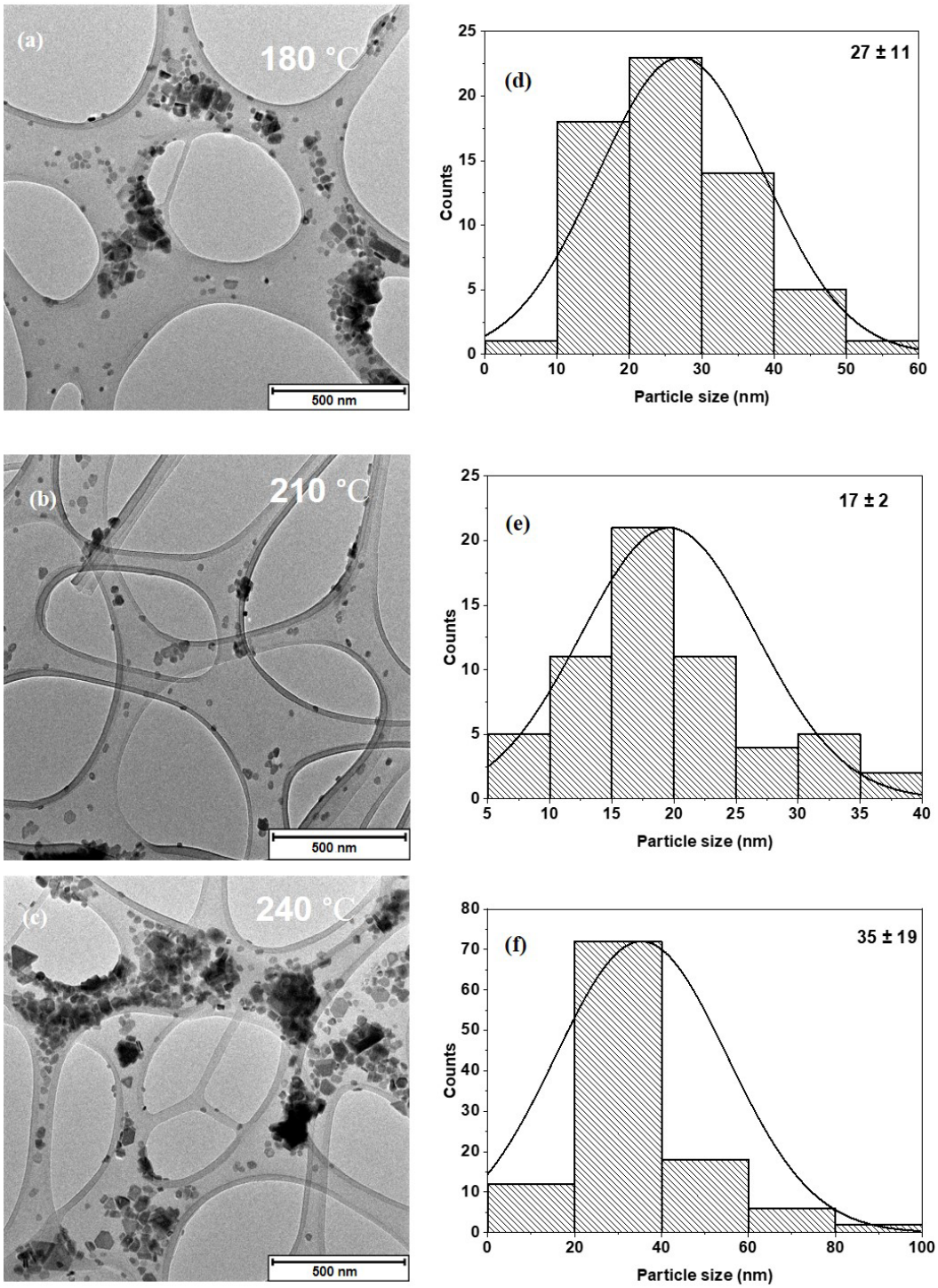

Fig. 4.2: (a-c) TEM images and (d-f) corresponding size distribution of $Cs_3Bi_2Br_9$ nanocrystals synthesized at different temperatures.

The optical properties of the $Cs_3Bi_2Br_9$ NCs synthesized at different temperatures were determined with UV-vis absorption and PL spectroscopy. For the determination of the bandgaps from the absorption measurements, the absorption wavelength values were converted

to energy using the Planck's equation. From the UV-vis spectra shown in Fig. 4.3(a), sharp excitonic peaks were observed and these peaks corresponds to bandgap energy of 2.85 eV (435 nm), 2.83 eV (438 nm) and 2.82 eV (439 nm) for 180 °C, 210 °C and 240 °C, respectively. The $Cs_3Bi_2Br_9$ NCs absorption measurements showed broad tailing peaks that were indicative of polydispersity of the NCs. The bandgaps reported here were slightly higher than the bandgap energy of 2.61 eV recorded for $Cs_3Bi_2Br_9$ single crystal [6]. From Fig. 4.3(b), the emission spectra of $Cs_3Bi_2Br_9$ NCs synthesized at 180 °C, 210 °C and 240 °C were located at 466 nm (2.66 eV), 478 nm (2.59 eV) and 482 nm (2.57 eV) respectively.

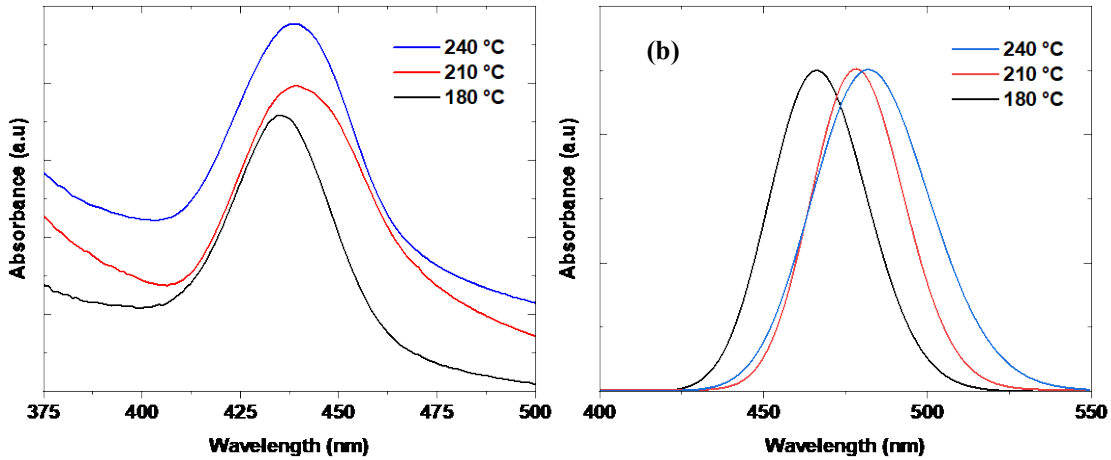

Fig. 4.3: (a) UV-vis absorption spectra and (b) PL emission spectra of $Cs_3Bi_2Br_9$ nanocrystals synthesized at different temperatures.

4.3.2 Effect of time on $Cs_3Bi_2Br_9$ nanocrystals

The synthesis of $Cs_3Bi_2Br_9$ NCs was set at 1 min, 5 min and 10 min to further gain insights into the behavior of the perovskite NCs as time is changed. The $Cs_3Bi_2Br_9$ NCs were more monodispersed at 210 °C hence the effect of time was studied at this temperature. Fig. 4.4 shows the XRD patterns of the $Cs_3Bi_2Br_9$ synthesized at different times. The XRD patterns were consistent from 1 min to 10 min with no deviation or noticeable peak shift. They were indexed to $Cs_3Bi_2Br_9$ (PDF 01-070-0493). The TEM images, as shown in Fig. 4.5, reveal that there is an increase in the size of the NCs as time progressed.

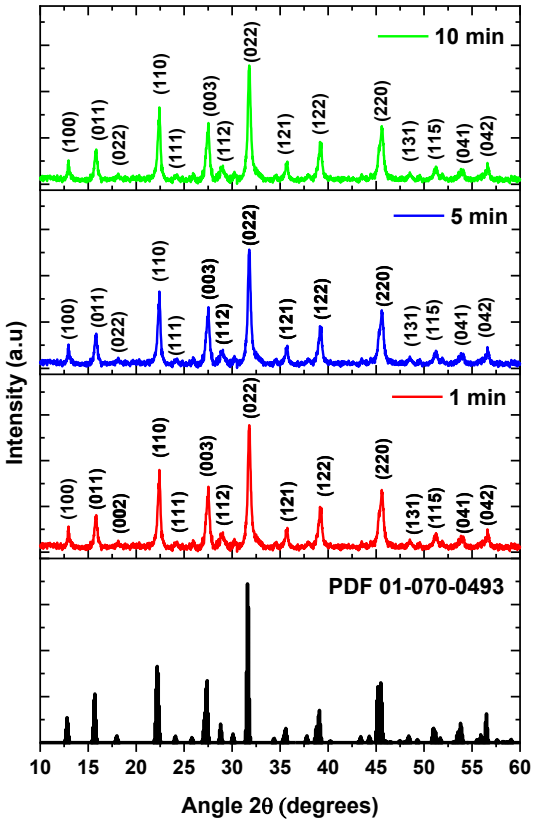

Fig. 4.4: XRD patterns of $Cs_3Bi_2Br_9$ nanoparticles at different reaction times.

At 1 min reaction time, *pseudo*-spherical $Cs_3Bi_2Br_9$ NCs with an average particle size of 17 ± 6 nm were obtained. The size of the NCs increased with reaction time where average particle sizes of 23 ± 16 nm and 40 ± 27 nm were obtained at 5 min and 10 min respectively. The increase in particles sizes with time is as a result of Ostwald ripening.

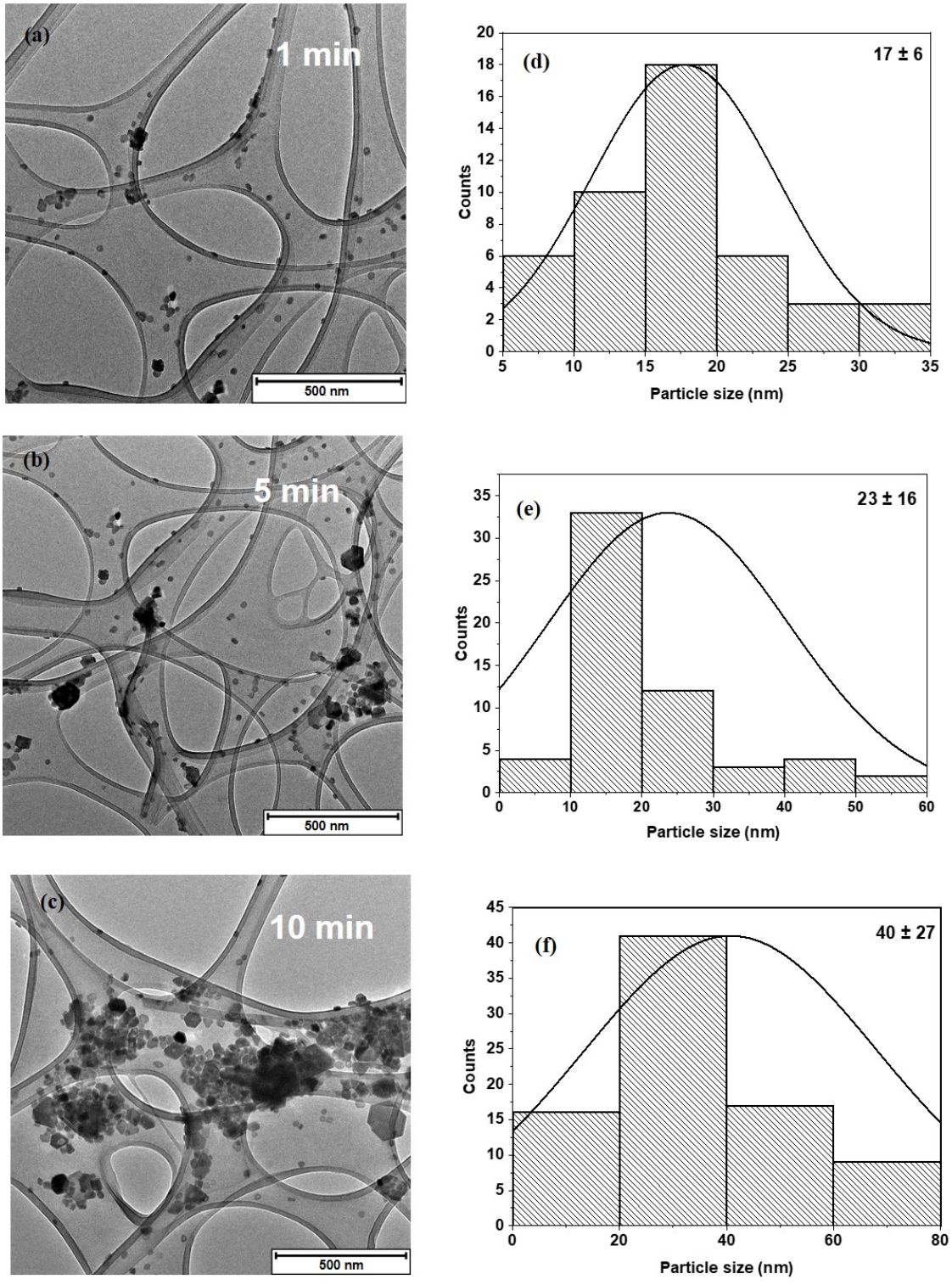

Fig. 4. 5: (a-c) TEM images and (d-f) corresponding size distribution of $Cs_3Bi_2Br_9$ synthesized at different reaction time.

The UV-vis spectra in Fig. 4.6(a) revealed that the bandgap energy of the $Cs_3Bi_2Br_9$ NCs gradually decreased from 2.83 eV (438 nm) to 2.79 eV (444 nm) and finally to 2.78 eV (446

nm) for 1, 5 and 10 min, respectively. This increase in bandgap energy with decreasing NCs size of the perovskite NCs is due to the quantum confinement effect, whereby the increase in spacing of the electronic levels resulting from the decrease in particle sizes leads to the increase in the semiconductor's bandgap energy. The PL spectra of $Cs_3Bi_2Br_9$ NCs are shown in Fig. 4.6(b). The NCs showed a steady red-shifting in their emission spectra wavelength. At 1 min, emission wavelength of 466 nm (2.66 eV) was observed, this increased to 478 nm (2.59 eV) and 482 nm (2.57 eV) at 5 min and 10 min reaction times. For further characterization of the $Cs_3Bi_2Br_9$ perovskite NCs, the optimum material synthesized at 210 °C for 1 min was used.

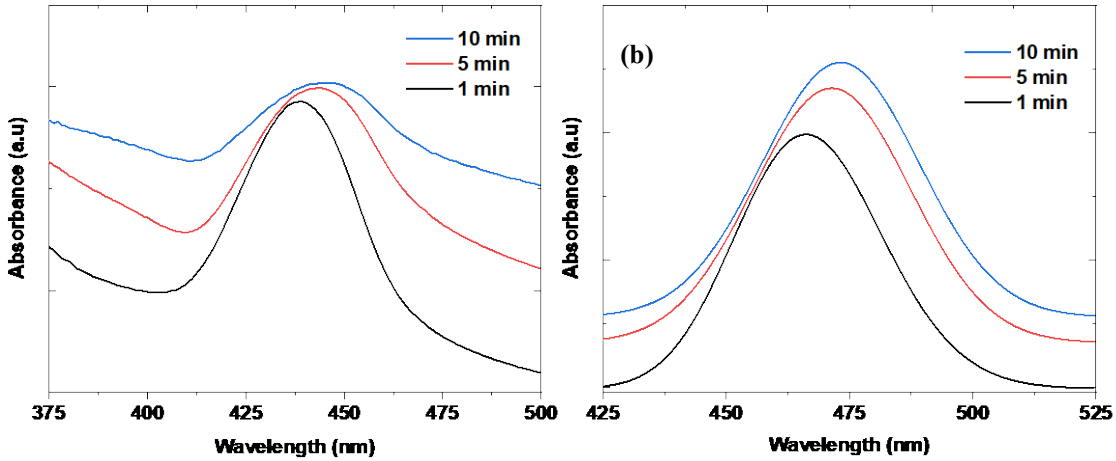

Fig. 4.6: (a) UV-vis absorption spectra and (b) PL spectra of $Cs_3Bi_2Br_9$ nanocrystals synthesized at different times.

The $Cs_3Bi_2Br_9$ electrochemical investigation was conducted at room temperature within a potential range of 3 V to -3 V as shown in Fig. 4.7. From the cyclic voltammogram of $Cs_3Bi_2Br_9$ in Fig. 4.7, the peak at +1.52 V and -1.56 V labelled as A and B, corresponds to the oxidation and reduction peaks respectively. The electrochemical bandgap derived from the oxidation and reduction peaks was 3.08 eV while the estimated valence band and conduction bands were -6.02 eV and -2.94 eV respectively.

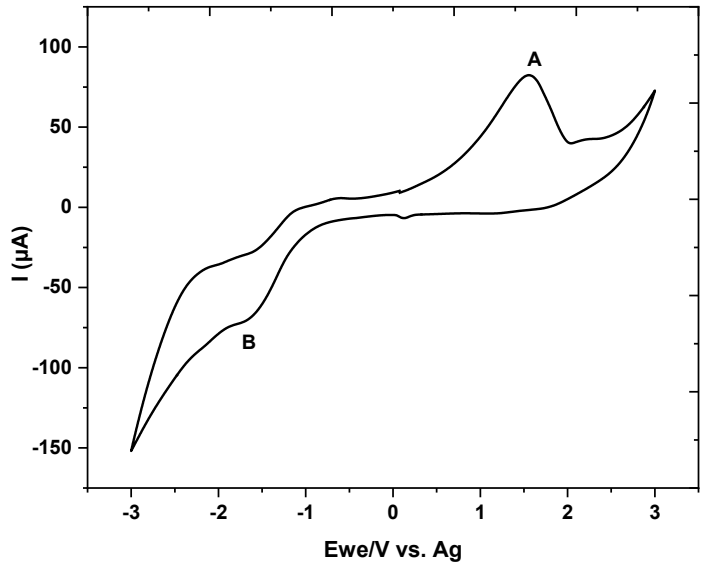

Fig. 4.7: Cyclic voltammogram of $Cs_3Bi_2Br_9$ nanocrystals.

Raman spectroscopy was used to probe the vibrational mode of the $Cs_3Bi_2Br_9$ NCs. $Cs_3Bi_2Br_9$ belongs to the p-m31 space group with general Raman modes represented by $\Gamma(Vib) = (4A_{1g} + A_{2g} + 5E_g) + (2A_{1u} + 6A_{2u} + 8E_u)$. Two vibration modes are more important in the characterization of $Cs_3Bi_2Br_9$ namely A_{1g} and E_g [7]. From the Raman spectrum of the NCs synthesized at 210 °C for 1 min as shown in Fig. 4.8, the A_{1g} and E_g vibration modes were observed at 166 cm^{-1} and 191 cm^{-1} respectively. These peaks appeared at similar wavenumbers as those earlier reported by Ghosh *et al.,* [7] who initially characterized the Raman spectrum of $Cs_3Bi_2Br_9$ NCs.

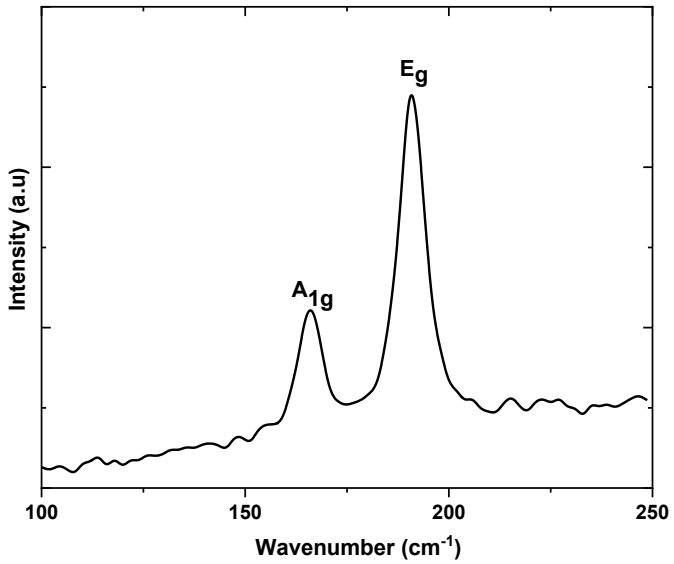

Fig. 4. 8: Raman spectrum of $Cs_3Bi_2Br_9$ nanocrystals.

XPS measurements were carried out to investigate the compositional and surface properties of the $Cs_3Bi_2Br_9$ NCs. The spectrometer dispersion is adjusted to the binding energy of 284.8 eV for the C 1s line of adventitious carbon. Due to spin-orbit coupling, the Cs 3d and Bi 4f gives two peaks. The broad survey spectrum and the high-resolution XPS spectra of Cs 3d, Bi 4f, Br 3d, C 1s, N 1s and O 1s are shown in Fig. 4.9. The Cs 3d high-resolution spectrum showed two distinct peaks at 724 eV and 738 eV corresponding to the $3d_{5/2}$ and $3d_{3/2}$ of Cs^+. The Cs 3d doublet separation of 13.9 eV perfectly agrees with the standard peak separation of Cs 3d [8, 9]. The Bi 4f spectrum show peaks centered at 158.7 eV and 164.1 eV, which correlates to the $4f_{7/2}$ and $4f_{5/2}$ of the Bi^{3+} ions [10]. The f-level spin-orbit split for Bi is 5.4 eV which is in agreement with previous literature [11]. The high-resolution Br 3d spectrum was deconvoluted into two peaks at 68.2 eV (Br $3d_{5/2}$) and 68.8 eV (Br $3d_{3/2}$) which both correspond to the CsBr bonding in the material [12]. The C 1s peaks were deconvoluted and fitted to three distinct peaks. The intense peak at 284.6 eV is assigned to the C-C bonds originating from the alkyl chains of the capping agents. Also, this peak is more pronounced compared to other deconvoluted carbon peaks due to the contribution of adventitious carbon (284.6) on the material. The C-O and O-C=O peaks are attributed to the oxidation of the capping agents. The O 1s spectrum showed three deconvoluted peaks at 529.4 eV, 531 eV and 533 eV corresponding to the metal oxide [13], C-O and C=O interactions in the sample respectively

[14]. No distinct peak was observed in the N 1s spectrum due to the low intensity of Nitrogen in the sample.

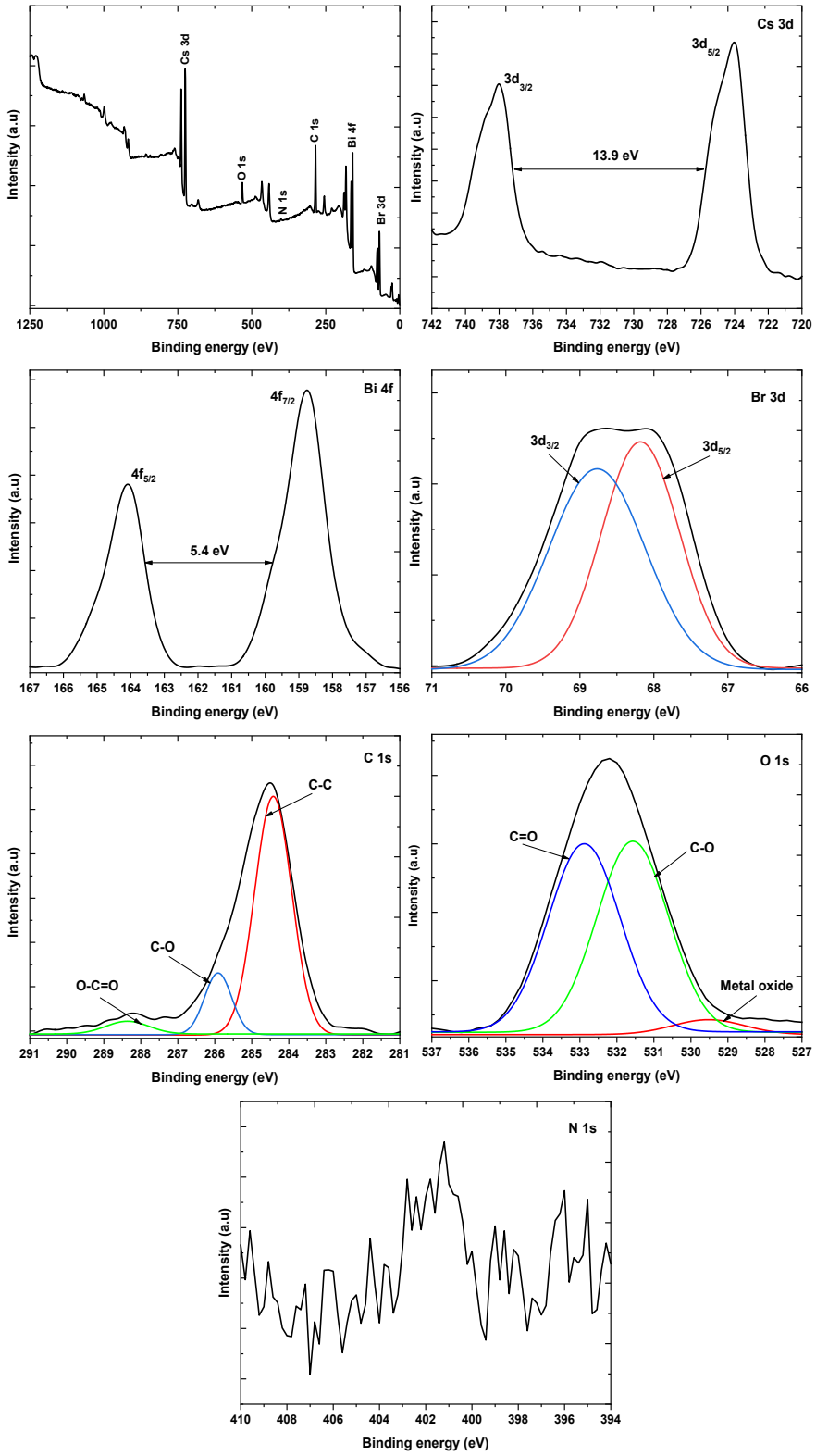

Fig. 4. 9: XPS spectra of $Cs_3Bi_2Br_9$ nanocrystals.

Table 4.1: Summary of the atomic composition and stoichiometric assignments obtained from the fitting of the XPS spectra of $Cs_3Bi_2Br_9$

Element	Peak binding energy (eV)	Atomic %	Assignment	Assignment binding energy (eV)
Cs	724.7	5.5	Cs $3d_{5/2}$	724
			Cs $3d_{3/2}$	738
Bi	158	2.5	Bi $4f_{7/2}$	158.7
			Bi $4f_{5/2}$	164.1
Br	68.4	17.0	Br $3d_{5/2}$	68.2
			Br $3d_{3/2}$	68.8
C	284.7	65.1	C-C	284.6
			C-O	286.1
			O-C=O	288.4
N	401.3	1.4		
O	532.2	8.4	M-O	529
			C-O	531.6
			C=O	533

The presence of capping agents on the surface of the as-synthesized $Cs_3Bi_2Br_9$ NCs was investigated *via* FTIR spectroscopy. The FTIR spectra of the pure OA, OLA and the $Cs_3Bi_2Br_9$ NCs are shown in Fig. 4.10 and the results are summarized in Table 4.3. The OLA and OA show their characteristic bands similar to those discussed in Chapter 3. Similar to the $CsSnBr_3$ NCs, the FTIR spectrum of the $Cs_3Bi_2Br_9$ NCs also show the absence of the C=O stretching vibration. However, the N-H bands of the OLA were significantly present in the $Cs_3Bi_2Br_9$ spectrum which suggests the successful capping of OLA to the NCs surface.

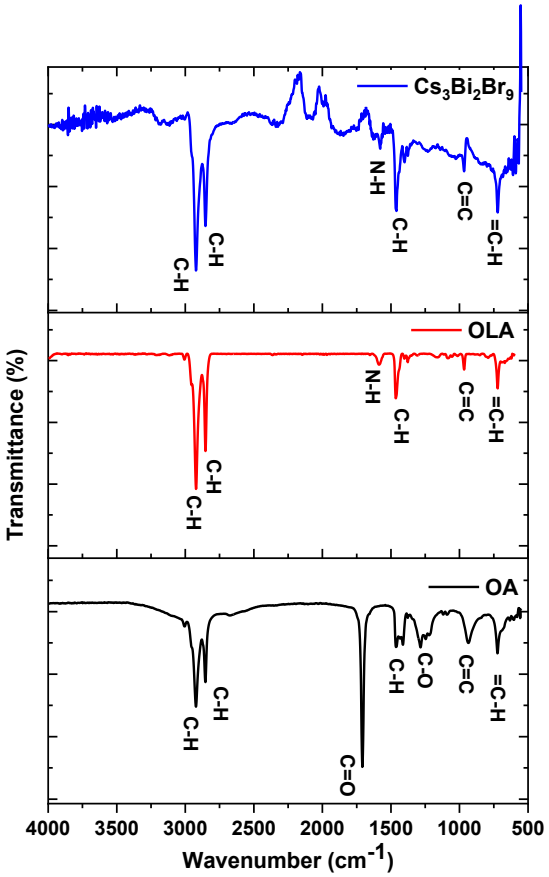

Fig. 4.10: FTIR spectra of OA, OLA and $Cs_3Bi_2Br_9$ nanocrystals.

Table 4.2: FTIR assignments for oleic acid, oleylamine and $Cs_3Bi_2Br_9$ nanocrystals

Assignment	OA	OLA	$Cs_3Bi_2Br_9$
=C-H	715 cm^{-1}	715 cm^{-1}	719 cm^{-1}
C=C	926 cm^{-1}	967 cm^{-1}	974 cm^{-1}
C-H	1467 cm^{-1}, 2845 cm^{-1}, 2923 cm^{-1}	1467 cm^{-1}, 2845 cm^{-1}, 2923 cm^{-1}	1467 cm^{-1}, 2848 cm^{-1}, 2920 cm^{-1}
C-O	1265 cm^{-1}	-	-
C=O	1709 cm^{-1}		
N-H	-	1586 cm^{-1}	1582cm^{-1}

To further confirm the capping of the NCs, NMR spectroscopy was done and the spectra are shown in Fig. 4.11 and 4.12 for the ^{1}H and ^{13}C NMR respectively and the results are summarized in Table 4.3. From the ^{1}H and ^{13}C NMR spectra of OLA and OA, all the protons

and carbons were accounted for. The characteristic $CdCl_3$ peaks for the ^{1}H and ^{13}C NMR are located at 7.26 and 77 ppm respectively.

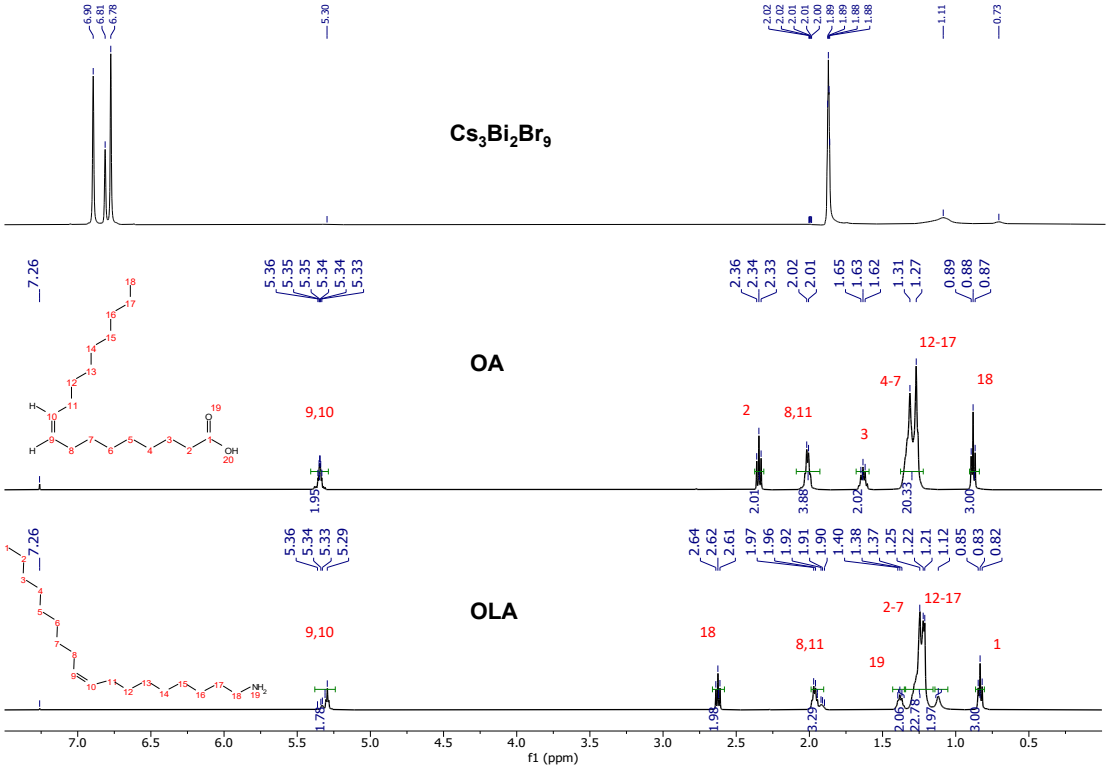

Fig. 4.11: ^{1}H NMR spectra of OLA, OA and $Cs_3Bi_2Br_9$ nanocrystals.

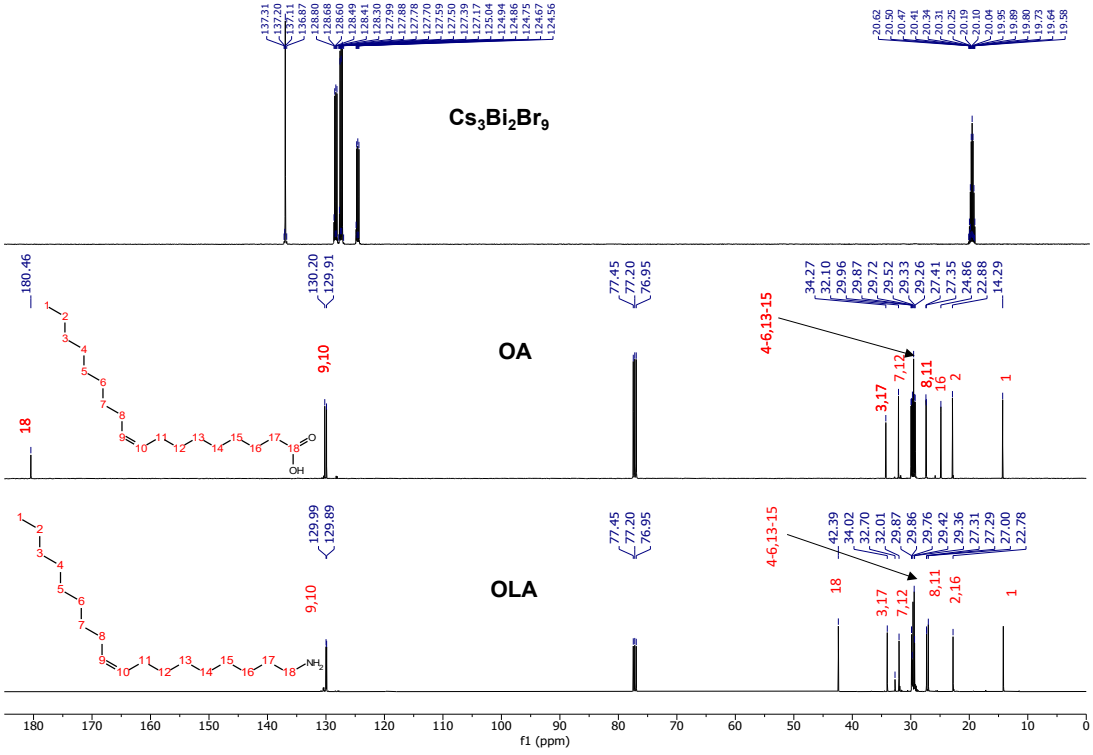

Fig. 4.12: ^{13}C NMR spectra of OLA, OA and $Cs_3Bi_2Br_9$ nanocrystals.

The characteristic peaks for OLA were the NH_2 (1.37-1.40 ppm) and the -CH_2-NH_2 (2.61-2.64) in the ^{1}H NMR spectrum and the -CH_2-NH_2 (42.39) in the ^{13}C NMR spectrum. While for the OA, the -CH_2-C=O (2.33 – 2.36 ppm) chemical shifts in the proton spectrum and C=O (180.46 ppm) chemical shift in the ^{13}C spectrum were the distinguishing bands. The ^{1}H NMR spectrum of the $Cs_3Bi_2Br_9$ NCs showed strong hexane peaks arising from the solvent used to wash and disperse the NCs. The perovskite's ^{1}H NMR spectrum also shows the -CH_2-NH_2 (2.00 – 2.02 ppm) peaks. These peaks suggest that only OLA is capped on the NCs surface. The absence of OA capping was further confirmed from the ^{13}C NMR spectrum of $Cs_3Bi_2Br_9$ NCs where no C=O characteristic peaks of the OA were observed. The NMR results are consistent with the FTIR results where only the N-H bands are observed in the $Cs_3Bi_2Br_9$ spectrum.

Table 4. 3: NMR assignments for oleic acid, oleylamine and $Cs_3Bi_2Br_9$ nanocrystals

Compound	^{1}H NMR (δ ppm)	^{13}C NMR (δ ppm)
OLA	-CH_3 (0.82 – 0.85), -CH_2- (1.12 – 1.25), -CH_2-CH=CH-CH_2- (1.90 – 1.97), -NH_2 (1.37 – 1.40), -CH_2-NH_2 (2.61 – 2.64), CH=CH (5.29 – 5.36)	-CH_3 (22.78), -CH_2- (27.00 – 34.02), -CH_2-NH_2 (42.39), CH=CH (129.91 – 130.20)
OA	-CH_3 (0.87 – 0.89), -CH_2- (1.27 – 2.02), -CH_2-C=O (2.33 – 2.36), CH=CH (5.33 – 5.36)	-CH_3 (14.29), -CH_2- (22.88 – 34.27), CH=CH (129.91 – 130.20), C=O (180.46)
$Cs_3Bi_2Br_9$	CH_3 hexane (0.73), -CH_2 hexane (1.1) , -CH_2 (1.89), -CH_2-NH_2 (2.00 – 2.02), CH=CH (5.33 – 5.36)	-CH_3 (18), -CH_2 hexane (19-58-20.62), CH=CH (127), CH=CH (128.30 – 137.31)

Perovskites are known to be very unstable in ambient conditions which consequently affect their application, therefore, stability studies were performed on the $Cs_3Bi_2Br_9$ NCs. From the XRD pattern in Fig. 4.13, the as-synthesized material showed excellent stability for 21 days with no deviation in the phase of the material as indicated by the lack of deviation in peak positions and absence of secondary peaks. This indicates that the Bi-based perovskite are more stable than the Sn-based perovskite which were only stable for 3 days.

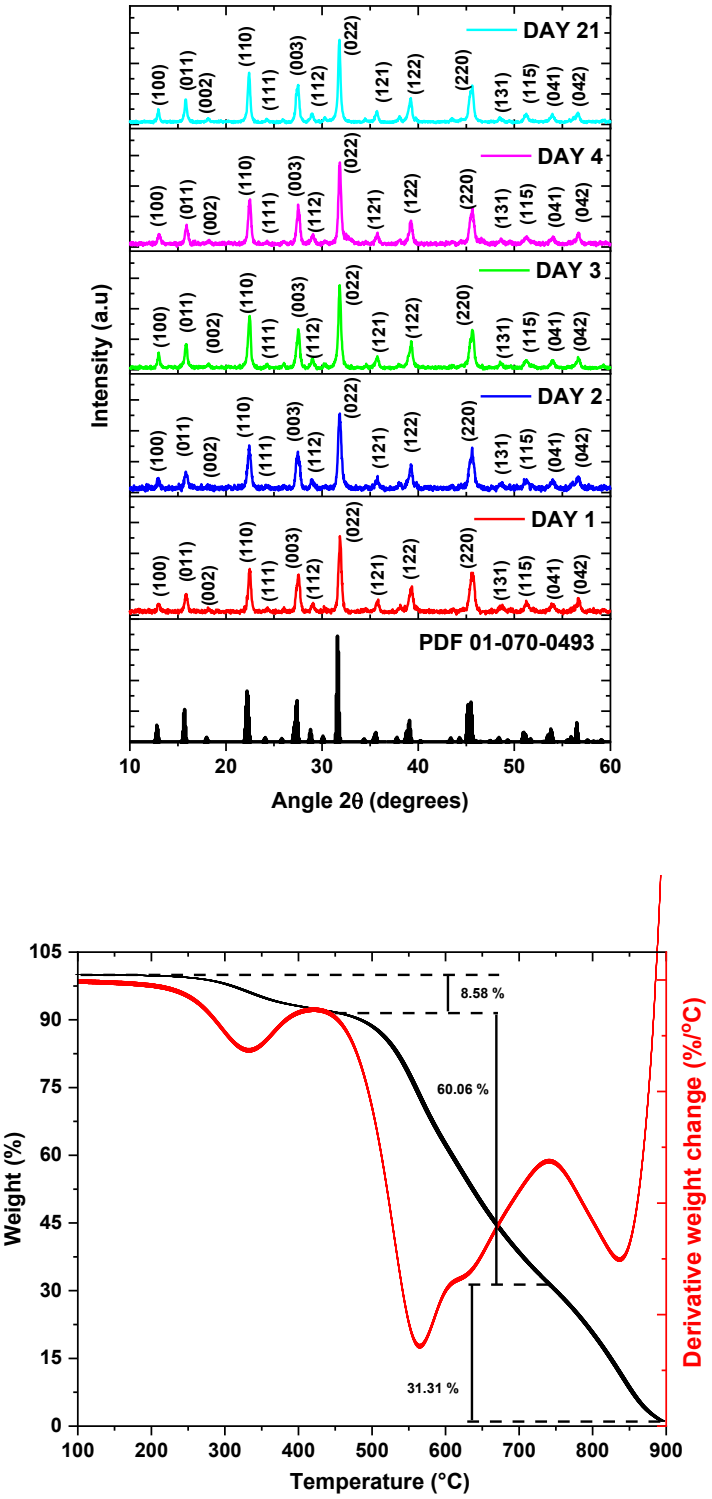

Fig. 4.13: Stability study of $Cs_3Bi_2Br_3$ nanocrystals synthesized at 210 °C for 1 min using XRD and TGA (day 1 sample).

TGA was done to determine the thermal stability of the perovskite NCs. From the TGA graph in Fig. 4.13, the derivative weight curve shows four decomposition peaks of the $Cs_3Bi_2Br_9$ NCs where the maximum temperature for the four decompositions steps are located at 330 °C, 567 °C, 632 °C and 839 °C. The weight percent curve shows that about 8.5% of the perovskite's weight was lost during the first decomposition step; this initial decomposition can be due to loss of moisture and organics in the sample. Furthermore, the second and third decomposition starting at about 455 °C occur simultaneously as revealed by the derivative weight. The concomitant decomposition processes may be due to $BiBr_3$ degradation and CsBr sublimation since $BiBr_3$ has a boiling point of about 461 °C while CsBr sublimes at about 650 °C [5, 15, 16]. Finally, the last decomposition process peak at 839 °C may be attributed to inorganic residual components in the perovskite. The $Cs_3Bi_2Br_9$ NCs showed improve stability over $MA_3Bi_2Br_9$ and this suggests that the inorganic perovskite are better candidates for use in various applications [17].

4.4 Conclusion

The study of colloidal synthesis parameters for $Cs_3Bi_2Br_9$ nanocrystals shows that 1 min and 210 °C were the optimum conditions. The XPS analysis confirmed the composition of $Cs_3Bi_2Br_9$ and the capping agents of the nanocrystals. Further confirmation of the capping agent was done with NMR and FTIR spectroscopy where both spectra conclusively show that only oleylamine was capped to the nanocrystal surface. XRD and TGA studies on the samples proved that the material's stability lasted for 21 days under standard temperature and pressure while the thermal degradation was observed after 250 °C. The stability together with the bandgap energy of the synthesized $Cs_3Bi_2Br_9$ open avenues for specific applications of these materials such as photocatalysis, sensing and electron transfer layer for photovoltaics.

4.5 References

[1] Q. Chen, N. De Marco, Y. (Michael) Yang, T.-B. Song, C.-C. Chen, H. Zhao, Z. Hong, H. Zhou, Y. Yang, *Nano Today* 10 (2015) 355–396.

[2] M. Leng, Z. Chen, Y. Yang, Z. Li, K. Zeng, K. Li, G. Niu, Y. He, Q. Zhou, J. Tang, *Angewandte Chemie International Edition* 55 (2016) 15012–15016.

[3] R. Wang, H. Li, H. Sun, Encyclopedia of Environmental Health (2019) 415–423.

[4] M.P. Kalenga, S. Govindraju, M. Airo, M.J. Moloto, L.M. Sikhwivhilu, N. Moloto, *Journal of Nanoscience and Nanotechnology 15* (2015) 4480-4486.

[5] Y. Dai, H. Tüysüz, *ChemSusChem Communications* 12 (2019) 2587–2592.

[6] M. Leng, Y. Yang, K. Zeng, Z. Chen, Z. Tan, S. Li, J. Li, B. Xu, D. Li, M.P. Hautzinger, Y. Fu, T. Zhai, L. Xu, G. Niu, S. Jin, J. Tang, *Advanced Functional Materials* 28 (2018) 1704446.

[7] S. Ghosh, S. Mukhopadhyay, S. Paul, B. Pradhan, S.K. De, *ACS Applied Nano Materials* 3 (2020) 11107–11117.

[8] M. Roy, S. Ghorui, Bhawna, J. Kangsabanik, R. Yadav, A. Alam, M. Aslam, *The Journal of Physical Chemistry C* 124 (2020) 19484–19491.

[9] M. Zhang, Z.-Q. Tian, D.-L. Zhu, H. He, S.-W. Guo, Z.-L. Chen, D.-W. Pang, *New Journal of Chemistry* 42 (2018) 9496–9500.

[10] Y. Wu, H. Pan, X. Zhou, M. Li, B. Zhou, C. Yang, W.-H. Zhang, J. Jie, C. Li, *Chemical Science* 6 (2015) 4615–4622.

[11] C. Wagner, W. Riggs, L. Davis, J. Moulder, G. Muilenberg, Eden Prairie, MN 38 *Handbook of X-ray Photoelectron Spectroscopy* (1979).

[12] W.E. Morgan, J.R. Van Wazer, W.J. Stec, *Journal of American Chemical Society* 95 (1973) 751–755.

[13] J.-C. Dupin, D. Gonbeau, P. Vinatier, A. Levasseur, *Physical Chemistry Chemical Physics* 2 (2000) 1319–1324.

[14] S. Hoste, D.F. Van De Vondel, G.P. Van Der Kelen, *Journal of Electron Spectroscopy and Related Phenomena* 17 (1979) 191–195.

[15] M. Kulbak, S. Gupta, N. Kedem, I. Levine, T. Bendikov, G. Hodes, D. Cahen, *The Journal of Physical Chemistry Letters* 7 (2016) 167–172.

[16] A. Murata, T. Nishimura, H. Shimizu, Y. Shiratori, T. Kato, R. Ishikawa, S. Miyajima, *AIP Advances* 10 (2020) 045031.

[17] J. Luo, M. Hu, G. Niu, J. Tang, *ACS Applied Materials and Interfaces* 11 (2019) 31575–31584.

CHAPTER 5

The effect of temperature and time on the synthesis of 2D Cs_2ZnBr_4 perovskite nanocrystals

5.1 Introduction

Since the high efficiencies observed in hybrid perovskite solar cells, these solar cells and materials have remained at the forefront of research. However, hampering the progress of these solar cells has been the stability of these materials [1]. This has perpetuated new efforts into the research of alternative perovskite materials that can achieve similar efficiencies while being stable over long periods. Among the most studied are the Cs based hybrid perovskite nanocrystals due to the optimum ionic radius of Cs and its stability [2]. In an effort to further improve the properties of Cs based nanocrystals, studies that vary the B cation and the halides have been undertaken. $CsPbI_3$ under optimized conditions has recently obtained 21.31% efficiency [3]. While the use of lead has led to great efficiencies, its toxicity has come under major scrutiny. This has led to the exploration of other B cations. Zinc is an element which can play a role in the composition and properties of Cs-based perovskite nanocrystals (NCs). Unlike Pb, Zn is an essential element required for the proper physiological functioning of the human body, as such, it is less toxic [4]. Hence, the B cation in ABX_3 structure can be replaced by Zn instead of using Pb. The exploration of Zn as a potential substitute for Pb was further informed by earlier studies on Zn incorporation into perovskites. For instance, all-inorganic $CsPbIBr_2$ was doped with $ZnBr_2$, the doped perovskite showed improved stability and crystallinity where just 1% $ZnBr_2$ doping improved the power conversion efficiency (PCE) of the device by 34% [5]. Also, the $CsPb_{0.99}Zn_{0.01}IBr_2$ device showed superior long-term stability in ambient conditions and against heat.

2D hybrid perovskites (so-called Ruddlesden–Popper) unlike traditional perovskites such as $CaTiO_3$ that take on the ABX_3 formula with A having an oxidation state +2, B +4, and X -2, have been shown to take on varied oxidation states. 2D hybrid perovskites have become promising semiconductors due to their high degree of structural flexibility and tunable optoelectronic properties [6]. They have a general formula of $A_{n+1}B_nX_{3n+1}$, where A = Cs^+, $CH_3NH_3^+$ (MA), $HC(NH_2)_2^+$ (FA), B = Ge^{2+}, Sn^{2+}, Pb^{2+} and X = Cl^-, Br^-, I^- and n can be n = 1, 2, 3, 4, 5 [7–10]. 2D hybrid perovskites are generally synthesized from the bottom-up self-

assembly of individual, semiconducting perovskite sheets having an adjustable slab thickness of up to a few nanometers [11]. Only until recently has B = Zn^{2+} been investigated following the structural determination in 1959 [12].

5.2 Experimental procedures

5.2.1 Chemicals

The same chemicals used in Chapter 3 were used including zinc bromide ($ZnBr_2$, 99%) which was obtained from Sigma-Aldrich and used without further purification.

5.2.2 Synthesis of Cs_2ZnBr_4 nanocrystals

The same procedure in Chapter 3 was followed here, except that $ZnBr_2$ was the metal precursor.

5.2.3 Characterization techniques

The same characterization techniques were used as in Chapter 3.

5.3 Results and discussion

5.3.1 Effect of temperature on Cs_2ZnBr_4 nanocrystals

Powder X-ray diffraction was used to determine the crystal phases of the resultant nanocrystals and for the detection of any impurities. Shown in Fig. 5.1 are the XRD patterns of the nanocrystals synthesized at different temperatures and the reference pattern of Cs_2ZnBr_4. The peaks in the XRD patterns of the synthesized materials were all assigned to the reference peaks indicating phase purity in Cs_2ZnBr_4. The Cs_2ZnBr_4 NCs crystallized in the orthorhombic phase with a reference card number PDF 01-088-2355 and lattice parameters: a = 10.202 Å, b = 7.738 Å, and c = 13.5390 Å. The space group of the synthesized nanocrystals was Pnma (62), indicating that the nanocrystals belonged to the D_{2h} point group [16]. The increase in peak intensity as the temperature increased was indicative of an increase in crystallinity of the nanocrystals.

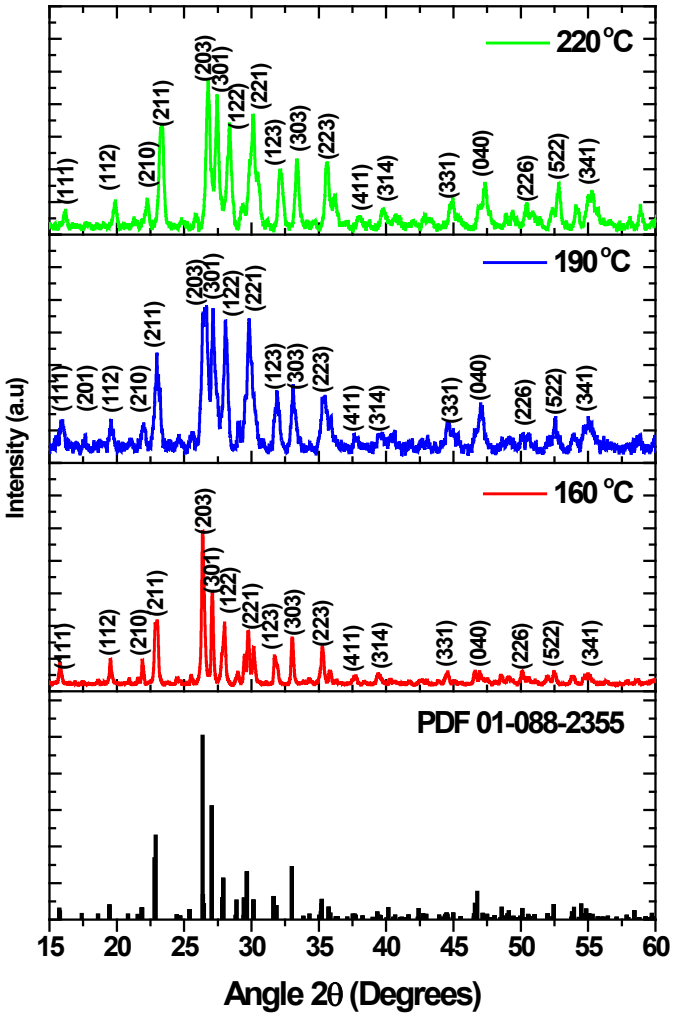

Fig. 5.1: XRD patterns of Cs_2ZnBr_4 nanocrystals synthesized at different temperatures.

TEM was then used to determine the morphology of the particles as the temperature was increased from 160 °C to 220 °C. As evident from the images in Fig. 5.2, there was an increase in the size of the nanocrystals with increasing reaction temperature from an average aspect ratio of 2 ± 0.9 nm to 3 ± 2 nm for 160 °C and 190 °C respectively. However, the aspect ratio was reduced to 2.5 ± 2 nm at 220 °C. Small nanorods with average lengths of 30.8 nm and widths of 17.6 nm were produced at 160 °C reaction temperature while bigger nanorods with average lengths of 138.7 nm and width of 48.4 nm were produced at 190 °C. The reduction in the aspect ratio observed at the higher temperature (beyond 200 °C) was due to the widening of the nanocrystals. From 160 °C to 190 °C, there was preferential growth in the lengths of the nanocrystals but at 220 °C, growth along the widths of the nanocrystals was preferred. The

nanorods at 160 °C were comparatively smaller and more monodispersed since, at a much lower temperature, the ligands are more strongly bonded to the nanocrystals thus influencing their growth as compared to the nanocrystals synthesized at higher temperatures where thermal agitation weakens the surfactant binding to the nanocrystals [17].

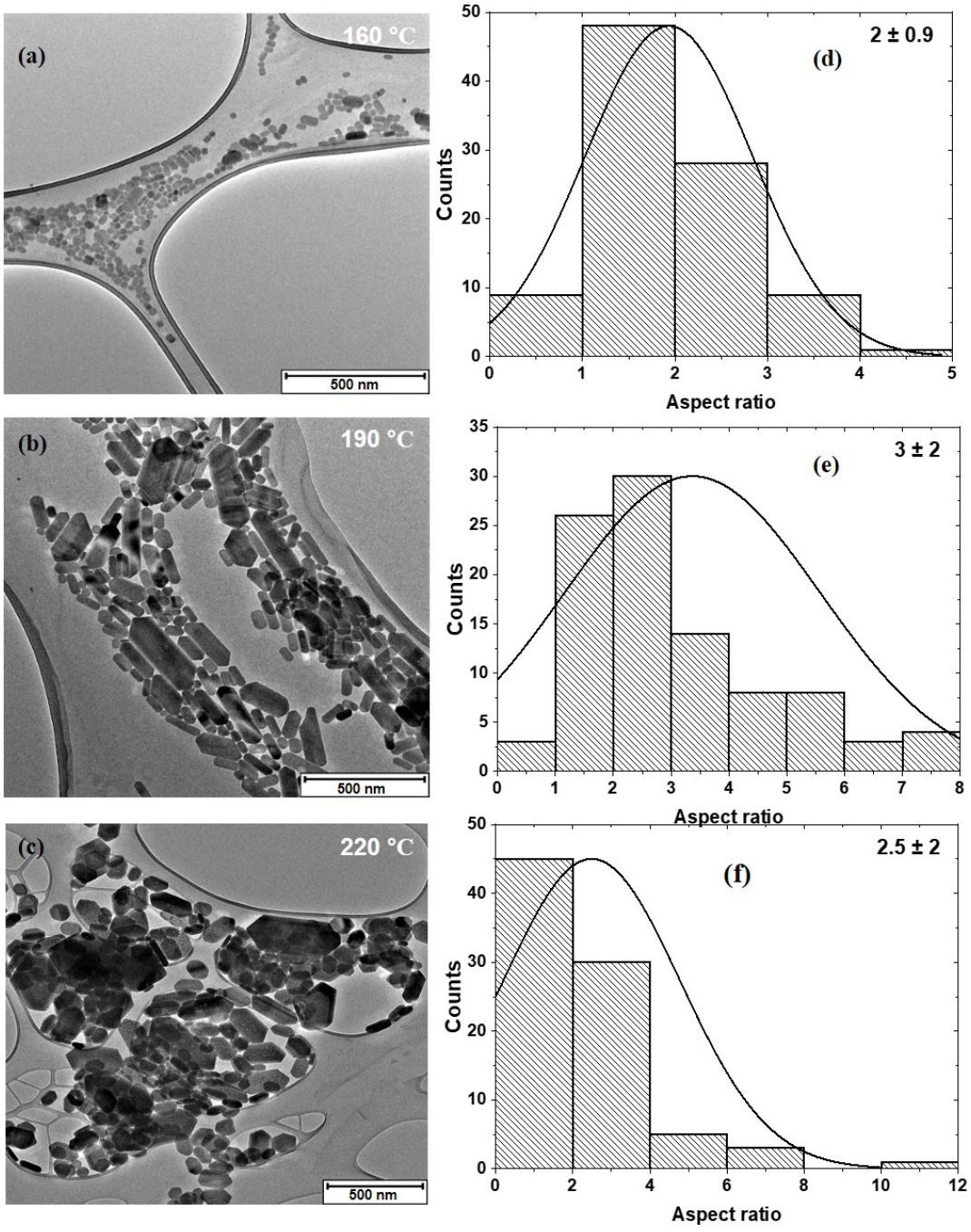

Fig. 5.2: (a-c) TEM images and (d-f) corresponding size distribution of Cs_2ZnBr_4 nanocrystals synthesized at different temperatures.

The optical properties of a material are crucial in optoelectronic applications. It has been shown that size, shape, and dispersity of nanocrystals can influence the optical properties, as a result of the quantum confinement effects and the density of states in nanocrystals [18, 19].

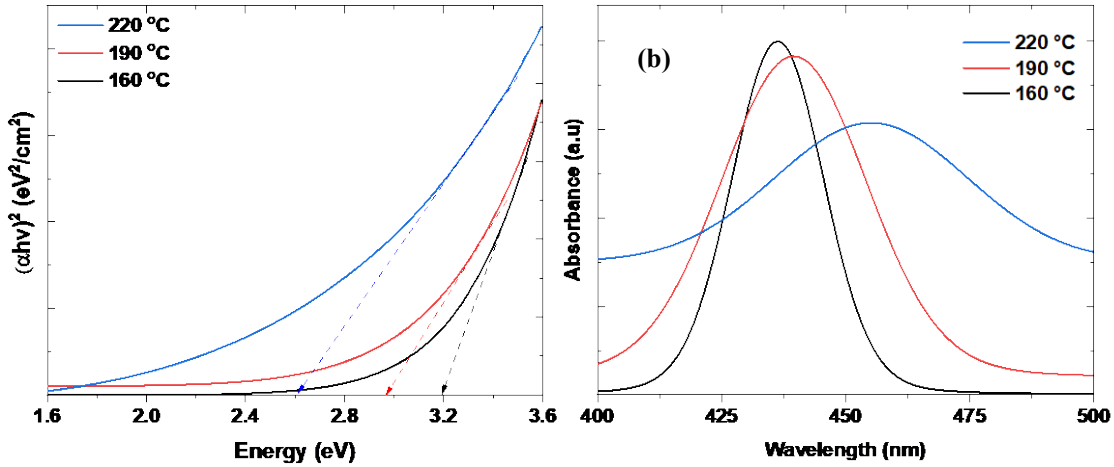

Fig. 5.3: (a) Tauc plot and (b) photoluminescence spectra of Cs_2ZnBr_4 nanocrystals synthesized at different temperatures.

The optical properties of Cs_2ZnBr_4 nanocrystals synthesized at different temperatures were studied using UV-vis absorption and photoluminescence spectroscopy and the results are depicted in Fig. 5.3. From the Tauc plots, a decrease in band-gap was observed as the temperature was increased from 3.18 eV, 2.96 eV to 2.60 eV for 160 °C, 190 °C, and 220 °C, respectively. This was attributed to an increase in particle sizes due to Ostwald ripening effects brought about by the increase in temperature [20]. The photoluminescence spectrum is typically red-shifted from the UV-vis absorption spectrum due to radiative losses and other defects. The emission maxima for particles synthesized at 160 °C, 190 °C and 220 °C were 436 nm (2.84 eV), 439 nm (2.82 eV) and 455 nm (2.73 eV), respectively.

5.3.2 Effect of reaction time on Cs_2ZnBr_4 nanocrystals.

The effect of time on the properties of nanocrystals has been well studied [18, 19]. However, to our knowledge, no work has been reported on the effect of time on the properties of Cs_2ZnBr_4 nanocrystals. Shown in Fig. 5.4 are the XRD patterns of Cs_2ZnBr_4 synthesized at different times.

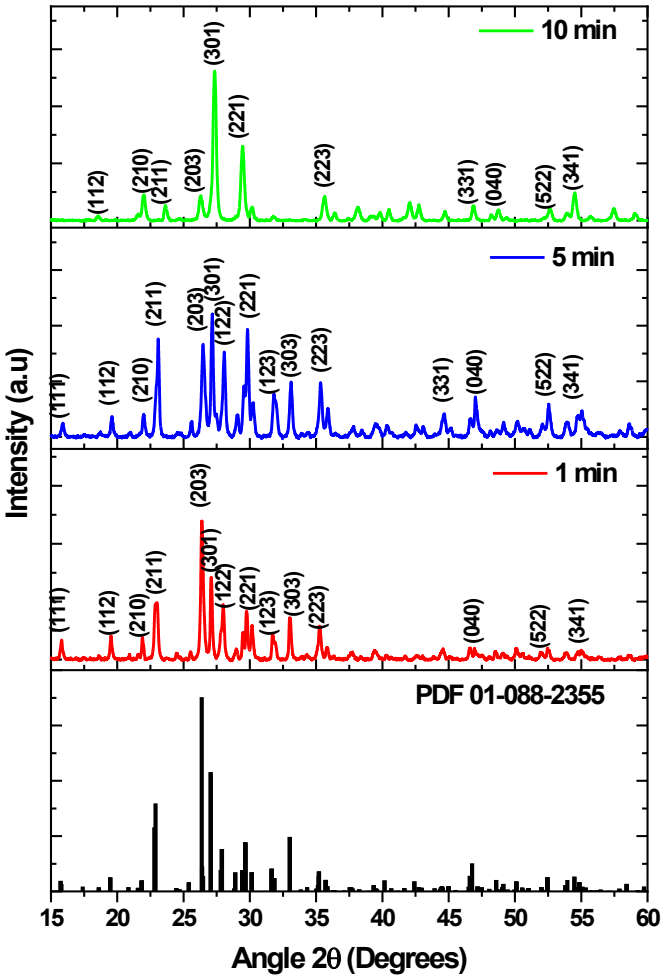

Fig. 5.4: XRD patterns of Cs_2ZnBr_4 nanocrystals synthesized at different times.

The nanocrystals form rapidly within 1 min as indicated by XRD pattern, which shows that all the peaks were indexed to orthorhombic Cs_2ZnBr_4 (PDF 01-088-2355). As the time was prolonged to 5 min, no changes in the crystal structure were observed. However, extending time further (10 min) resulted in the formation of Cs_3ZnBr_5 (PDF 00-066-0032) binary metal halide. The morphology and size of Cs_2ZnBr_4 nanocrystals changed drastically with increasing time. As shown in the TEM images in Fig. 5.5, an obvious increase in the size of the nanocrystals was observed with increasing reaction time.

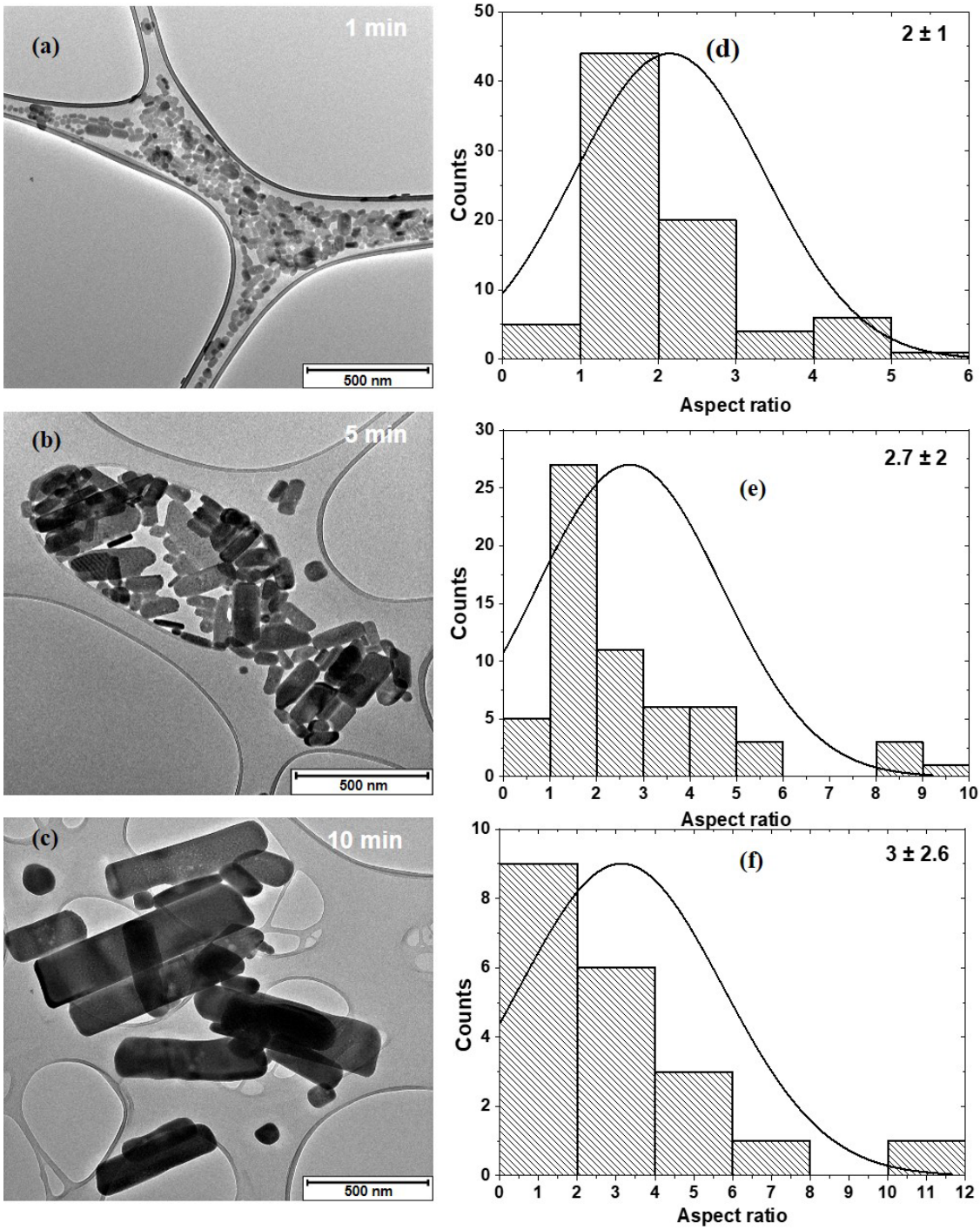

Fig. 5.5: (a-c) TEM images and (d-f) corresponding size distribution of Cs_2ZnBr_4 nanocrystals synthesized at different times.

Smaller nanorods with an aspect ratio of (average length of 38 nm and a width of 22 nm) were produced at 1 min reaction time and this increased to an aspect ratio of 2.7 ± 2 nm at 5 min reaction time. Bigger rods with an aspect ratio of 3 ± 2.6 nm (average length of 366 nm and a width of 131 nm) were produced at 10 min reaction time. This continuous growth in

nanocrystal size was due to the Ostwald ripening effect whereby larger particles are formed at the expense of small ones since the smaller ones are more soluble than larger ones [17]. Therefore, as time progresses in the synthesis of Cs_2ZnBr_4, the smaller particles diffuse and deposit on the larger particles.

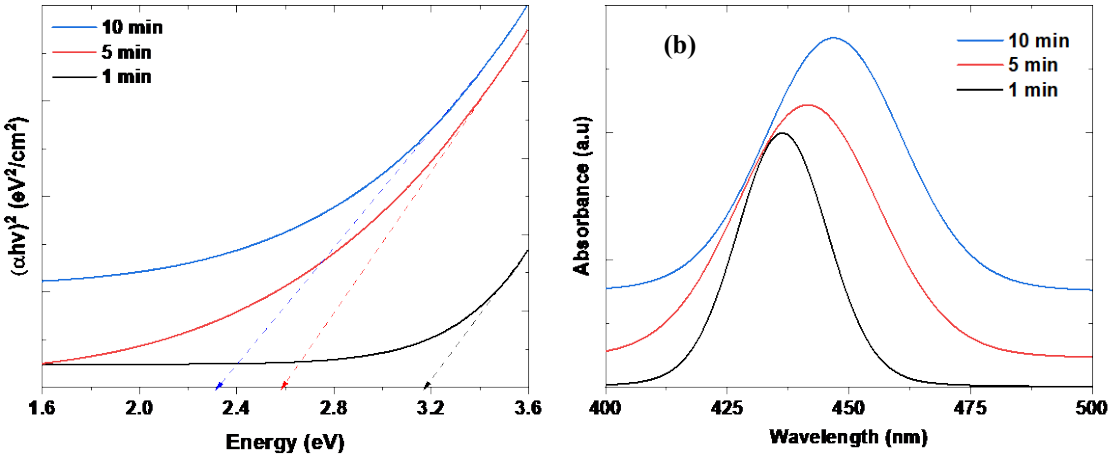

Fig. 5.6: (a) Tauc plot and (b) photoluminescence spectra of Cs_2ZnBr_4 nanocrystals synthesized at different times.

The optical properties of Cs_2ZnBr_4 synthesized at different times are depicted in Fig. 5.6. The 1 min sample had a bandgap of 3.18 eV; this is the same as in Fig. 5.3 as the reaction conditions were the same. As time was increased to 5 min and 10 min, there was a decrease in bandgap, consistent with an increase in particle size. The bandgaps were 2.60 eV (476 nm), 2.32 eV (534 nm) for the 5 min and 10 min samples respectively. The photoluminescence spectra showed a red-shift in the wavelength as the time was increased. At 1 min, the emission peak was at 436 nm while at 5 and 10 min, the emission peaks were observed at 441 nm and 447 nm respectively.

The electrochemical measurements of Cs_2ZnBr_4 NCs were done to estimate band edges of electroactive species in the solution phase at ambient conditions. As shown in Fig. 5.7, the cyclic voltammogram of Cs_2ZnBr_4 NCs dispersion show the oxidation and reduction peaks of the NCs which can be attributed to the valence band and conduction band of Cs_2ZnBr_4 respectively. The peak at +1.68 and -1.34 corresponds to the oxidation and reduction peaks respectively. From this measurement, the E_{bg} is 3.02 eV which is close to the optical bandgap

(3.18 eV). The valence band and conduction band levels of the Cs_2ZnBr_4 NCs were determined to be -6.18 eV and -3.16 eV respectively.

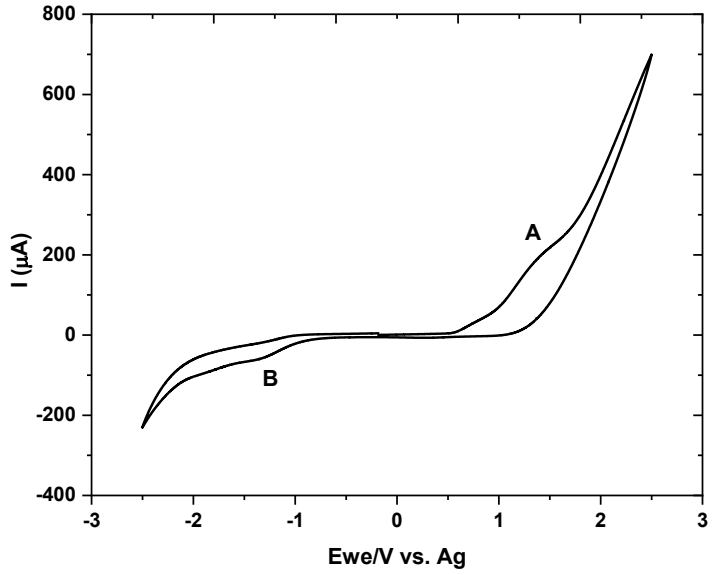

Fig. 5.7: Cyclic voltammogram of Cs_2ZnBr_4 nanocrystals.

Raman spectroscopy was used to further confirm the formation of Cs_2ZnBr_4 nanomaterial. The Raman spectrum of the as-synthesized material shown in Fig. 5.8 shows a very strong peak at 178 cm^{-1} which is the characteristic A_g mode of cesium zinc halides and it is due to the Zn-Br stretch motions [21].

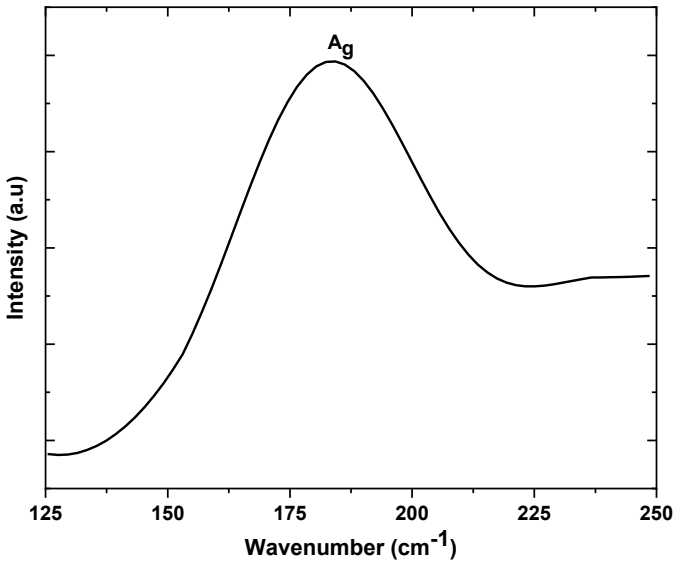

Fig. 5.8: Raman spectrum of Cs_2ZnBr_4 nanocrystals.

The surface of the nanocrystals is thought to be capped with a layer of surfactant molecules and in this case oleic acid and oleylamine. This is a common assumption in the colloidal synthesis of nanocrystals. The broad survey XPS spectrum of the capped Cs_2ZnBr_4 synthesized at 160 °C for 1 min along with the spectra of the constituent elements are shown in Fig. 5.9. These were consistent with OA/OLA capped Cs_2ZnBr_4. The C 1s spectrum was deconvoluted to three peaks. The presence of the C-C was to be expected and was attributed to the long alkyl-chains of the capping agents. The C-O at 286 eV and O-C=O at 288.4 eV were indicative of the OA capping however it must be noted that the capping agent is prone to oxidation [22]. The N 1s and O 1s high-resolution spectra were low in intensity as such no additional information from this technique could be deducted about the nature of the capping. The atomic composition for both N and O were 3.3% and 3.9% respectively as shown in Table 5.1. The Cs 3d high-resolution spectrum showed two peaks at 725.8 eV and 739.9 eV corresponding to $3d_{5/2}$ and $3d_{3/2}$ of Cs^+. The Zn 2p high-resolution spectrum showed two peaks at 1025.2 eV and 1048.4 eV corresponding to $2p_{3/2}$ and $2p_{1/2}$ respectively. This is as a result of Zn^{+2} species being present. The high-resolution Br 3d spectrum was deconvoluted into three peaks at 69.0 eV ($3d_{5/2}$), 69.4 eV, and 69.8 eV ($3d_{3/2}$) where the peaks at 69.0 eV and 69.8 eV were due to the $ZnBr_2$ bonding in the material [23] while the deconvoluted peak at 69.4 eV was due to the Cs-Br bonding [25]. The percentage compositions of the present species are shown in Table 5.1.

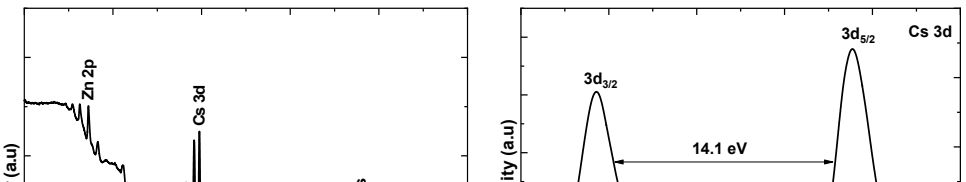

Fig. 5.9: XPS high-resolution spectra of capped Cs_2ZnBr_4 nanocrystals synthesized at 160 °C for 1 min.

Table 5.1: Summary of the atomic composition and stoichiometric assignments obtained from the fitting of the XPS spectra of Cs_2ZnBr_4

Element	Peak binding energy (eV)	Atomic %	Assignment	Assignment binding energy (eV)
Br	69.0	16.1	Br $3d_{5/2}$	69.0
			CsBr	69.4
			Br $3d_{3/2}$	69.8
C	284.9	65.3	C-C	284.4
			C-O	286.0
			O-C=O	288.4
N	401.6	3.3	-	-
O	532.4	3.9	-	-
Cs	725.8	6.4	Cs $3d_{5/2}$	725.9
			Cs $3d_{3/2}$	739.7
Zn	1026.0	5.0	Zn $2p_{3/2}$	1025.2
			Zn $2p_{1/2}$	1048.4

To further study the nature of the interaction of the capping molecules with the nanocrystals, FTIR and NMR spectroscopies were undertaken. The FTIR spectra are shown in Fig. 5.10 and the results are summarized in Table 5.2. The OA spectrum showed all the expected bands with the significant bands C-O and C=O found at 1265 cm^{-1} and 1709 cm^{-1}, respectively. Cs_2ZnBr_4 nanocrystals are thought to be capped by both OA and OLA. From the FTIR results, no C-O or C=O bands were observed in the Cs_2ZnBr_4 spectrum. The OLA spectrum showed all the C-H and C=C bands and a weak N-H band at 1586 cm^{-1}. The N-H bands were significantly present in the Cs_2ZnBr_4 spectrum thereby suggesting that OLA was indeed capping the particles. The absence of the C=O band suggested that OA was not capping the nanocrystals. FTIR spectroscopy while it is a useful technique it is however not conclusive hence NMR analysis was conducted.

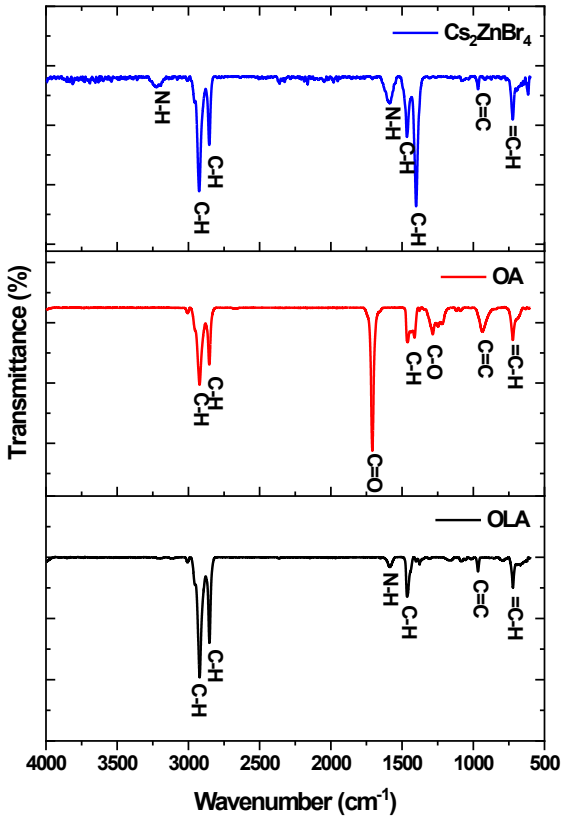

Fig. 5.10: FTIR spectra of OA, OLA and Cs_2ZnBr_4 nanocrystals.

Table 5.2: FTIR assignments for oleic acid, oleylamine and Cs_2ZnBr_4 nanocrystals

Assignment	OLA	OA	Cs_2ZnBr_4
=C-H	715 cm^{-1}	715 cm^{-1}	715 cm^{-1}
C=C	958 cm^{-1}	926 cm^{-1}	974 cm^{-1},
C-H	1467 cm^{-1}, 2837 cm^{-1}, 2923 cm^{-1}	1467 cm^{-1}, 2837 cm^{-1}, 2923 cm^{-1}	1379 cm^{-1}, 1477 cm^{-1}, 2837 cm^{-1}, 2935 cm^{-1}
C-O	-	1265 cm^{-1}	-
C=O		1709 cm^{-1}	
N-H	1586 cm^{-1}	-	1580 cm^{-1}, 3225 cm^{-1}

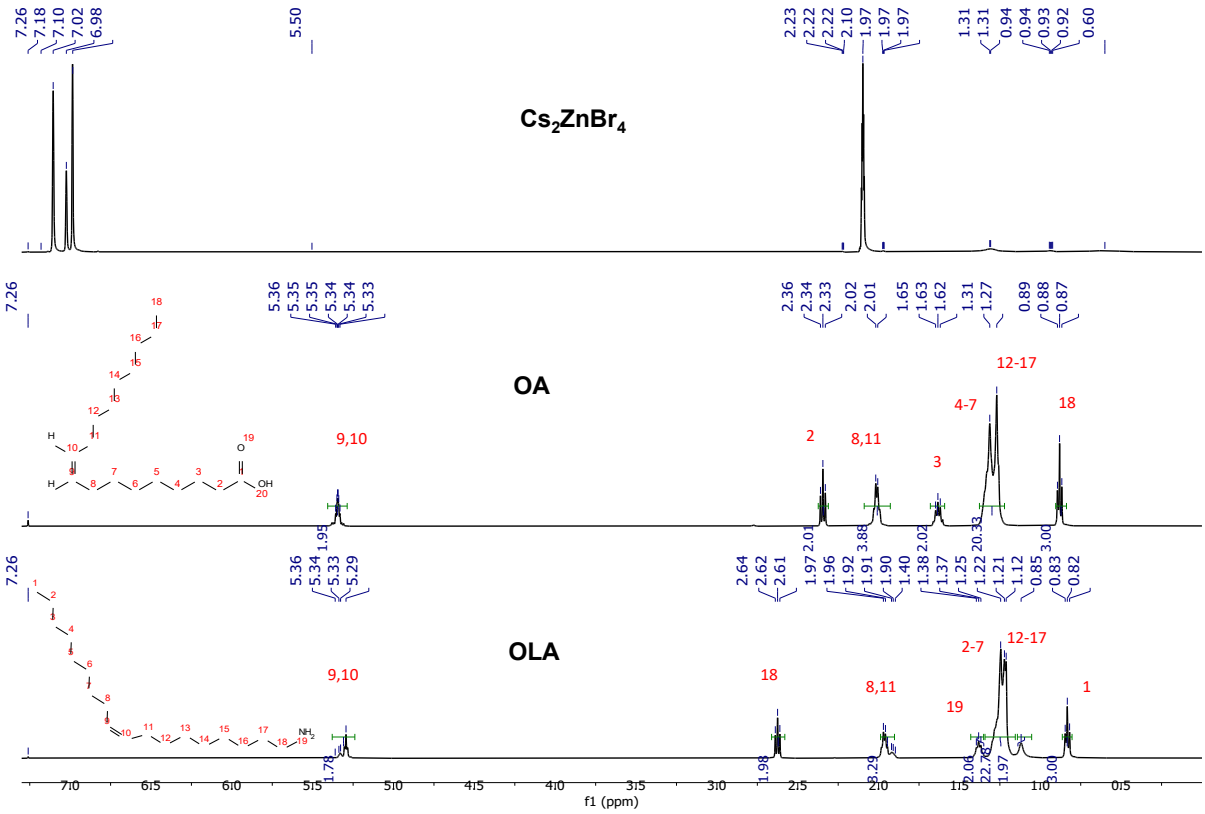

Fig. 5.11: ^{1}H NMR spectra of OLA, OA and the capped Cs_2ZnBr_4 nanocrystals.

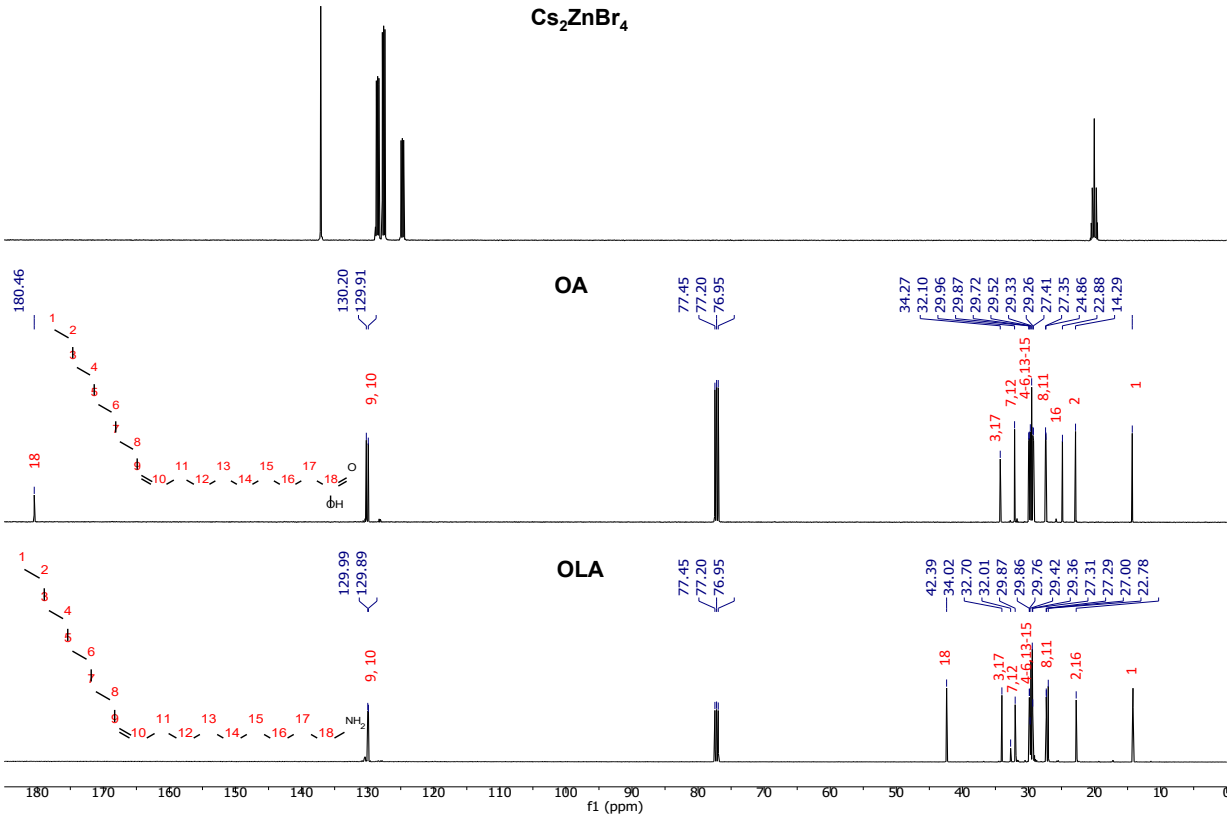

Fig. 5.12: ^{13}C NMR spectra of OLA, OA and the capped Cs_2ZnBr_4 nanocrystal.

The ^{1}H and ^{13}C NMR spectra are shown in Fig. 5.11 and 5.12 respectively and the results are summarized in Table 5.3. From the ^{1}H NMR and ^{13}C NMR, all protons and carbons were accounted for in the OLA ($CH_3(CH_2)_7CH=CH(CH_2)_7CH_2NH_2$ and OA ($CH_3(CH_2)_7CH=CH(CH_2)_7COOH$) spectra. The distinguishing peaks for OLA were the -NH_2 (1.37 – 1.40 ppm) and the -CH_2-NH_2 (2.61 – 2.64 ppm) chemical shifts in the proton spectrum and -CH_2-NH_2 (42.39 ppm) in the carbon spectrum. Contrary, for the OA, the -CH_2-C=O (2.33 – 2.36 ppm) chemical shifts in the proton spectrum and C=O (180.46 ppm) chemical shift in the carbon spectrum were the differentiating bands.

Table 5. 3: NMR assignments for oleic acid, oleylamine and Cs_2ZnBr_4 nanocrystals

Compound	^{1}H NMR (δ ppm)	^{13}C NMR (δ ppm)
OLA	-CH_3 (0.82 – 0.85), -CH_2- (1.12 – 1.25), -CH_2-CH=CH-CH_2- (1.90 – 1.97), -NH_2 (1.37 – 1.40), -CH_2-NH_2 (2.61 – 2.64), CH=CH (5.33 – 5.36)	-CH_3 (22.78), -CH_2- (27.00 – 34.02), -CH_2-NH_2 (42.39), CH=CH (129.91 – 130.20)

OA	-CH_3 (0.87 – 0.89), -CH_2- (1.27 – 2.02), -CH_2-C=O (2.33 – 2.36), CH=CH (5.33 – 5.36)	-CH_3 (14.29), -CH_2- (22.88 – 34.27), CH=CH (129.91 – 130.20), C=O (180.46)
Cs_2ZnBr_4	-CH_3 (0.92 – 0.94), -CH_2 (1.97), CH_3 toluene (2.10), -CH_2-NH_2 (2.22 – 2.23), CH=CH (5.50), CH toluene (6.98 – 7.18)	-CH_3 (18), CH toluene (122.5 & 125.5), CH=CH (127), C toluene (137)

In the ^{1}H NMR spectrum of Cs_2ZnBr_4 nanocrystals, strong toluene peaks were observed and these were impurities from the solvent used to wash and disperse the nanocrystals. Also observed were the triplet –CH_2 peaks at 1.97 ppm associated with the methylene protons adjacent to the ethylene protons (-CH_2-CH=CH-CH_2-) and the ethylene chemical shift at 5.50 ppm. However more telling were the -CH_2-NH_2 (2.22 – 2.23 ppm) peaks, these peaks suggest that only OLA was capping the nanocrystals. Even when examining the ^{13}C NMR spectrum, no C=O peaks were observed, further suggesting that only OLA was capping the nanocrystals. This observation is consistent with the FTIR results where only the N-H bands were observed in the Cs_2ZnBr_4 spectrum in Fig 5.10. It is not completely unexpected that OLA will bind to the nanocrystals solely as amines are better nucleophiles than acids [22]. This further suggests that the O observed in the XPS was from the surface oxidation of the OLA. Surface oxidation of a capping agent is readily observed in capped nanocrystals [22]. The nature of the surface of the nanocrystals especially for perovskite nanocrystals is important for mainly two reasons; (1) the capping agent is known to stabilize nanocrystals, a property that is much sort after in perovskite nanocrystals and (2) the surface affects the reactivity hence properties and applicability of nanocrystals.

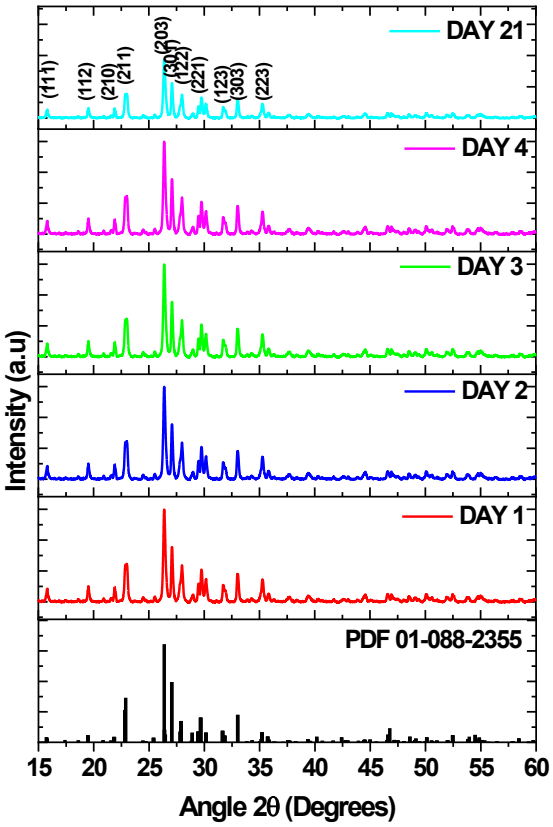

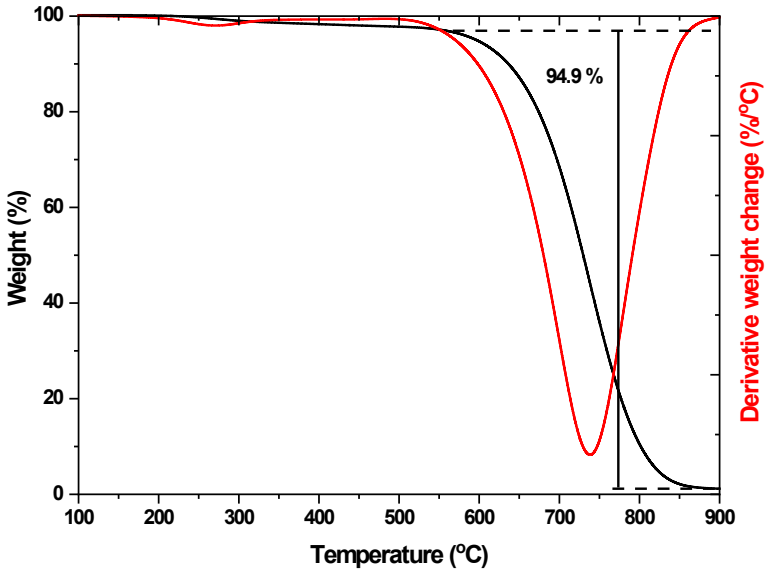

Fig. 5.13: Stability study of Cs_2ZnBr_4 nanocrystals synthesized at 160 °C for 1 min using XRD and TGA (day 1 sample).

Before the application of the nanocrystals, stability studies were done. The particles were stored at room temperature in a cool, dry cabinet prior to analysis. From the XRD studies, the crystal structure and phase did not change for 21 days and no decomposition products were detected. In comparison, the model $CsPbBr_3$ has been shown to lose its properties over a matter of hours [25]. In addition to structural stability, TGA was done to establish the thermal stability. The particles were stable until 260 °C where a slight degradation was observed in the TGA spectrum and this is attributed to the decomposition of the moisture and organics in the sample. Thereafter, the NCs were thermally stable up to 560 °C where the second degradation process started. This second degradation peaked at 735 °C and is attributed to the sublimation of CsBr in the sample [26]. The stability suggests that 2D hybrid perovskite are better candidates for use in various applications.

5.4 Conclusion

Herein we investigate the synthesis of Cs_2ZnBr_4 using the colloidal method. Furthermore, we investigate the effect of changing the reaction temperature and time on the properties of Cs_2ZnBr_4. The variation of temperature and time in the colloidal synthesis follows the Lamer and Dinegar mechanism [13]. An increase in temperature and time promotes the growth of the nuclei through Ostwald ripening. Apart from size, the temperature has been shown to also greatly affect the morphology, crystal structure, and phase of the nanocrystals [14, 15].

The synthesis conditions were optimized to 160 °C and 1 min. The surface chemistry of the optimum sample was studied using XPS, FTIR, and NMR spectroscopies. The XRD and XPS studies confirmed the crystalline structure and the composition of Cs_2ZnBr_4 and the capping of the nanocrystals. The C 1s high-resolution spectrum show oxygenated carbon species which was not conclusive whether these were from the oleic acid or the oxidation of the surface. However, from the FTIR and NMR spectroscopies, oleylamine was confirmed as the only ligand capping the nanocrystals. The role of oleic acid was therefore limited to forming a more robust cesium oleate precursor. The structure of the synthesized materials remained unchanged for 25 days at room temperature, indicating good stability while the Cs_2ZnBr_4 NCs only started decomposing after 560 °C.

5.5 References

[1] D. Wang, M. Wright, N.K. Elumalai, A. Uddin, *Solar Energy Materials and Solar Cells* 147 (2016) 255–275.

[2] J.Y. Woo, Y. Kim, J. Bae, T.G. Kim, J.W. Kim, D.C. Lee, S. Jeong, *Chemistry of Materials* 29 (2017) 7088–7092.

[3] G.E. Eperon, G.M. Paternò, R.J. Sutton, A. Zampetti, A.A. Haghighirad, F. Cacialli, H.J. Snaith, *Journal of Materials Chemistry A* 3 (2015) 19688–19695.

[4] A.S. Prasad, *Advances in Nutrition* 4 (2013) 176–190.

[5] Y. Long, C. Wang, X. Liu, J. Wang, S. Fu, J. Zhang, Z. Hu, Y. Zhu, *Journal of Materials Chemistry C* 9 (2021) 2145–2155.

[6] L. Mao, S.M.L. Teicher, C.C. Stoumpos, R.M. Kennard, R.A. DeCrescent, G. Wu, J.A. Schuller, M.L. Chabinyc, A.K. Cheetham, R. Seshadri, *Journal of American Chemical Society* 141 (2019) 19099–19109.

[7] C.C. Stoumpos, M.G. Kanatzidis, *Accounts of Chemical Research* 48 (2015) 2791–2802.

[8] C.C. Stoumpos, C.D. Malliakas, M.G. Kanatzidis, *Inorganic Chemistry* 52 (2013) 9019–9038.

[9] L. Protesescu, S. Yakunin, M.I. Bodnarchuk, F. Krieg, R. Caputo, C.H. Hendon, R.X. Yang, A. Walsh, M.V. Kovalenko, *Nano Letters* 15 (2015) 3692–3696.

[10] Y. Bekenstein, B.A. Koscher, S.W. Eaton, P. Yang, A.P. Alivisatos, *Journal of the American Chemical Society* 137 (2015) 16008–16011.

[11] H. Tsai, W. Nie, J.-C. Blancon, C.C. Stoumpos, R. Asadpour, B. Harutyunyan, A.J. Neukirch, R. Verduzco, J.J. Crochet, S. Tretiak, *Nature* 536 (2016) 312–316.

[12] B. Morosin, E.C. Lingafelter, *Acta Crystallographica* 12 (1959) 744–745.

[13] V.K. LaMer, R.H. Dinegar, *Journal of the American Chemical Society* 72 (1950) 4847–4854.

[14] L.F.E. Machogo, P. Tetyana, R. Sithole, S.S. Gqoba, N. Phao, M. Airo, P.M. Shumbula, M.J. Moloto, N. Moloto, *Applied Surface Science* 456 (2018) 973–979.

[15] N. Moloto, M.J. Moloto, N.J. Coville, S. Sinha Ray, *Journal of Crystal Growth* 311 (2009) 3924–3932.

[16] A.A. Belik, S.Y. Stefanovich, B.I. Lazoryak, E. Takayama-Muromachi, *Chemistry of Materials* 18 (2006) 1964–1968.

[17] N. Pradhan, D. Reifsnyder, R. Xie, J. Aldana, X. Peng, *Journal of the American Chemical Society* 129 (2007) 9500–9509.

[18] S. Govindraju, M.P. Kalenga, M. Airo, M.J. Moloto, L.M. Sikhwivhilu, N. Moloto, *Optical Materials* 38 (2014) 310–313.

[19] J. Butkus, P. Vashishtha, K. Chen, J.K. Gallaher, S.K.K. Prasad, D.Z. Metin, G. Laufersky, N. Gaston, J.E. Halpert, J.M. Hodgkiss, *Chemistry of Materials* 29 (2017) 3644–3652.

[20] S.T. Gentry, S.F. Kendra, M.W. Bezpalko, *The Journal of Physical Chemistry C* 115 (2011) 12736–12741.

[21] O.P. Lamba, S.K. Sinha, *Solid State Communications* 57 (1986) 365–371.

[22] R.K. Sithole, L.F.E. Machogo, M.A. Airo, S.S. Gqoba, M.J. Moloto, P. Shumbula, J.V. Wyk, N. Moloto, *New Journal of Chemistry* 42 (2018) 3042–3049.

[23] R. Seals, R. Alexander, L.T. Taylor, J.G. Dillard, *Inorganic Chemistry* 12 (1973) 2485–2487.

[24] J. Sharma, Z. Iqbal, *Chemical Physics Letters* 56 (1978) 373–376.

[25] H. Sun, Z. Li, L. Kong, B. Wang, C. Zhang, Q. Yuan, S. Huang, Y. Liu, L. Li, *Chemical Communications* 54 (2018) 9345–9348.

[26] M. Kulbak, S. Gupta, N. Kedem, I. Levine, T. Bendikov, G. Hodes, D. Cahen, *The Journal of Physical Chemistry Letters* 7 (2016) 167–172.

CHAPTER 6

Fabrication of Schottky Diode using $CsSnBr_3$, $Cs_3Bi_2Br_9$ and Cs_2ZnBr_4 nanocrystals

6.1 Introduction

The fabrication of most electronic and optoelectronic devices requires the assemblage of two or more different materials (metals, semiconductors and insulators) [1]. The interface formed between these dissimilar materials is called a junction and it is pivotal since it influences the electrical and transport properties of the device. Two possible junctions can be formed when a metal and a semiconductor are in contact, these 2 junctions are dependent on the work function of the semiconductor and its relation to the metal [2]. When the metal's work function is higher than the semiconductor's work function, a Schottky junction is formed. Contrarily, when the

metal's work function is lower than that of the semiconductor's work function an ohmic junction is formed [2]. The Schottky junction or Schottky barrier contact shows a rectifying current-voltage (I-V) characteristic upon changing the polarity of the applied voltage while the ohmic conductor exhibits a non-rectifying characteristic when the polarity of the applied voltage is changed as shown in Fig. 6.1.

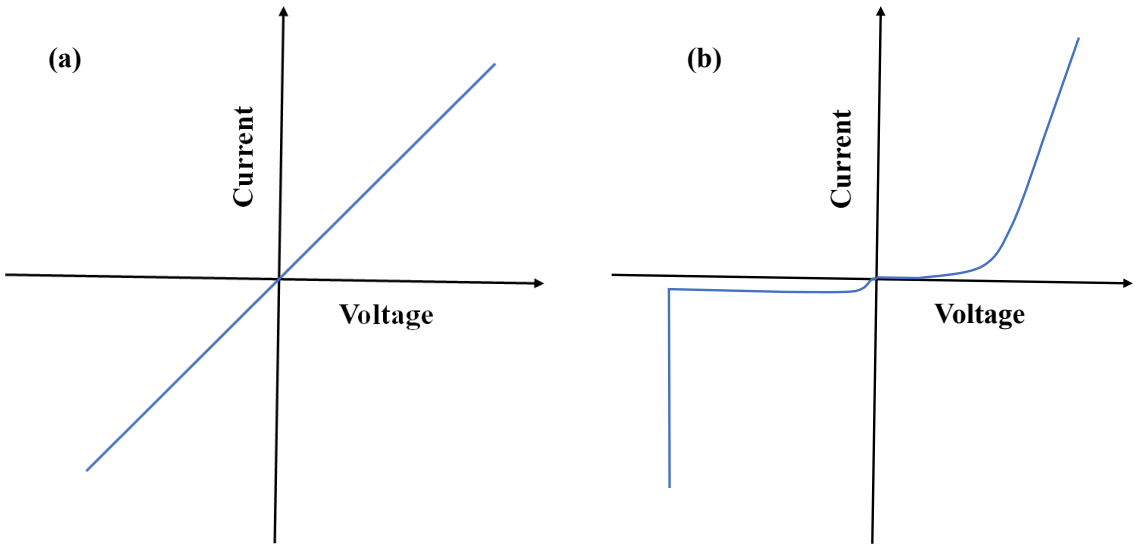

Fig. 6.1: Current-voltage characteristic of (a) ohmic and (b) Schottky contact.

The Schottky diode is useful for numerous applications such as in solar cells, photodiodes and bypass diodes [3–6]. The Schottky diode has also been used in gas sensing applications where the formation of a stable contact with the active layer is necessary. Hence, due to the versatile nature of Schottky diodes, it is important to fabricate Schottky diodes based on new materials such as perovskites and the determination of their electrical parameters offers great possibilities for their potential application in solar cells.

6.2 Experimental procedures

6.2.1 Chemicals

Gold target (Au, 99.95, 6.35 mm) was purchased from Alfa Aesar. Acetone, ethanol, toluene 95%, indium doped tin oxide (ITO) coated glass slide (surface resistivity ~ 8-12 Ω/sq) were purchased from Sigma-Aldrich. All chemicals were used without any further purification.

6.2.2 Device fabrication and characterization

Prior to the device fabrication, the ITO coated glass substrate was washed using the ultrasonic bath in ethanol, acetone and distilled water for 15 min each. The ITO glass substrates were then dried. The device structure (Fig. 6.2) consisted of ITO/perovskite/Au thin film layers. The device was obtained by spin-coating the well - dispersed solution of the perovskite nanocrystals on the ITO substate at 3000 rpm for 2 min. After vacuum drying of the film at 90 °C, the top Au contact was thermally deposited through a shadow mask to generate an array of patterned electrodes. The Au was deposited in high vacuum of pressure above 4×10^{-5} Pa, voltage of 80 kV, current of 280 A for 5 min with the device having an active area of 0.05 cm^2. The $I-V$ measurement for the Schottky device was performed in the dark at 298 K using a Keithley 2400 source meter.

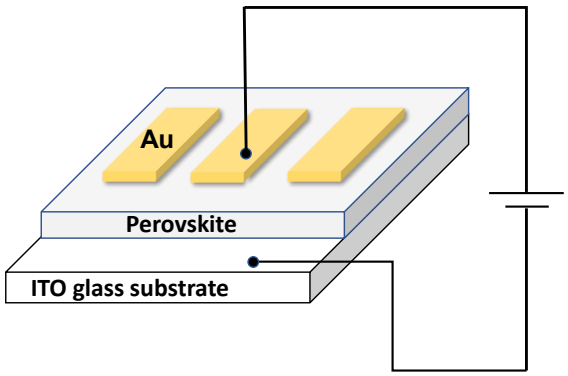

Fig. 6.2: Schematic showing the device architecture of the Schottky diode.

6.3 Results and discussion

Herein, the perovskite and hybrid perovskite nanocrystals ($CsSnBr_3$, $Cs_3Bi_2Br_9$ and Cs_2ZnBr_4) were used as the semiconductor in a Schottky diode. Shown in Fig. 6.2 is the device architecture with an active device area of 0.05 cm^2. The Schottky barrier height was measured from the $I-V$ curve. According to the Schottky thermionic theory the dependence of the forward current I on the applied voltage V is given by the relation:

$$I = I_0\left[exp\left(\frac{qV}{nkT}\right)-1\right] \qquad (6.1)$$

where q is the electronic charge, k the Boltzmann constant, T the ambient temperature, and n is a dimensionless factor indicating the deviation from the ideal Schottky cell characteristics. I_0 is the saturation current represented by equation (6.2):

$$I_0 = SA^*T^2exp\left(-\frac{q\emptyset_B}{kT}\right) \qquad (6.2)$$

$$LnI = LnI_0 + \frac{q}{nkT}V \qquad (6.3)$$

with $A^* = A\left(m^*/m_0\right)$, where A is the Richardson constant (A = 120 /cm^2 K^2), m^* is the effective electron mass and it is estimated to be 0.73, 0.34 and 0.12 m_0 for $CsSnBr_3$, $Cs_3Bi_2Br_9$ and Cs_2ZnBr_4 nanocrystals respectively [7,8]. The saturation currents were 9.97 mA, 9.92 mA and 9.98 mA for the Sn, Bi and Zn based Schottky diodes. The barrier height ($\emptyset_B$) can be obtained from equation (6.4) where S is the area of the cell.

$$\emptyset_B = \left(-\frac{kT}{q}\right) Ln\left(-\frac{SA^*T^2}{I_0}\right) \qquad (6.4)$$

The coefficient n is evaluated from the slope of $Ln\ I$ versus V (equation (6.3)).

The classical thermionic method has a limitation because it only works for diodes possessing negligible series resistance in the forward bias. However, since the series resistance is a crucial parameter influencing the electrical behavior of a Schottky diode, other methods (Cheung and Norde) are employed to determine the series resistance (R_s), $\emptyset_B$ and n. Using Cheung's method, n, $\emptyset_B$ and R_s can be evaluated. The forward bias current – voltage characteristics due to thermionic emission of a Schottky barrier diode with series resistance can be expressed as Cheung's functions [9]:

$$\frac{dV}{dLnI} = n\frac{kT}{q} + IR_s \qquad (6.5)$$

$$H(I) = V - n\frac{kT}{q}Ln\left(\frac{1}{SA^{*2}}\right) \qquad (6.6)$$

$$H(I) = n\emptyset_B + IR_s \qquad (6.7)$$

From a straight-line plot of $dV/dLnI$ vs I, n, and R_s can be calculated from the slope and the y-intercept using equation (6.5).

Furthermore, Norde proposed an alternative method to determine values of series resistance and barrier height [10]. The Norde method can be expressed as follows:

$$F(V) = \frac{V}{\gamma} - \frac{kT}{q}Ln\left(\frac{I}{SA^*T^2}\right) \qquad (6.8)$$

where γ is a first integer greater than n, I the current obtained from $I-V$. In this study γ is taken to be 2, 3 and 5 for $CsSnBr_3$, $Cs_3Bi_2Br_9$ and Cs_2ZnBr_4 respectively. The barrier height and series resistance can be obtained from equation (6.9) and (6.10).

$$\emptyset_B = F(V_0) + \frac{V_0}{\gamma} - \frac{kT}{q} \qquad (6.9)$$

$$R_s = \frac{kT(\gamma - n)}{qI} \qquad (6.10)$$

The I-V characteristic curves of $CsSnBr_3$, $Cs_3Bi_2Br_9$ and Cs_2ZnBr_4 nanocrystals are shown in Fig. 6.3, 6.4 and 6.5 respectively. These representative I-V curves all show a degree of rectification which is characteristic of a Schottky barrier diode.

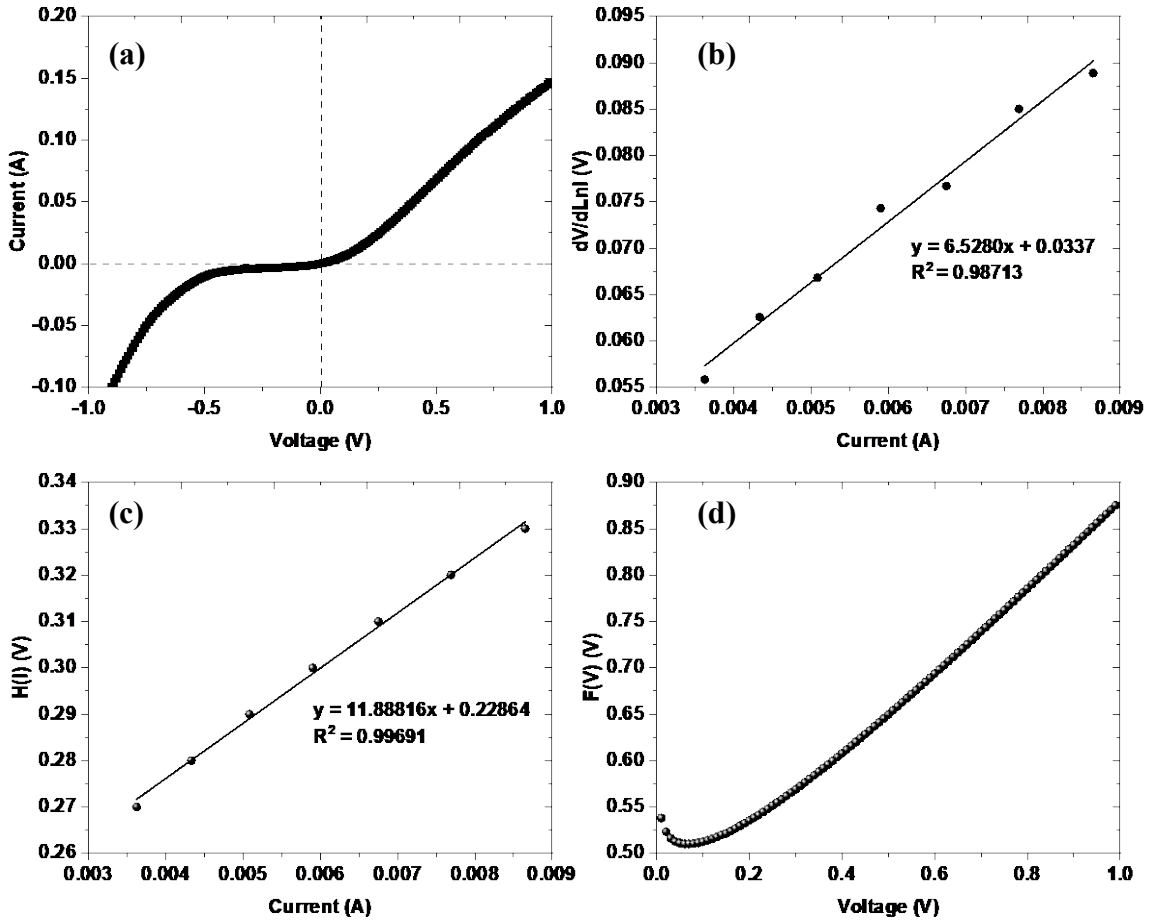

Fig. 6.3: (a) *I–V*, (b) *dV/dLnI −I,* (c) *H(I) −I and* (d) *F(V)-V* characteristics of the Au/$CsSnBr_3$ Schottky diode at the temperature of 298 K in the dark.

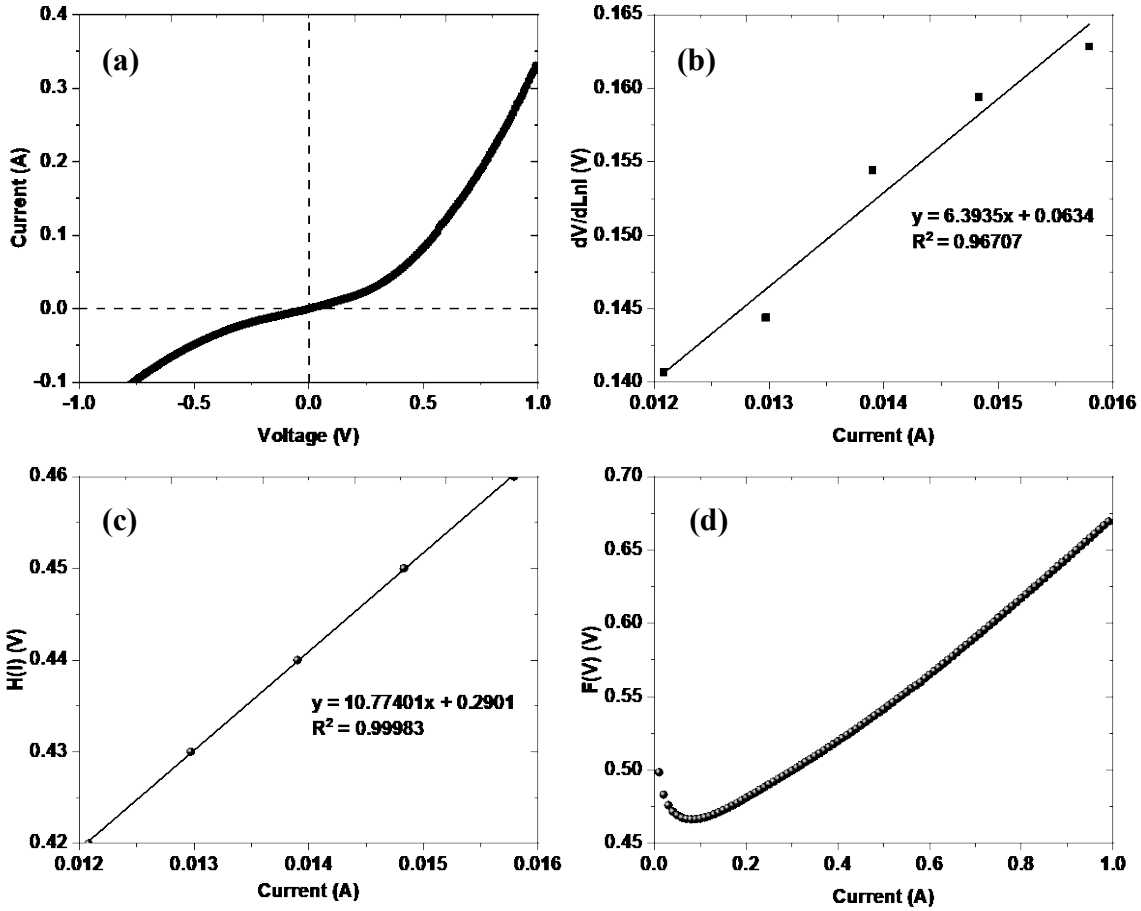

Fig. 6.4: (a) ***I–V,*** **(b)** ***dV/dLnI −I,*** **(c)** ***H(I) −I and*** **(d)** ***F(V)-V*** **characteristics of the Au/$Cs_3Bi_2Br_9$ Schottky diode at the temperature of 298 K in the dark.**

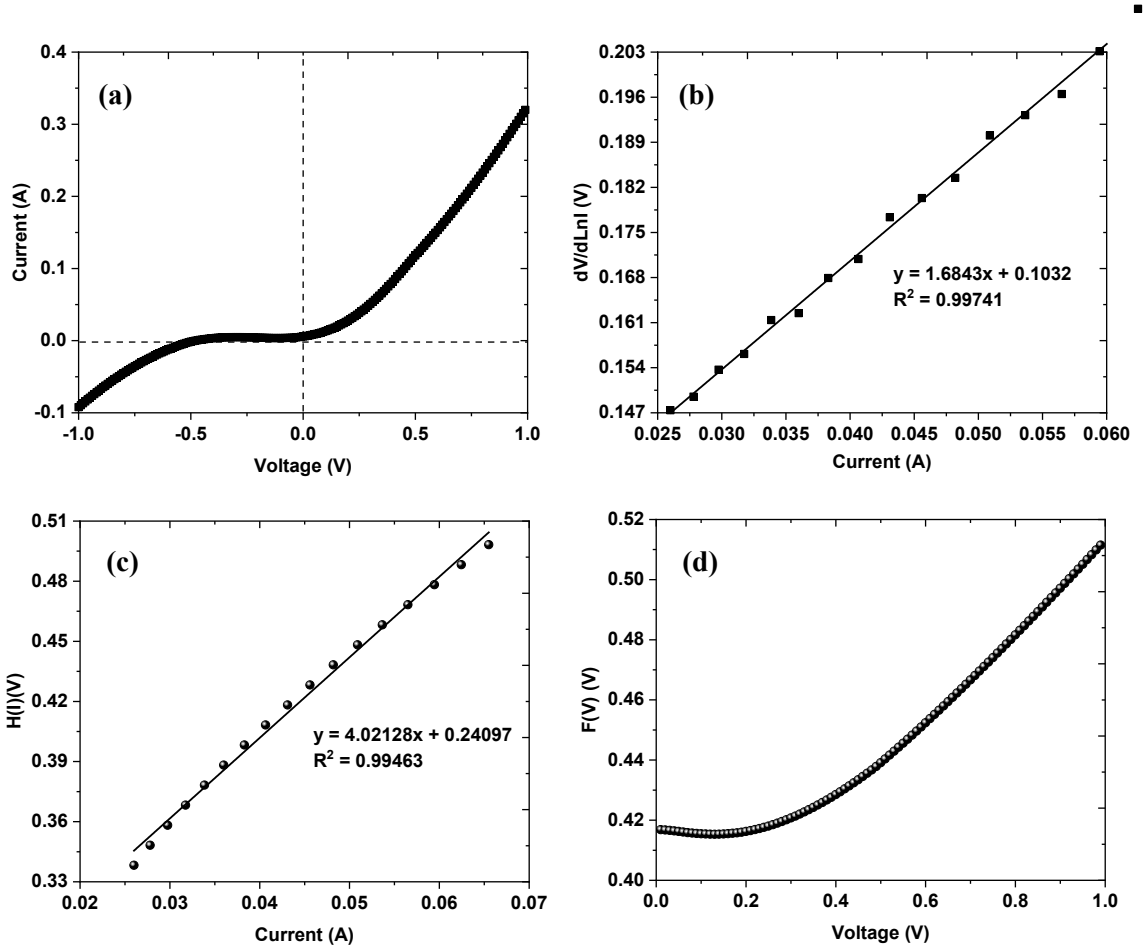

Fig. 6.5: (a) ***I–V,*** **(b)** ***dV/dLnI −I,*** **(c)** ***H(I) −I and*** **(d)** ***F(V)-V*** **characteristics of the Au/Cs_2ZnBr_4 Schottky diode at the temperature of 298 K in the dark.**

Table 6.1: Diode parameters obtained from the $I-V$ data of $CsSnBr_3$, $Cs_3Bi_2Br_9$ and Cs_2ZnBr_4

Material	Method	Ideality factor, n	Barrier height, $\emptyset_B$	Series resistance, R_s
$CsSnBr_3$	$LnI-V$	3.370	0.330 eV	-
	$dV/dLnI-I$	1.300	-	6.528 Ω
	$H(I)-I$	-	0.174 eV	11.888 Ω
	$F(V)-V$	-	0.785 eV	6.040 Ω
$Cs_3Bi_2Br_9$	$LnI-V$	3.670	0.313 eV	-
	$dV/dLnI-I$	2.500	-	6.393 Ω
	$H(I)-I$	-	0.117 eV	10.774 Ω
	$F(V)-V$	-	0.462 eV	2.047 Ω
Cs_2ZnBr_4	$LnI-V$	9.629	0.287 eV	-
	$dV/dLnI-I$	4.018	-	1.684 Ω
	$H(I)-I$	-	0.059 eV	4.021 Ω
	$F(V)-V$	-	0.191 eV	1.7696 Ω

The electrical characteristics for classical thermionic, Cheung and Norde's models are summarized in Table 6.1. The classical thermionic ideality factors n of the three Schottky diodes are 3.370, 3.670 and 9.629 for $CsSnBr_3$, $Cs_3Bi_2Br_9$, and Cs_2ZnBr_4 samples respectively. The Schottky diode's ideality factor provides information about how closely the Schottky diode follows the ideal diode equation where in an ideal diode, n is unity. The obtained values of the ideality factor of the perovskite NCs show a deviation from the ideal thermionic emission model and this may be due to extrinsic factors such as the presence of interface states or barrier height inhomogeneity [11]. The ideality factor of the Cs_2ZnBr_4 NCs is particularly high as compared to that of $CsSnBr_3$ and $Cs_3Bi_2Br_9$ and this is attributed in part to defects induced by

cleaving of the semiconductor in the junction region. This deviation of n is an indication that other mechanism such as field-enhanced and thermally assisted tunneling contribute to the current transport in the system [12]. Literature reports an ideality factor of 7.09 in the Pb-based perovskite Schottky diode [13], which is higher than the n obtained for the Sn and Bi perovskite but lower than that of Zn hybrid perovskite.

The n, were also determined with the Cheung's method using equations (6.6) to (6.7). From Cheung's function, n, was found to be 1.3, 2.5 and 4.018 for $CsSnBr_3$, $Cs_3Bi_2Br_9$, and Cs_2ZnBr_4 respectively. This indicates that a moderately good junction was formed for the $CsSnBr_3$ and $Cs_3Bi_2Br_9$ as compared to the Cs_2ZnBr_4 junction. Shaikh *et al*., [14] employed $CH_3NH_3PbBr_3$ perovskite for a Schottky diode, using the Cheung's method, an ideality factor of 1.7 was observed, this n is comparable to the one obtained for the Sn-based perovskite. This suggests that the synthesized $CsSnBr_3$ perovskite NCs may be used as replacement for Pb-based perovskite materials. Due to presence of defects and generation-recombination currents within the space charge region, high bandgap heterojunctions often possess high ideality factor [15, 16]. As a result, from both the classical thermionic and Cheung's method a concomitant increase in n was observed as the bandgap energy increases from $CsSnBr_3$ to Cs_2ZnBr_4.

The Schottky barrier height $\emptyset_B$ is a reflection of energy position between semiconductor's band edge and metal's Fermi level where the level of energy mismatch is indicated by magnitude of barrier height [17]. Since the flow of current across the metal-semiconductor junction is contingent on the magnitude of $\emptyset_B$, the electrical properties can be confirmed after $\emptyset_B$ determination. The $\emptyset_B$ was found to steadily decrease from 0.330 eV to 0.313 eV and finally to 0.287 eV for the $CsSnBr_3$, $Cs_3Bi_2Br_9$, and Cs_2ZnBr_4 based Schottky diodes respectively using the thermionic model. Similar decrement was observed in both the Cheung and Norde's model where $\emptyset_B$ of 0.174 eV, 0.117 eV and 0.059 eV were obtained for the Sn, Bi and Zn perovskites using the Cheung's method. While $\emptyset_B$ of 0.785 eV, 0.462 eV and 0.191 eV were obtained for $CsSnBr_3$, $Cs_3Bi_2Br_9$ and Cs_2ZnBr_4 Schottky diodes using the Norde's model.

This steady decrease in $\emptyset_B$ from $CsSnBr_3$ to Cs_2ZnBr_4 nanocrystals can be attributed to surface oxidation. The $\emptyset_B$ is usually influenced by surface oxidation where $\emptyset_B$ increases linearly with oxide thickness [18,19]. Hence, it is unsurprising that the easily oxidized perovskite ($CsSnBr_3$) possessed the highest $\emptyset_B$. This effect of oxide thickness on $\emptyset_B$ is due to the charges trapped in

the oxide layer which alters the semiconductor's charge distribution by forming a dipole layer with the charges confined in the surface states [20]. This results in a potential shift that alters the $\emptyset_B$. Although Schottky diodes based on perovskite semiconductors have barely been reported, however, a barrier height of 0.97 eV was reported for an organo-lead halide perovskite Schottky photodiode [21]. Liu *et al*., [22] fabricated an high-efficiency graphene-on-silicon Schottky junction solar cell, the undoped device showed an ideality factor of 3.39 while the doped material which has the highest efficiency had an ideality factor of 1.50. Both the pristine and doped material had $\emptyset_B$ of 0.76 and 0.87 eV. These values are comparable to the ones obtained for the perovskites herein which further accentuate the potential of Sn, Bi and Zn as Pb substitute in perovskites.

The R_s obtained from the Cheung's method were 6.528 Ω and 11. 888 Ω for $CsSnBr_3$ NCs, 6.393 Ω and 10.774 Ω for $Cs_3Bi_2Br_9$ NCs and 1.684 Ω and 4.021 Ω for Cs_2ZnBr_4 NCs. However, the Norde's method gave R_s of 6.040 Ω, 2.047 Ω and 1.769 Ω for Sn, Bi and Zn based Schottky diodes respectively. Series resistance is one of the parasitic resistances that influence the I-V characteristics of a Schottky diode and determination of this parameter provides information about the performance of the Schottky device. Although there are no standard limits for R_s, however, low R_s are required for efficient solar cell performance [23]. Also, when the series resistance is high, obtaining the diode parameters especially the determination of the barrier height becomes challenging [24]. The R_s obtained from both Cheung's and Norde's method steadily increased from Cs_2ZnBr_4 to $CsSnBr_3$. Of the three materials, $CsSnBr_3$ showed the highest series resistance while Cs_2ZnBr_4 had the least R_s. The trend can be due to the oxidation of the perovskite NCs either prior to film deposition or during the metal deposition. This oxidation may lead to the formation of oxide layer at the metal-semiconductor interface which consequently form an interface state charge which can affect the electrical properties of the diode [25]. This idea was further substantiated by the XPS data for the individual perovskites. From the XPS spectra of $CsSnBr_3$, $Cs_3Bi_2Br_9$ and Cs_2ZnBr_4, the obtained atomic % of oxygen in the sample were 25.2, 8.4 and 3.9 respectively. Hence, this steady decrease in oxygen content from Sn to Zn perovskite as recorded *via* XPS analysis directly corresponds to the decrease in series resistance observed for the different materials. Another factor that may influence the diode's series resistance is the nanocrystal morphology where highly oriented nanostructures have been demonstrated to possess impressive performance [26]. Nanorods, especially the vertically aligned nanorods have been reported to

show improved electrical characteristics [26,27]. It is therefore not surprising that Cs_2ZnBr_4 with nanorod morphology showed the least series resistance when compared to other nanocrystals. This impressive Cs_2ZnBr_4 nanorods' R_S is because there is a probability that some of the nanorods will be vertically aligned, hence they possess higher vertical conduction since they use one-dimensional transport in the direction that is perpendicular to the conducting substrate. This benefit of higher vertical conduction would be difficult to obtain in morphologies different from nanorods ($CsSnBr_3$) or partially agglomerated nanocrystals ($Cs_3Bi_2Br_9$) [26]. Finally, the values obtained from Norde's functions are different from Cheung's methods probably because Cheung's functions are only executed for the nonlinear region of forward bias $I-V$ curve while Norde's functions are executed for the whole forward bias region of the $I-V$ curve of the diode.

6.4 Conclusion

Spin-coating method was used to make different perovskite NCs film and the contact was deposited *via* thermal evaporation. The fabricated devices show rectifying behavior which is characteristic of a Schottky diode. The Schottky barrier parameters were extracted for the I-V characteristic of each device using the classical thermionic emission model, Cheung's model and the Norde's model. The Schottky diode parameters especially the barrier heights and the series resistance are, to a large extent, influenced by surface oxidation and nanocrystal morphology. The Cs_2ZnBr_4 based Schottky diode showed the best electrical properties by having the lowest series resistance and good barrier height as extrapolated by the Cheung and Norde's model. The electrical properties indicate that all the three materials have potential applications in photovoltaics, photodiodes and sensors.

6.5 References

[1] M.R. Islam, D. Joung, S.I. Khondaker, *New Journal of Physics* 13 (2011) 035021.

[2] B. Sharma, Metal-Semiconductor Schottky Barrier Junctions and Their Applications, *Springer Science & Business Media*, (2013).

[3] T. Le Duc, E. Moyen, M.R. Zamfir, J. Joe, X. Yan, Y. Zhang, D. Pribat, *ACS Applied Materials and Interfaces* 12 (2020) 37464–37469.

[4] Z. Huang, C. Yu, A. Chang, Y. Zhao, W. Huang, S. Chen, C. Li, *Journal of Materials Science* 55 (2020) 8630–8641.

[5] S.V. Mukhamale, A.R. Chavan, R.M. Lokhande, P.P. Khirade, *Solar Energy* 211 (2020) 866–878.

[6] M. Mathew, C.S. Rout, *Journal of Materials Chemistry C* 9 (2021) 395–416.

[7] C. Yu, Z. Chen, J. J. Wang, W. Pfenninger, N. Vockic, J.T. Kenney, K. Shum, *Journal of Applied Physics* 110 (2011) 063526.

[8] K.M. McCall, Z. Liu, G. Trimarchi, C.C. Stoumpos, W. Lin, Y. He, I. Hadar, M.G. Kanatzidis, B.W. Wessels, *ACS Photonics* 5 (2018) 3748–3762.

[9] S. Cheung, N. Cheung, *Applied Physics Letters* 49 (1986) 85–87.

[10] H. Norde, *Journal of Applied Physics* 50 (1979) 5052–5053.

[11] S. Khan, S. Halder, A. Dey, B. Dutta, P.P. Ray, S. Chattopadhyay, *New Journal of Chemistry* 44 (2020) 11622–11630.

[12] R. Nouchi, *Journal of Applied Physics* 116 (2014) 184505.

[13] L. Chen, J. Deng, H. Gao, Q. Yang, G. Wang, L. Kong, M. Cui, Z. Zhang, *Journal of Materials Science: Materials in Electronics* 27 (2016) 4275–4280.

[14] P.A. Shaikh, D. Shi, J.R.D. Retamal, A.D. Sheikh, M.A. Haque, C.-F. Kang, J.-H. He, O.M. Bakr, T. Wu, *Journal of Materials Chemistry C* 4 (2016) 8304–8312.

[15] M. Brötzmann, U. Vetter, H. Hofsäss, *Journal of Applied Physics* 106 (2009) 063704.

[16] A. Jana, S. Ghosh, P.S. Devi, N.R. Bandyopadhyay, M. Ray, *Journal of Materials Chemistry C* 2 (2014) 9613–9619.

[17] A.E.-D.S. Hafez, M. Abd El-Latif, ISRN *Electronics* (2013) e528094.

[18] F. Hasegawa, M. Onomura, C. Mogi, Y. Nannichi, *Solid-State Electronics* 31 (1988) 223–228.

[19] C. Wei, S. Yee, *Journal of Applied Physics* 45 (1974) 971–971.

[20] M. Peckerar, *Journal of Applied Physics* 45 (1974) 4652–4652.

[21] W. Luo, L. Yan, R. Liu, T. Zou, S. Zhang, C. Liu, Q. Dai, J. Chen, H. Zhou, *Semiconductor Science and Technology*. 34 (2019) 074004.

[22] X. Liu, X.W. Zhang, J.H. Meng, Z.G. Yin, L.Q. Zhang, H.L. Wang, J.L. Wu, *Applied. Physics Letters*. 106 (2015) 233901.

[23] F. Fabregat-Santiago, G. Garcia-Belmonte, I. Mora-Seró, J. Bisquert, *Physical Chemistry Chemical Physics*. 13 (2011) 9083–9118.

[24] E. Karagöz, S.F. Varol, S. Sayın, Z. Merdan, *Physical Chemistry Chemical Physics*. 20 (2018) 30502–30513.

[25] İ. Dökme, *Physica B: Condensed Matter* 388 (2007) 10–15.

[26] M. Kumar, V.K. Lamba, *AIP Conference Proceedings* 2142 (2019) 140032.

[27] B.S. Mwankemwa, S. Akinkuade, K. Maabong, J.M. Nel, M. Diale, *Physica B: Condensed Matter* 535 (2018) 175–180.

CHAPTER 7

Overall conclusions and recommendations

7.1 Conclusions

In this dissertation, colloidal method of synthesis was used to synthesize $CsSnBr_3$, $Cs_3Bi_2Br_9$ and Cs_2ZnBr_4 nanocrystals. Effect of different reaction parameters such as temperature and time on the properties of perovskite nanocrystals was explored. Cubic $CsSnBr_3$ nanocrystals were successfully synthesized at optimum conditions of 230 °C for 1 min in OLA and OA using $SnBr_2$ and Cs_2CO_3 precursors. $CsSnBr_3$ NCs produced quantum dots morphology. Hexagonal $Cs_3Bi_2Br_9$ NCs were synthesized at optimum conditions of 210 °C while orthorhombic Cs_2ZnBr_4 hybrid perovskite was formed at 160 °C, both using 1 min synthesis time. Pseudo spherical and nanorod morphologies were obtained for the $Cs_3Bi_2Br_9$ and Cs_2ZnBr_4 NCs, respectively. All the perovskites NCs were influenced by the reaction time and temperature as a result, the bandgap and morphologies of the NCs varied with these parameters. XRD and XPS showed the composition of the individual perovskite while NMR and FTIR conclusively showed that OLA successfully capped the NCs surface. The $CsSnBr_3$ was stable for 3 days while the Cs_2ZnBr_4 and $Cs_3Bi_2Br_9$ were stable for over 21 days.

The different perovskites were then used to fabricate Schottky diodes to investigate their potential for electronic and optoelectronic applications. The perovskite thin films were formed *via* spin coating and the metal contact was deposited *via* thermal evaporation. All the three devices showed rectification behavior which is indicative of a Schottky contact. The materials showed impressive electrical properties which were comparable and sometimes better than those obtained in literature. Such results indicate that $CsSnBr_3$, Cs_2ZnBr_4 and $Cs_3Bi_2Br_9$ are potential semiconductors for photovoltaic and sensor applications. Also, the synthetic method adopted can lower the overall cost of preparation of perovskite materials and fabricating devices due to the use of lower temperatures, low reaction times and fewer capping agents while serving as a potential alternative to the toxic Pb.

7.2 Recommendations

- To further characterize the nanocrystals, use of HRTEM to determine the lattice fringes in the perovskites.
- Use hyphenated-technique (TGA-FTIR and TGA-MS) to determine the actual products of thermal degradation.
- To further obtain better diode parameters, the thin-films quality can be improved upon.
- Investigate other methods to fabricate thin films that can be reproducible.
- To see the effect of photon energy on the Schottky diodes.
- Fabricate and optimize a full perovskite solar cell with the three materials.